THE OHIO STATE UNIVERSITY

Planar Near-Field Scanning for Compact Range Bistatic Radar Cross-Section Measurement

S.R. Tuhela-Reuning and E.K. Walton

The Ohio State University

ElectroScience Laboratory

Department of Electrical Engineering
Columbus, Ohio 43212

Final Report 723105-2
Contract No. ~~NA3-1125~~ NAG3-1125
November 1991

NASA/Lewis Research Center
21000 Brookpark Road
Mail Stop 54-8
Cleveland, Ohio 44135

A. Approved for public release; Distribution is unlimited

NOTICES

When Government drawings, specifications, or other data are used for any purpose other than in connection with a definitely related Government procurement operation, the United States Government thereby incurs no responsibility nor any obligation whatsoever, and the fact that the Government may have formulated, furnished, or in any way supplied the said drawings, specifications, or other data, is not to be regarded by implication or otherwise as in any manner licensing the holder or any other person or corporation, or conveying any rights or permission to manufacture, use, or sell any patented invention that may in any way be related thereto.

50272-101

REPORT DOCUMENTATION PAGE	1. REPORT NO.	2.	3. Recipient's Accession No.

4. Title and Subtitle
Planar Near-Field Scanning
for Compact Range Bistatic Radar Cross-Section Measurement

5. Report Date
November 1991

6.

7. Author(s)
S.R. Tuhela-Reuning and E.K. Walton

8. Performing Org. Rept. No.
723105-2

9. Performing Organization Name and Address
The Ohio State University
ElectroScience Laboratory
1320 Kinnear Road
Columbus, OH 43212

10. Project/Task/Work Unit No.

11. Contract(C) or Grant(G) No.
(C)
(G) ~~NA3-1125~~ NAG3-1125

12. Sponsoring Organization Name and Address
NASA/Lewis Research Center
21000 Brookpark Road, Mail Stop 54-8
Cleveland, Ohio 44135

13. Report Type/Period Covered
Final Report

14.

15. Supplementary Notes

16. Abstract (Limit: 200 words)

This thesis details the design, construction and testing of a low cost, planar scanning system to be used in a compact range environment for Bistatic Radar Cross Section (Bistatic RCS) measurement. This scanning system is similar to structures used for measuring near field antenna patterns. A synthetic aperture technique is used for plane wave reception. System testing entailed comparison of measured and theoretical bistatic RCS of a sphere and a right circular cylinder. Bistatic scattering analysis of the ogival target support, target and pedestal interactions, and compact range room was necessary to determine measurement validity.

17. Document Analysis a. Descriptors
NEAR-FIELD
PLANAR SCANNING
BISTATIC RCS
BACKPROJECTION
SAR

b. Identifiers/Open-Ended Terms

c. COSATI Field/Group

18. Availability Statement	19. Security Class (This Report)	21. No. of Pages
A. Approved for public release; Distribution is unlimited.	Unclassified	130
	20. Security Class (This Page) Unclassified	22. Price

(See ANSI-Z39.18) *See Instructions on Reverse* OPTIONAL FORM 272 (4-77)
Department of Commerce

Contents

List of Figures

List of Tables

Chapter 1

Introduction

The goal of this project was to design, construct, and evaluate the performance of a low cost alternative method of obtaining Bistatic Radar Cross-Section (Bistatic RCS) measurement data in a compact range environment. Bistatic RCS of a target is defined as 4π times the bistatically scattered power from the target per steradian divided by the far field incident signal power per unit area. The bistatic scattering measurement scenario considered in this work is shown in Figure 1.1. Note the bistatic angle definition. As shown in this figure, a compact range consisting of a parabolic reflector and a spherical wave feed was used to generate a plane wave that illuminated the target [1]. The test target bistatically scattered the incident plane wave and the bistatic RCS measurement system then determined the far field scattered signal in the desired bistatic direction.

A simple and effective bistatic RCS measurement system concept is to place a second parabolic reflector at the desired bistatic angle to receive the scattered fields. This intrinsically creates a far field measurement due to the collimating effect of the parabolic surface. Lower cost alternatives are desired because this method is expensive and requires a large measurement chamber.

Many methods exist to estimate a far field radiated signal without the distance necessary to measure the actual far field signal. The parabolic reflector is one possibility. Other methods include using a vertical one-dimensional parabolic cylinder

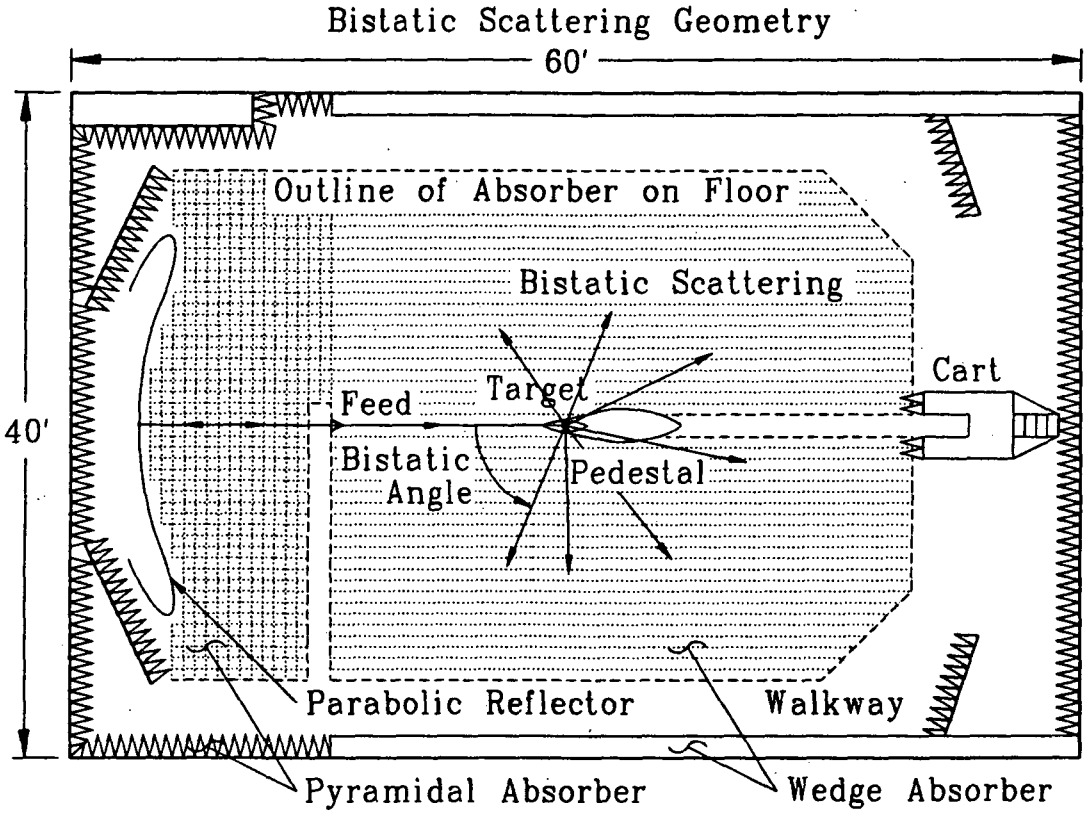

Figure 1.1: Bistatic scattering arrangement of the OSU-ESL compact range.

scanned in a radial manner around the target. This measurement method utilizes a one dimensional near field to far field transformation algorithm in cylindrical coordinates to obtain the far field data. Another alternative is to scan the scattered fields along a spherical, cylindrical, or planar surface with a probe antenna and transform the measured data to the far field. Each of these surface scans require a two dimensional near field to far field transformation algorithm but planar scanning does not require curved sampling paths and it uses a well known near field to far field transformation algorithm, the heart of which is a two dimensional Fourier transform [2]. In this research, a combination of planar scanning and data processing techniques is used to estimate the bistatically scattered far field RCS response of test targets.

This technique is similar to the classical planar near field scanning technique for antenna pattern measurement. Upon illumination of the target by the plane wave, the target becomes a radiator, behaving like an antenna. This means that much of the planar near field scanning technology developed for antenna pattern measurements applies to this research. Many requirements of a planar scanning system as reported by E.B. Joy, J.B. Rowland [3], [4] and D.G. Falconer [5] are appropriate for antenna gain pattern measurements. However, for Bistatic RCS measurement, many of the constraints can be modified as discussed in Chapter 2.

In this research, the bistatically scattered fields were probed over a planar aperture using a computer controlled x-y scanner which was designed and built as part of this project. Data processing techniques were used to locate the scattering centers of the test targets and to estimate the far field bistatic scattering from the test targets. The far field estimation utilized a synthetic aperture technique in which the x-y probe measurement data sets were synthetically combined to produce the response of an array antenna and then spatially windowed to induce selective plane wave reception. A window function was applied to the aperture measurement data which mimicked the amplitude and phase aperture distribution of a compact range reflector with rolled edges. Applying this window to an array antenna in the trans-

mitting mode would cause a transmit pattern similar to a compact range reflector. By reciprocity, the synthesized antenna array should receive a single plane wave and thus estimate the far field bistatic scattered signal of the test target.

The data acquisition system used in this work included a pulsed CW radar measurement system installed in The Ohio State University ElectroScience Laboratory (OSU-ESL) compact range, an Everex 386/20 computer for radar and scanner control, and a VAX-8550 for data storage and computations. Measurement of background and reference targets allowed for background subtraction and calibration of the test targets. Background subtraction was necessary to reduce direct reflected signals from the rolled edges of the compact range parabolic reflector. Calibration removed intrinsic system non-linearities, such as the transition between the 2 to 6 GHz synthesizer and the 6 to 18 GHz synthesizer. Measured and theoretical bistatic RCS responses were compared to evaluate the system performance. Test targets measured were a 6 inch diameter sphere, an 18 inch diameter sphere and a 6 cm tall right circular cylinder with a 4 cm diameter.

Chapter 2

Planar Near Field Scanning Theory

2.1 Introduction

The prototype scanner design reflects the wealth of published knowledge on planar near field scanning systems. However, for bistatic RCS measurement, some of the accuracy requirements, as stated in the literature, are inappropriate. In this chapter, the design parameters of scan plane size, probe measurement spacing, position accuracy, probe characteristics, and scanner to test target separation are discussed and mention is made where the criteria given in the references was modified for our specific application. The scan plane geometry and coordinate system is presented in Figure 2.1. The positive z' axis is directed toward the target zone.

2.2 Scan Plane Size

In classical near field antenna pattern measurements, many methods can be used to estimate the far-field scattered signal from a scan plane measured data set; Near field to far field transformations (such as Kern's Plane Wave Spectrum matrix approach [6]), direct determination of the source distribution at the target, or the Lorentz reciprocity formulation developed by Paris, Leach and Joy [7]. For the case of antenna gain estimation, Yaghjian [8] suggested performing the transformation

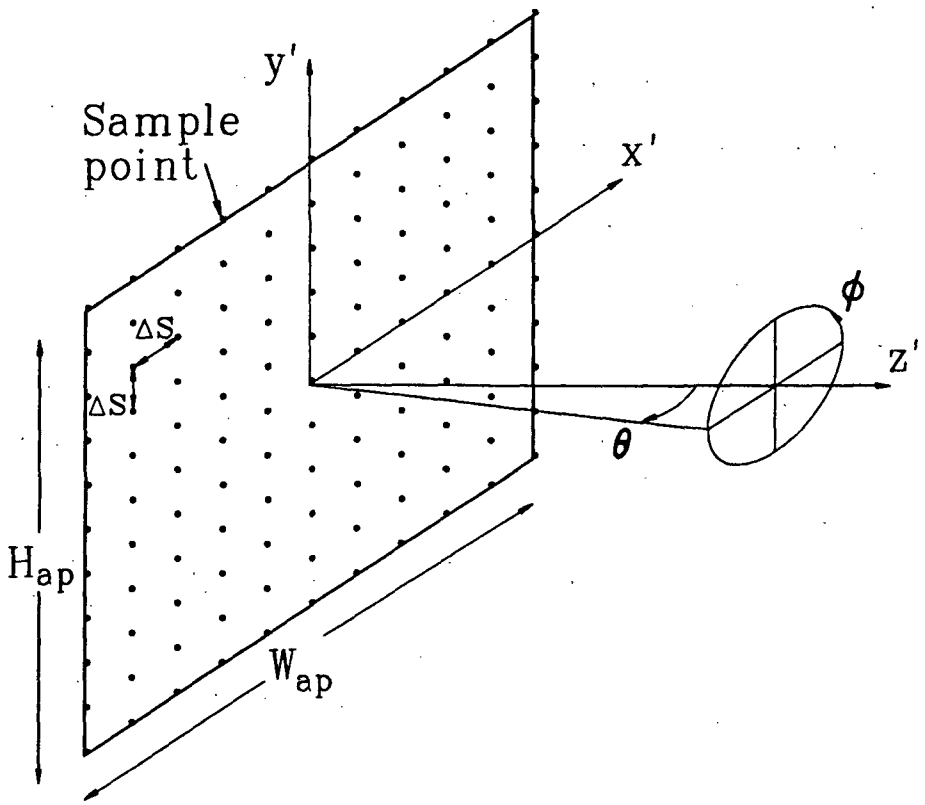

Figure 2.1: Coordinate reference frame for prototype x-y scanner aperture.

algorithm on the area outside of the scan plane aperture to quantify the magnitude of the error induced by a finite aperture. Since the fields outside the scan plane are not known, the antenna gain error is estimated as the "a priori" knowledge of the energy not intercepted by the scan plane. This limits the types of test radiators that can be measured by planar near field scanning to directive radiators since if the scan plane intercepts at least 80% of the radiated energy, the total radiated power can be well estimated and computation of antenna gain patterns is possible.

For the measurement of Bistatic RCS, only the scattered field in a small sector surrounding the desired bistatic angular direction is needed since the gain of the radiating structure is not desired. Therefore, no restriction is placed on the "directivity" of the target to be measured.

In this research, the maximum test target size is a function of the width of the scanner's receive-pattern plane-wave section, which depends on the performance of the aperture window function. The window function is constrained by the physical limits of the scan aperture size. The scan plane aperture size of the prototype scanner was constrained by the physical size of the prefabricated motion devices used. Therefore, the test target maximum dimension for the prototype scanner constructed was indirectly determined by the size of the scan plane aperture. In a full-scale scanner measurement system, the aperture size should be designed as a function of the desired test target dimensions.

The aperture efficiency of the prototype scanner (the ratio of the largest aperture dimension to the largest dimension of the plane wave zone) was desired to be as large as possible, and, when implemented, was comparable with the aperture efficiency of a compact range reflector (including rolled edges). The performance of the window function and the resulting aperture efficiency of the prototype scanner is discussed in Section 4.2.

2.3 Probe Sample Spacing

The planar scanner measures the scattered fields at discrete sample points across the scan aperture. To satisfy the Nyquist sampling criterion, samples should be taken at intervals which are equal to or less than one half the wavelength. However, Cown and Ryan [9] note that "thinned" near field data sets can be used to find accurate RCS values over reduced angular sectors. The grating lobes that occur due to the increased sample spacing are outside the reduced angular sector which encompasses the target and are simply ignored.

If the incident plane wave signals of interest are restricted to a small range of angles about the normal of the scan surface, the sample spacing should be such that neighboring array elements are 180° out of phase when the incident angle approaches the boundary of the reduced angular sector. This is the first null of the array pattern. With reference to Figure 2.1 for coordinate definitions, this sample spacing is given by:

$$\Delta S_{max} = \frac{\lambda}{2\cos(\frac{\pi}{2} + \theta_i)} \tag{2.1}$$

where θ_i is the reduced angular sector angle. The resulting grating lobes are located at incidence angles θ_{gl}:

$$\theta_{gl} = \frac{\pi}{2} \pm \arccos(\frac{n\lambda}{\Delta S}); \qquad n = 1, 2, 3, ... \tag{2.2}$$

For measurement of bistatic scattering in a compact range environment, the test target is not in the far field of the scanner. Grating lobes, which are a far field phenomenon, do not truly form in the near field. However, since the scanner can be viewed as a selective plane wave receiver and plane waves are a far field phenomenon, the sample spacing can be viewed to produce a spectrum of grating lobes similar to a plane wave spectrum which, if allowed to propagate to the far field, would become a true grating lobe. The same angular boundaries derived for the far field are therefore valid in the near field.

Freq. [GHz]	λ [cm]	θ_{gl} [deg.]
2	15.00	NONE
4	7.50	NONE
6	5.00	NONE
8	3.75	NONE
10	3.00	NONE
12	2.50	79.82
14	2.14	57.53
16	1.88	47.58
18	1.67	41.01

Table 2.1: Table of Grating Lobe Location: n=1, $\Delta S = 2.54$ cm

For OSU-ESL compact range dimensions, the target zone width is approximately 6 feet at a bistatic distance of roughly 18 feet in front of the scan plane aperture [10]. Therefore, the maximum incidence angle of interest is approximately 10 degrees from the scan plane normal and the maximum acceptable sample spacing is 2.8λ. This translates to 4.67 cm for the highest frequency of interest, 18 GHz.

A sample spacing of 2.54 cm was chosen for the testing of the prototype scanner system. The location of the resultant grating lobe spectrum as a function of frequency is tabulated in Table 2.1 using Equation (2.2) where grating lobes only exist for the n=1 case. For a 2.54 cm sample spacing, the border of the reduced angular sector (the first array pattern null) is approximately $\theta = 20$ degrees. This is twice the minimum reduced angular sector computed from the target zone width providing a larger potential target zone. This larger width, however, could not be utilized in this work due to small aperture effects.

2.4 Position Accuracy

Near field positions must be known to within a small fraction of a wavelength to obtain accurate near field measurements [2]. This statement is made in reference to the measurement of antenna gain patterns. Whether near field scanning is used for antenna gain measurements or bistatic RCS measurements, the position accuracy is a function of the accuracy needed in the computation of the desired response.

For the test geometry of the prototype scanner system, the scan plane to target separation was large enough (17 feet) to assume that position errors contributed only to errors in phase measurement. This would not be the case for a separation where the target was in the extreme near field of the scanner which is the normal geometry for antenna gain measurements. The prototype scanner design was prone to two types of position errors. The first positioning error was a non-planar nature of the scan surface affecting all sample locations, and the second error type was when only a single sample location was in error.

A non-planar nature of the scan aperture would induce redirection of the main beam component signals thus deforming the entire main beam the scanner. The scan aperture was aligned to be planar to $\pm$ 0.1 degrees. Thus, for a worst case misalignment of 0.2 degrees at a target to scanner separation of 17.5 feet, the redirection of the main beam of the scanner was only 0.7 inches at the target, a negligible error for targets 2 inches smaller than the maximum width of the scanner main beam. Due to the prototype scanner design, single sample position errors characteristically would be only 0.002 inch errors. Assuming that one sample location is in error, results in a maximum phase error of 1.1 degrees at 18 GHz (the smallest wavelength).

An important concern for bistatic measurements is re-positioning accuracy, necessary for background subtraction algorithms (if desired). The scanner must precisely reposition the antenna and RF cable to the same set of locations for each scan. Assuming all errors affect only phase measurements, background subtraction suppression of chamber-intrinsic signals by 20 dB requires that the target and background

voltage vectors (which are assumed to be of equal magnitudes for chamber-intrinsic signals), vector subtract to not more than 0.1 times the magnitude of the original signals. This will occur if the target and background voltage vectors differ only in phase by 6 degrees, giving a 0.25 mm repositioning accuracy requirement at 18 GHz (smallest wavelength). Background suppression of the direct reflected signal off the parabolic reflector edge (to be discussed in Section 5.2) indicated that the scanner structure was built and aligned adequately and that the repositioning precision was also sufficient.

2.5 Probe Characteristics

Johnson et.al. [11] suggest the following probe characteristics; (1) Small aperture for point measurement and broad beam width, (2) Polarization should be accurate and stable, (3) Probes the size of $\lambda/2$ dipoles or smaller are needed for accurate measurements but probes with more directivity than $\lambda/2$ dipoles produce large measurement errors.

To reduce the time required for each data set scan, different scanning antennas can be used. Cown and Ryan [9] suggest the use of arrays of modulated scattering elements or electronically scanned antenna arrays to accomplish one of the dimensions of the scan plane. Since this could reduce the dimension of the scan by one, the data measurement times for these antennas are shown to be dependent on N rather than N^2, where N is the number of sample positions along one direction of the scan plane.

In classical near field measurements, probe compensation is used to remove the effect of the probe directivity and increase measurement accuracy. In our tests of the scanning system, probe compensation was not employed. The probe antenna used was an AEL model H-1498, 2-18 GHz rectangular horn. The same type of horn was used as the feed for the compact range reflector. The probe antenna mount allowed a 90 degree rotation for both vertical and horizontal polarization measurements. The

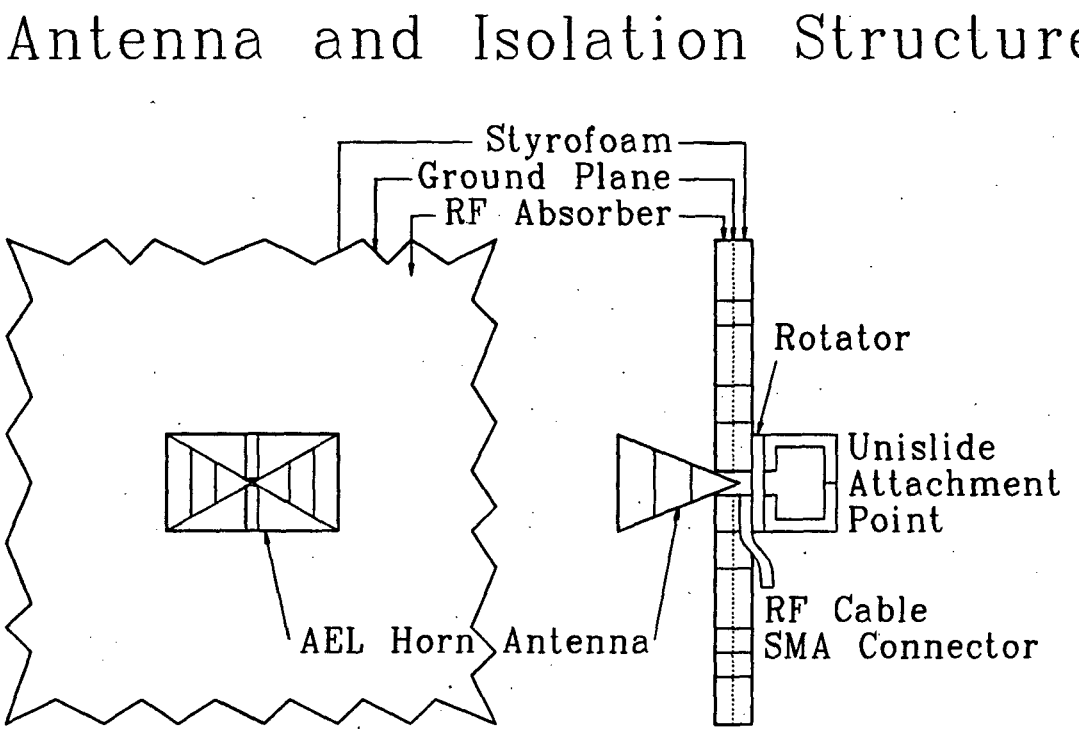

Figure 2.2: Probe Antenna and isolating absorber.

principal plane patterns of the AEL horn antenna have a maximum ± 1 dB taper or ripple, and a 20 degree maximum taper over a 30 degree beamwidth for frequencies of 2 to 18 GHz. The side lobes of the AEL horn antenna were down at least 20 dB from the main beam. Since the angular sector of interest was only 20 degrees wide and the scanner was not located in the extreme near zone of the target, the AEL horn nearly simulated an omni-directional antenna for that reduced angular sector. If desired in future analysis, including probe compensation requires no new measurements since probe compensation is implemented during the data processing.

The scanner support structure effect on the measured data could be reduced by covering the support structure with RF absorbing material or isolating the antenna from the scattering of the structure by the use of an absorber covered ground plane. This second approach was used to design the antenna "isolator" shown in Figure 2.2. The randomly placed serrations placed on the edges of the absorber coated ground

plane were intended to break up the edge diffraction fields coming from behind the antenna. A hardware range gate was used to gate out signals such as the scattering off the support structure interacting with the room and target and then being received by the scanner. Measurements taken along a linear horizontal cut of the scan aperture did not indicate the presence of any signals due to the vertical struts of the support structure.

2.6 Scanner to Test Target Separation Distance

2.6.1 Multiple Interactions

All possible reflection paths from the target to the scan plane via walls and support structures are designated multiple interactions. To experimentally estimate the effect of multiple interactions, Yaghjian [8] suggested varying the spacing between the scan plane and target as a function of the wavelength. Amplitude variations of period one half wavelength will be caused primarily by double bounce reflections. Multiple interactions can also be reduced by increasing the scan surface to target separation allowing for hardware range gating and spherical wave propagation amplitude decay. The prototype scanner system's aperture to target separation was 17 feet making the double bounce from target to scanner out of the hardware range gate. Efficient use of absorber can also contribute to amplitude decay of the multiple bounce signals.

2.6.2 Evanescent Waves

An evanescent wave's constant phase plane is not parallel to its direction of arrival. Thus its propagation constant can be greater than k_o, the free-space propagation constant along a given direction [12]. Due to these characteristics, the evanescent wave effects should be minimized. One solution is to place the antenna array far enough away from the scatterer such that the evanescent waves are attenuated by the distance. In a compact range environment this criteria is easily met by placing the scanner at a sufficient distance to the side of the main beam of the parabolic reflector.

Joy and Paris [13] formulated the minimum attenuation α_{min} of all evanescent waves which cannot be recovered by sampling at $\Delta S < \frac{\lambda}{2}$.

$$\alpha_{min} = 54.6N \left[\left(\frac{\lambda}{2\Delta S} \right)^2 - 1 \right]^{\frac{1}{2}} \qquad [dB] \tag{2.3}$$

where

λ = Wavelength

N = Distance in wavelengths

ΔS = Sample spacing

For a sample spacing of 2.54 cm at 2 GHz and a scanner to target separation of 210 inches, the minimum attenuation of evanescent waves is 5460 dB. Assuming that the only effect of sampling at greater than $\frac{\lambda}{2}$ is the occurrence of grating lobes and that the evanescent waves come only from the target, this value of evanescent wave attenuation is valid over the 2 to 18 GHz frequency range.

2.7 Summary

Some of the important parameters to consider in the design of a near field scanner have been presented and modifications of published standards of accuracy and precision were given. Joy [3] makes an exhaustive list of parameters to consider in the design and evaluation of a planar near field scanner system. Two unusual concerns mentioned were that motion during data measurement can induce Doppler effects on the received frequencies and that Teflon has a phase anomaly at room temperature [3].

Chapter 3

Mechanical Design of Planar Scanner

3.1 Support Structure

The probe antenna and motion mechanism support structure was constructed of aluminum U-channel in triangular sections for rigidity. An orthographic projection geometry of the scanner support structure is presented in Figure 3.1. Assuming ideal point joints and zero bending moments, the support structure is perfectly rigid since the triangular sections are incapable of deformation. The front rectangular face of the ideal support structure is also incapable of deformation because each side is a part of a triangular section. In the actual structure, the joints were composed of angle brackets and bolts. Once the entire structure was aligned, roll pins were inserted to prevent joint movement.

The aluminum U-channel was sufficiently rigid for the vertical and slanted brace members, however in the base configuration shown in Figure 3.2, the weight of the upright portion of the scanner support structure caused deflection of the U-channel at the mid-section of the base side beams. Feet structures, created by taping the base beams and inserting lengths of $\frac{1}{2}$ inch diameter threaded rod with a nut for counter tightening, were placed to eliminate bending moments in the base side beams. Deployment of the feet eliminated base side beam bending and increased

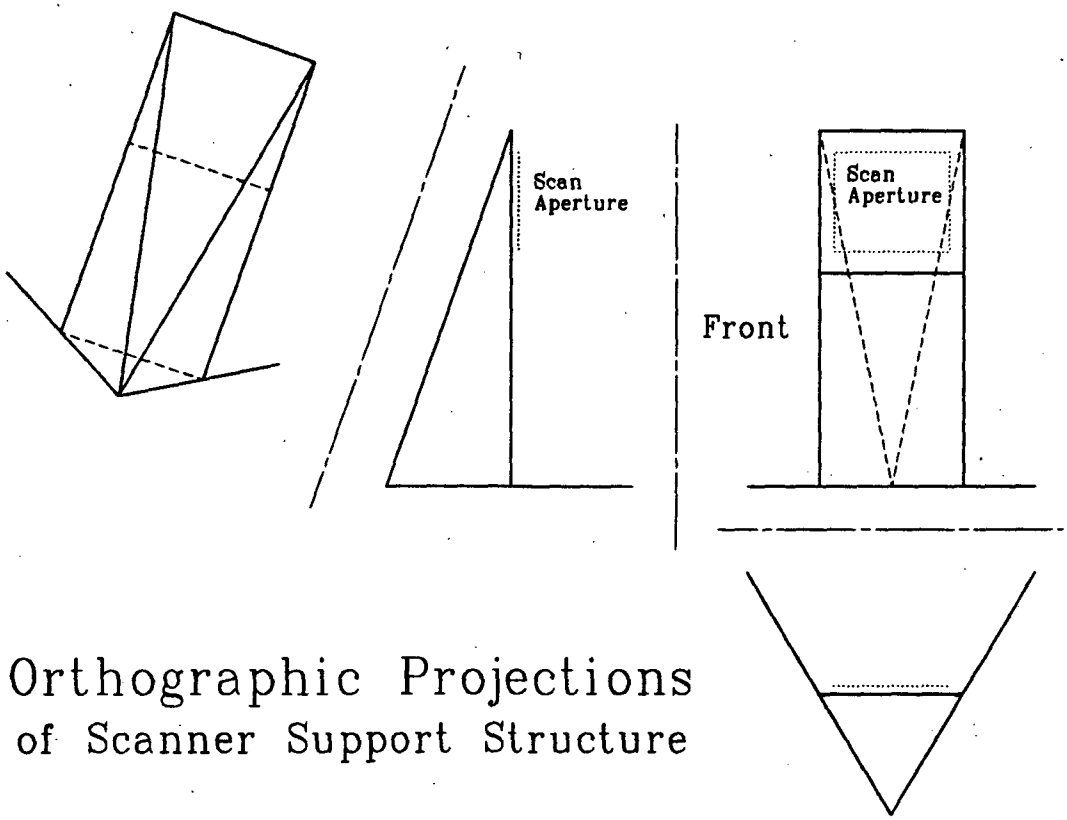

Figure 3.1: Orthographic projections of idealized scanner support structure geometry.

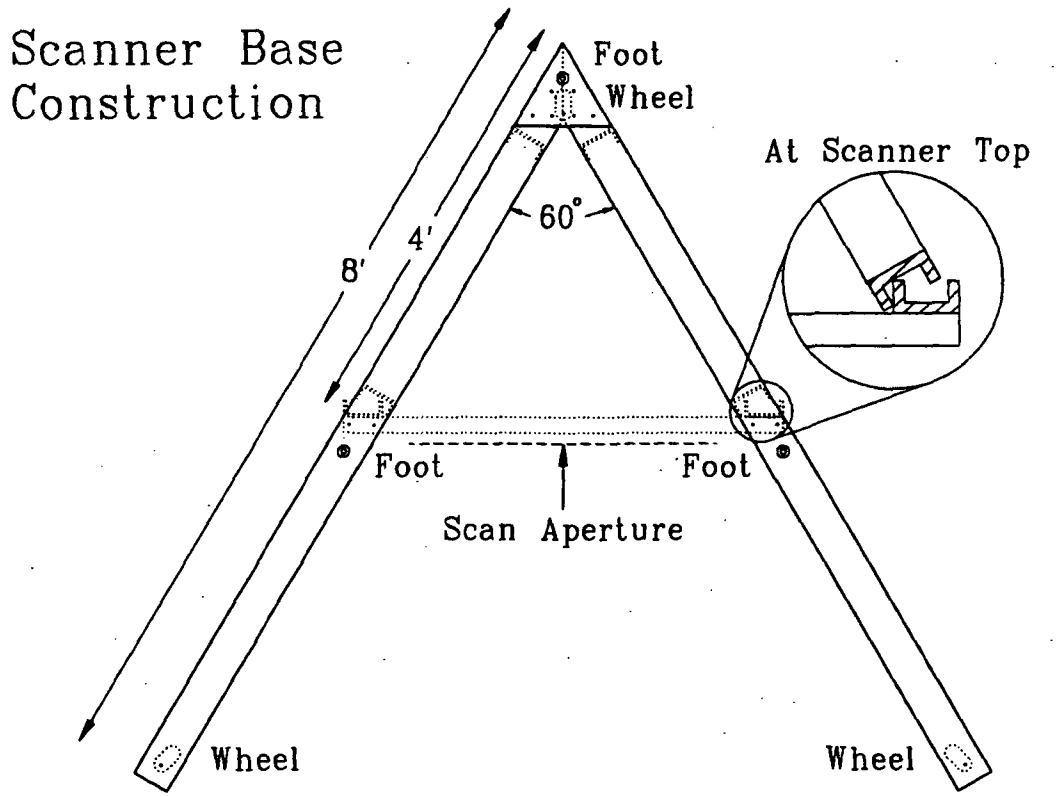

Figure 3.2: Base design of scanner support structure.

the stability of the scanner. The wheels aided moving the scanner in and around the test chamber. When located at the desired bistatic position, the feet established the scanner position by lifting the scanner and wheels up off the floor.

3.2 Motion Control

Precise motion was accomplish with the combination of Unislide assemblies and stepper motors. Figure 3.3 shows the front face of the scanner structure. The three Unislide assemblies all model number B2536W4J supplied by Velmex, Inc., Bloomfield NY had a nominal 36 inch linear motion range and a precision roll-formed lead screw with a 0.400 inch advance per revolution. The manufacturer-specified maximum-error in the direction of motion was 0.008 inches per foot (0.10 mm per 30 cm). Two types of stepper motors were used. The vertical Unislide drive motor was specified at 100 oz-in holding torque, 200 steps per revolution, with power supply requirements of 1.65V and 4.7A. The two horizontal Unislide drive motors were specified at 35 oz-in running torque, 200 steps per revolution, and power supply requirements of 5V and 1A. The combination of the Unislide's 0.400 inch advance per revolution and the stepper motor's 200 steps per revolution yielded a 0.002 inch motion per 1 motor step, which was the positioning precision of the system. Upon installation of the antenna mount structure, the Unislide assemblies range decreased to approximately 32 inches and the scan aperture was chosen to be 30 inches by 30 inches square. Loading of the horizontal Unislides by the vertical Unislide and antenna did not exceed load limit specifications.

The vertical Unislide motor power supply was a 12 volt source with 2 Ohm power resistors to give a 6A current through the motor windings at DC. The horizontal Unislide motors' power supply was also a 12 volt source with 6 Ohm power resistors to produce the specified 1A current in the two motors wired in parallel. The horizontal motors were wired in parallel to ensure that the control signals would reach both motors. At low speeds where the torque is maximum, motor torque is dependent on

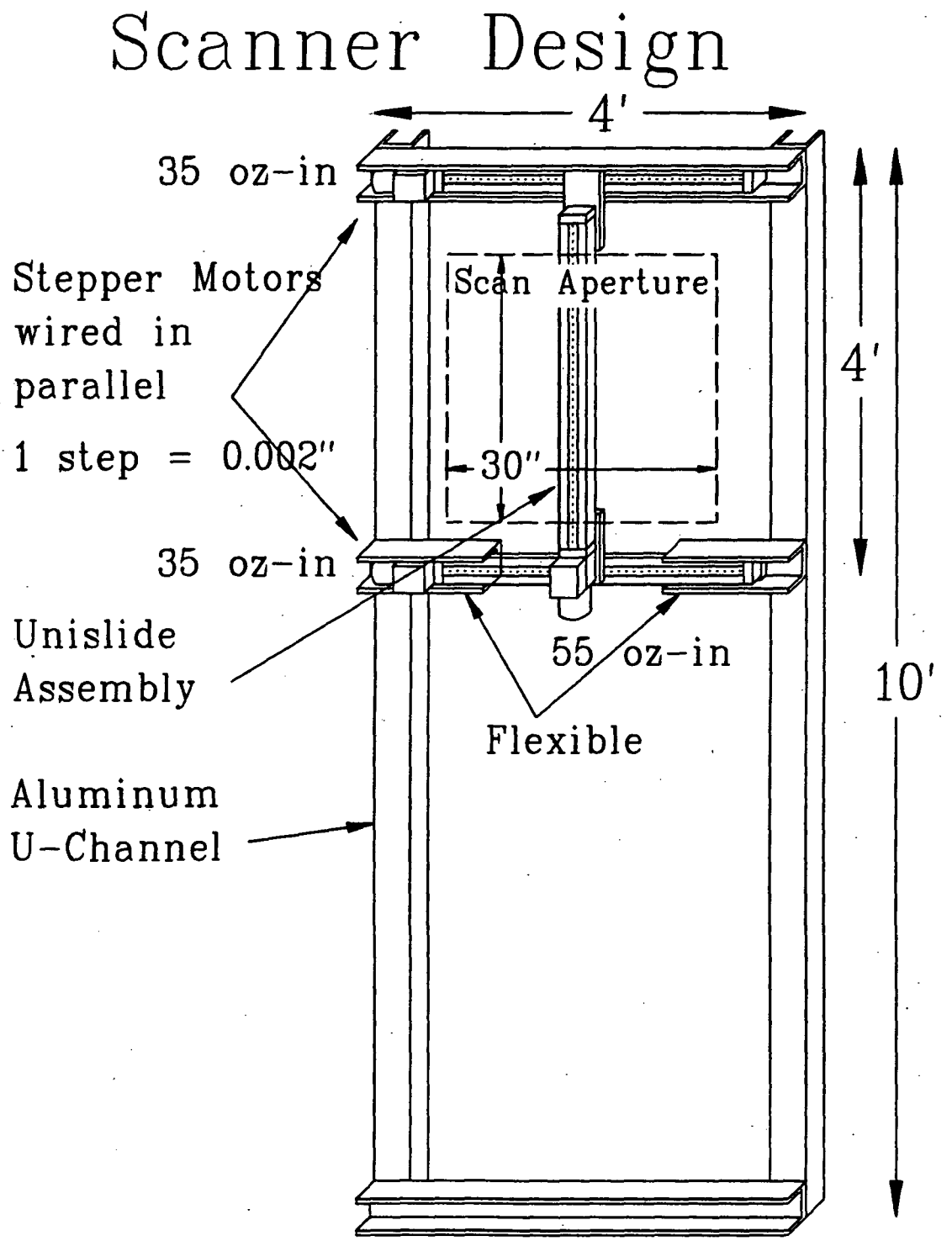

Figure 3.3: Scanner structure front face design.

the supplied current. Parallel wiring lacks a guarantee that both motors receive the same current, thus the motors were not guaranteed to produce the same amount of torque. This was a problem because the loading of the motors by the weight of the vertical Unislide and friction forces due to deviations from perfect alignment were not evenly distributed. Tests and design modifications were made to ensure proper operation of the motion system.

3.3 Open Loop Control System

An open loop control system was used for stepper motor control. Tests were performed to verify the motor response to the control signals. Two factors were explored to ensure reliable motor performance.

3.3.1 Motor Step Errors

The Unislide and stepper motor combination produced a 0.002 inch movement for each step executed by the motor. A test was implemented in which the computer instructed the motor to perform X number of steps to the right, then count the number of steps required to return to the original position. If a step was missed by the motor, the count would not match the X step number. The original position was defined by the location at which the slider "tripped" the limit switch which could be read by the computer independent of the step count. This sequence was then repeated for many trials.

An example of the type of data acquired in this test is shown in Figure 3.4. In all cases discussed here, the number X was chosen to move the slider along the entire length of the Unislide. These tests also indicated the precision of the "zero" position. During data measurement all probe locations are referenced to the "zero" position and each two dimensional scan must be referenced to the same "zero" position.

If a motor step error (a "miss") occurs, the computer count will be four steps off, since the motor's four sets of internal stator fields will not "catch up" with the

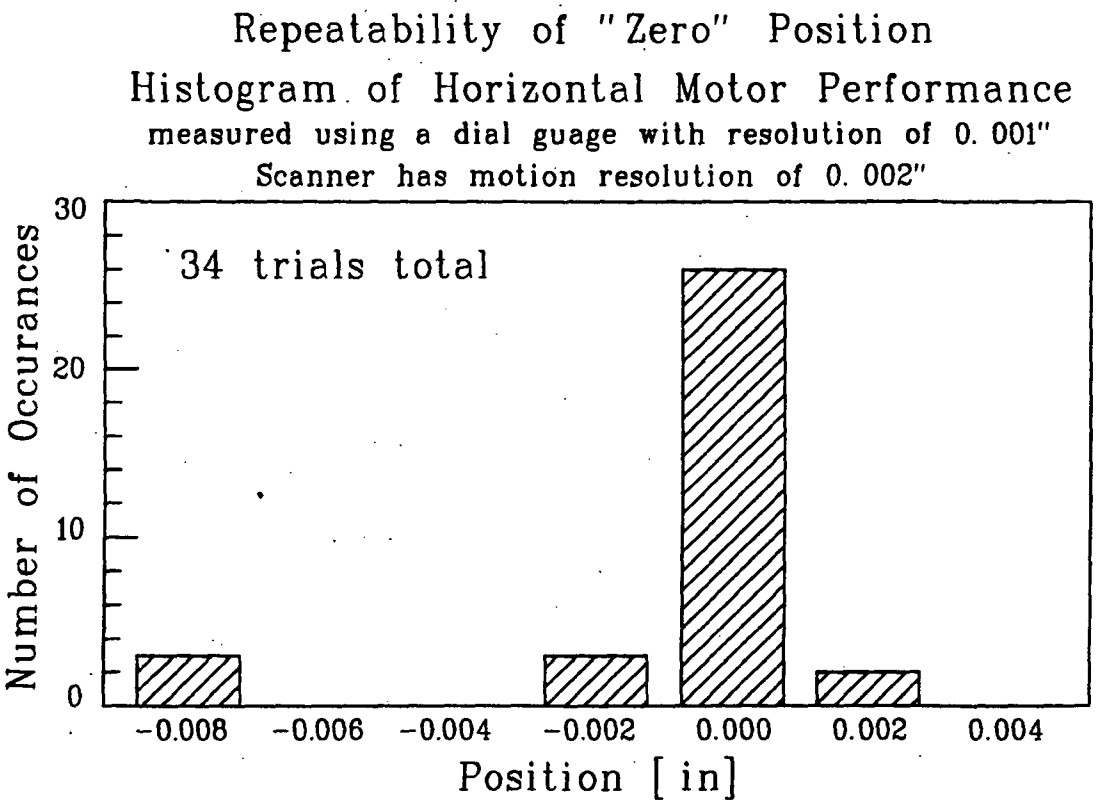

Figure 3.4: Histogram of horizontal motor pair performance indicating "zero" repositioning precision.

rotor field for four steps (± 0.008 inch). Variation in the "throw" location of the limit switch causes the ± 0.002 inch variations about the "zero" position. Note that this verifies system positioning precision of ±0.002 inches.

This test set was performed on the horizontal Unislide pair before the final modification of the vertical Unislide attachment. In 34 trials there were 3 misses – an unacceptable 10% error rate. Using the final Unislide attachment design to be discussed in Section 3.4, the same test gave no misses in 10 trials, and two days of measurements were made with the "zero" position accurate to within 0.002 inches. The vertical Unislide tests showed no motor errors in 200 trials and was assumed satisfactory.

3.3.2 Motor Torque Requirements

The zero position test could indicate the occurrence of a motor error but it did not give any information as to the cause or location of the problem areas. To investigate this, a torque profile of the horizontal Unislide pair was made using hand made pulleys and bottles of water. The testing was not extremely accurate but did give insight to possible trouble spots.

Figure 3.5 shows the results which clearly indicate an increase in the torque needed to move the slider near 30 inches. This test suggested that the attachment of the vertical Unislide was causing rotational stress on the small sliders inside the horizontal Unislides due to non-planar nature of the top and bottom Unislide alignment. The resulting design modifications from this hypothesis are presented in Section 3.4. A torque profile for positions near 30 inches on the horizontal Unislide pair with the final attachment design implemented showed the necessary torque to be reduced to less than 7 oz-in for both static and kinetic frictional forces.

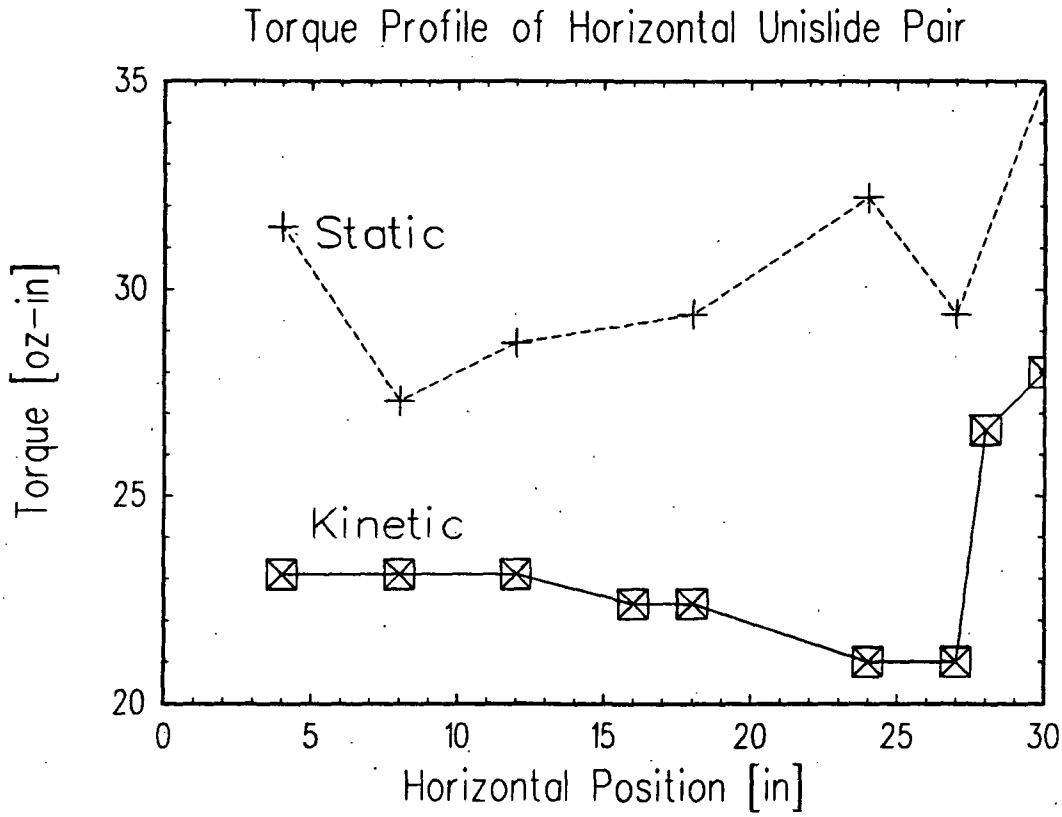

Figure 3.5: Torque profile of horizontal Unislide pair.

3.4 Alignment Procedures

The support structure was required to support the Unislide assemblies and provide alignment ability. The alignment capabilities included solidly attaching the top Unislide as the reference, and allowing the other Unislides to "float" with respect to the support structure but aligned with respect to the reference Unislide. This was accomplished by three mechanisms located at the attachment points of the bottom Unislide to the support structure, the vertical Unislide to the top Unislide, and the vertical Unislide to the bottom Unislide.

Figure 3.3 indicated the flexible nature of the attachments of the bottom Unislide to the support structure. These short attachment beams allowed deflection in the vertical direction only (approximately 2 mm under 100 lb applied force). This allowed compensation of parallel errors between the top and bottom Unislides. The attachment scheme of the vertical Unislide to the horizontal Unislides is shown in Figures 3.6 and 3.7. This attachment design was created in response to system testing described in Section 3.3. The top attachment point shown in Figure 3.6 allows rotational motion about the axis defined by the circular rod. The rubber washers reduce vibration of the vertical Unislide and antenna. The bottom attachment scheme shown in Figure 3.7 allows horizontal-plane rotational motion of the vertical Unislide due to the rubber washers. The combination of these two components of the vertical Unislide attachment scheme allows compensation for any non-planar behavior between the top and bottom Unislides. The bottom attachment point also allows vertical motion controlled by a threaded screw. This was used to evenly distribute the weight of the vertical Unislide and probe antenna between the top and bottom Unislides. The threaded screw was adjusted until neither motor could be caused to miss a step when equal loadings were applied.

The feet of the support structure were used to position the top horizontal Unislide assembly which was used as the reference for all alignments and was horizontal to within 0.1 degrees as measured by a digital inclinometer in each experimental mea-

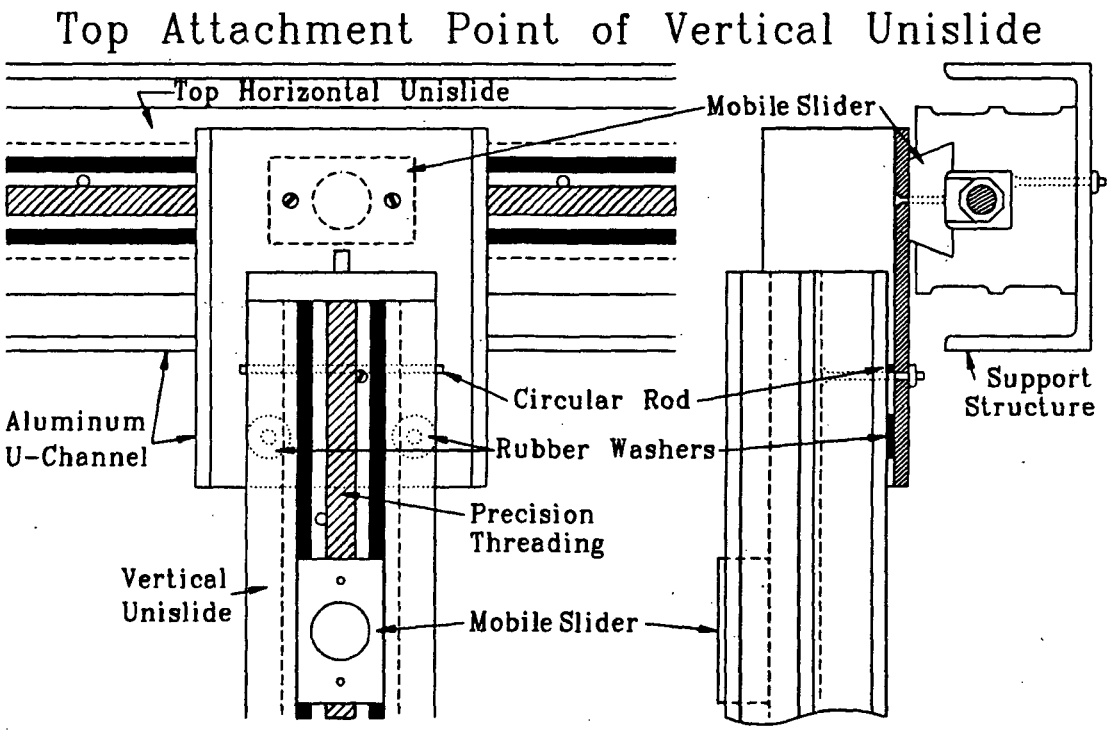

Figure 3.6: Diagram of attachment scheme of vertical Unislide to top horizontal Unislide.

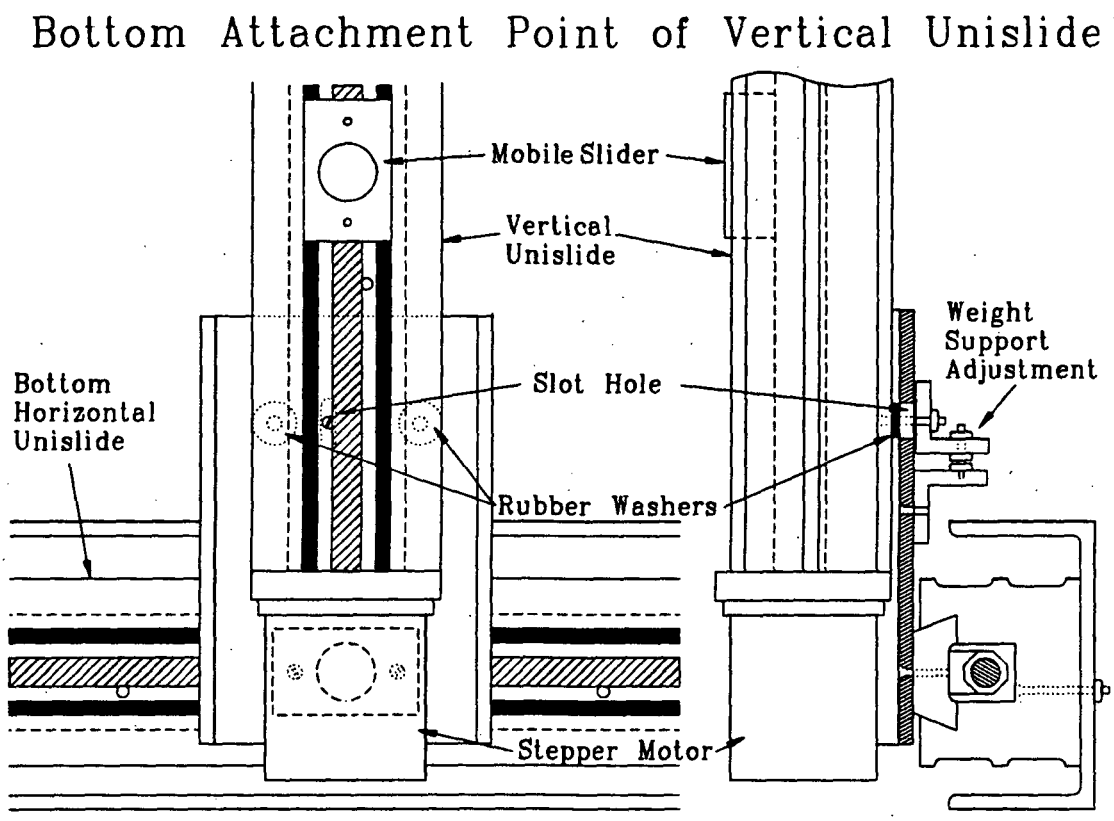

Figure 3.7: Diagram of attachment scheme of vertical Unislide to bottom horizontal Unislide.

surement set. The vertical Unislide was aligned to within 0.1 degrees perpendicular to the horizontal reference and was retained in that relationship by the application of power to the stepper motors. Note that the lower horizontal Unislide assembly is necessary to maintain perpendicularity and support part of the weight of the vertical Unislide assembly.

3.5 Positioning and Repositioning Accuracy

Positioning accuracy has been discussed theoretically in Chapter 2. The positioning of the scanner system was accurate to 0.002 inches with respect to an arbitrary fixed zero location. More important than the accuracy of the individual sample positions was the repositioning accuracy at each sample position. As discussed in section 2.4, for a 20 dB suppression of undesired background signals via a vector background subtraction algorithm, the maximum deviation in phase due to positioning error is approximately 6 electrical degrees. At 18 GHz this acceptable tolerance is 0.010 inches. Mechanical tests of the system discussed in Section 3.3.1 indicated that a more probable repositioning precision of 0.002 inches occurred.

3.6 RF Cable Routing

The routing of the RF cable from the mobile probe antenna to the stationary support structure was a concern related to the repositioning requirements. The cable must "hang" in exactly the same manner for any specific sample point, independent of previous probe antenna location. This is required because cable bending induces phase errors which are equivalent to errors in the z' direction. If background subtraction is desired, as previously mentioned, it is important that the same error whether caused by cable bending or a non-planar structure is induced each time the probe antenna is located at each particular sample point.

Chapter 4

Data Processing Procedures

4.1 Overview

Prior to data measurement, the parameters of an aperture window function were investigated to optimize the plane wave performance of a projection of the window function in the target zone. This window function, applied to the aperture data, spatially filters the received target response inducing plane wave reception. The flow diagram in Figure 4.1 shows the measurement and data processing scheme which was followed to estimate the Bistatic RCS of test targets. Each procedure is discussed in the following sections.

4.2 Aperture Taper Design

One method to design an aperture window function for a desired response is to compute the near field response of the scanner as a transmitting antenna. The reverse method, specifying the near field response and then computing the necessary aperture distribution can also be done. In this work, the planar near field scanner was modeled as a synthetic antenna array in the transmitting mode. By reciprocity, if the synthetic array can generate a plane wave region in the target zone, the planar near field scanner will receive that plane wave from the target zone. Thus, use of

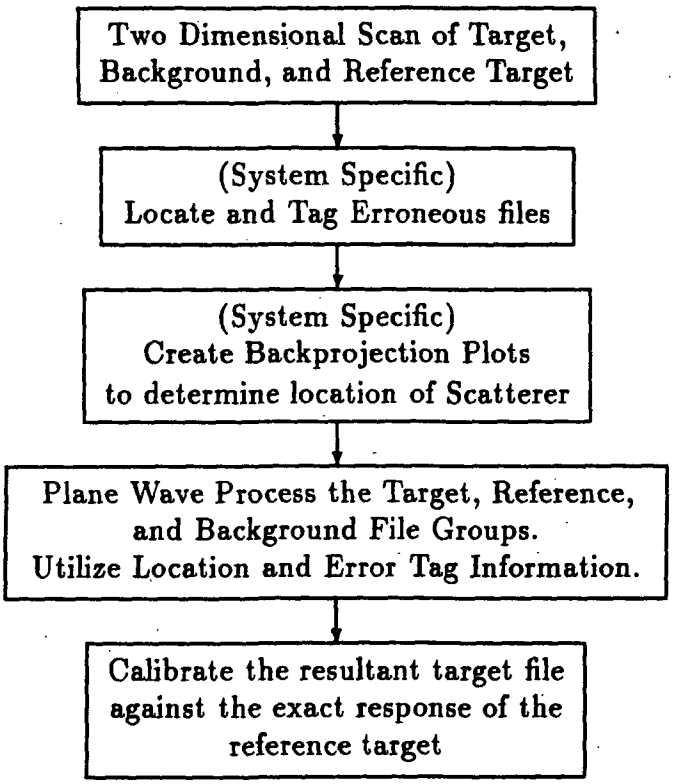

Figure 4.1: Flow Chart of Measurement Process.

the transmitting viewpoint to design the planar scanner aperture window function is justified.

The window function is illustrated in Figure 4.2 with W being the scan aperture width. The amplitude and phase taper functions serve the same purpose as the edge treatment effects of a compact range reflector with rolled edges. In a rolled edge compact range reflector the geometry transitions from a parabolic surface, which produces a constant phase and amplitude reflected signal, to a rolled edge which produces an increasing phase delay and a decreasing amplitude in the reflected signal.

With the scanner taper function, a similar transition occurs from constant phase and amplitude to phase and amplitude tapering. Referring to Figure 4.2, the amplitude taper is a cosine squared roll-off which characteristically has low side lobes, and the phase taper is a cosine function drop off with a frequency independent phase delay characteristic. Note that this is different from a parabolic reflector with rolled edges which has a frequency dependent phase delay characteristic over a range of frequencies. The aperture taper function spatially filters the measured data to suppress measurement sidelobes.

A specific taper function is denoted by the parameters (x,MPD), the percentage of the scan plane width (x% of W), and the maximum phase delay (MPD) in degrees. For example, a taper with x= 14% of W allotted to roll-off and a maximum phase delay of 90° is denoted as (14,90).

4.2.1 Taper Function "Projection" to Target Zone

To evaluate the performance of different aperture taper function parameters, the projection or response generated in the target zone was needed. The theory of "projecting" the window function to the target zone is detailed in Figure 4.3.

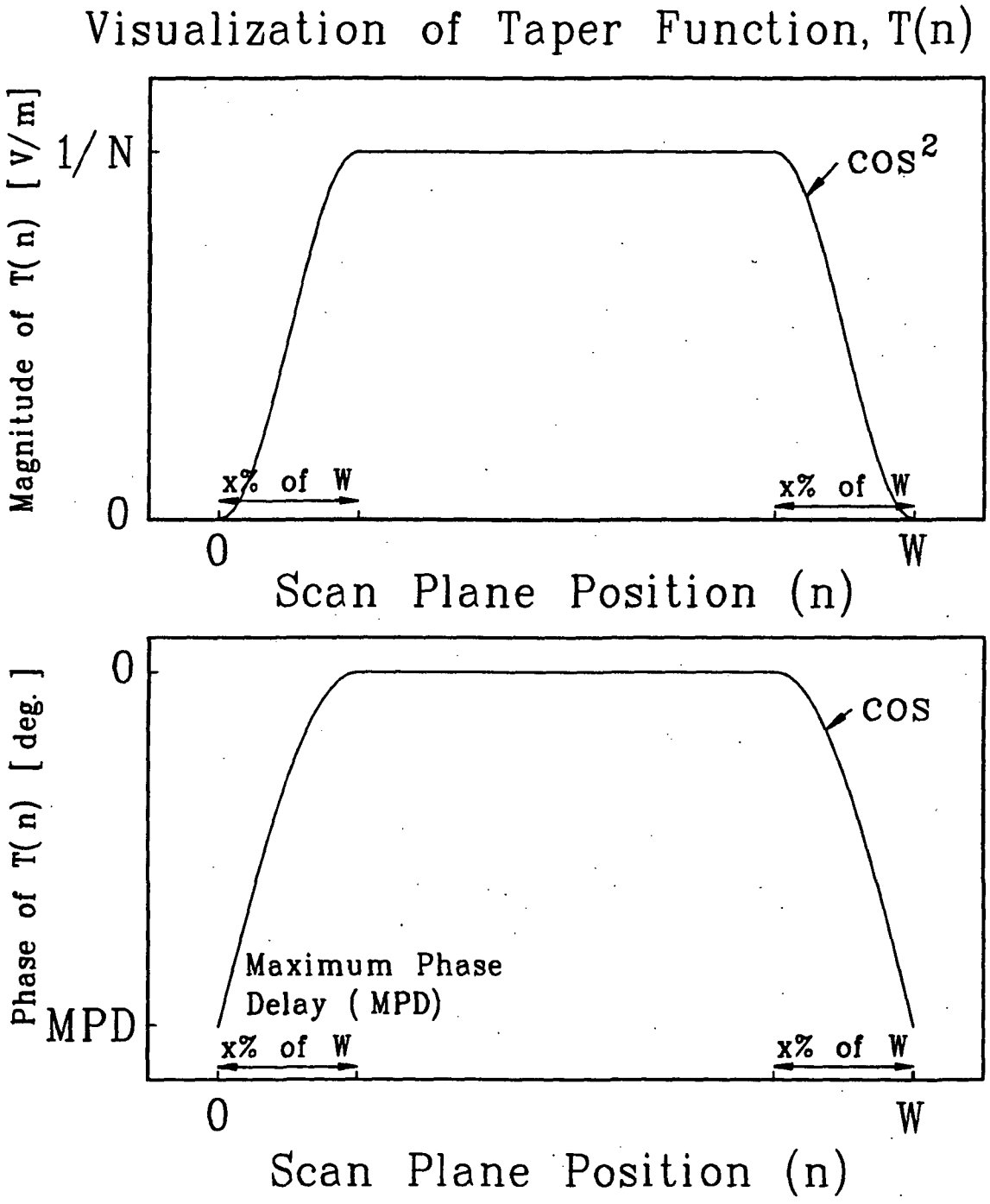

Figure 4.2: Visualization of the aperture taper function.

The projection algorithm is based on a point by point summation of spherical waves. Each field point in the quiet zone is the resultant sum of contributions from each source element antenna in the scan plane. Normalization of the E_n sources in the scan plane by N, the number of array elements, gives a constant output power independent of the numbers of array elements.

4.2.2 Taper Parameter Investigation

A computer program was implemented which output the resultant effective "width" of the projected response in the target zone as a function of the taper parameters x (0–50% of W), the maximum phase delay (0–180°), and frequency (2–18 GHz). The definition of "width" was the portion of the projected response which contained a maximum ±1 dB and ±10 degree ripple. This program was incremented independently in x by 10%, MPD by 10 degrees and frequency by 2 GHz steps in an automated process to find the parameter values which gave the "widest" target zone plane wave response. Smaller incrementation of the program yielded two sets of values with similar window "widths" for the 2 - 18 GHz frequency range: (14,90) and (40,120) where the notation is (x%,MPD in degrees). Figure 4.4 shows the (14,90) and (40,120) taper functions' magnitude and phase projected 17.5 feet in front of the scan aperture to the target zone. The patterns in Figure 4.4 are the E-field amplitude and phase that result in the target zone from the excitation of the synthetic array antenna in the scan plane. They are one-dimensional cuts through what are actually two-dimensional patterns.

In this work, the scan plane array element pattern function was set to 1 for all θ_{nm} (simulating an isotropic radiator), the scan plane width W, was 30 inches, and the sample spacing was 1 inch. The target to scan plane separation was 17.5 feet. Note that at 18 GHz, the (14,90) projection has amplitude ripple of ±1 dB over an approximate 17 inch width resulting in an aperture efficiency of 56% as compared to the (40,120) projection which has an amplitude taper of ±1 dB over an approximate

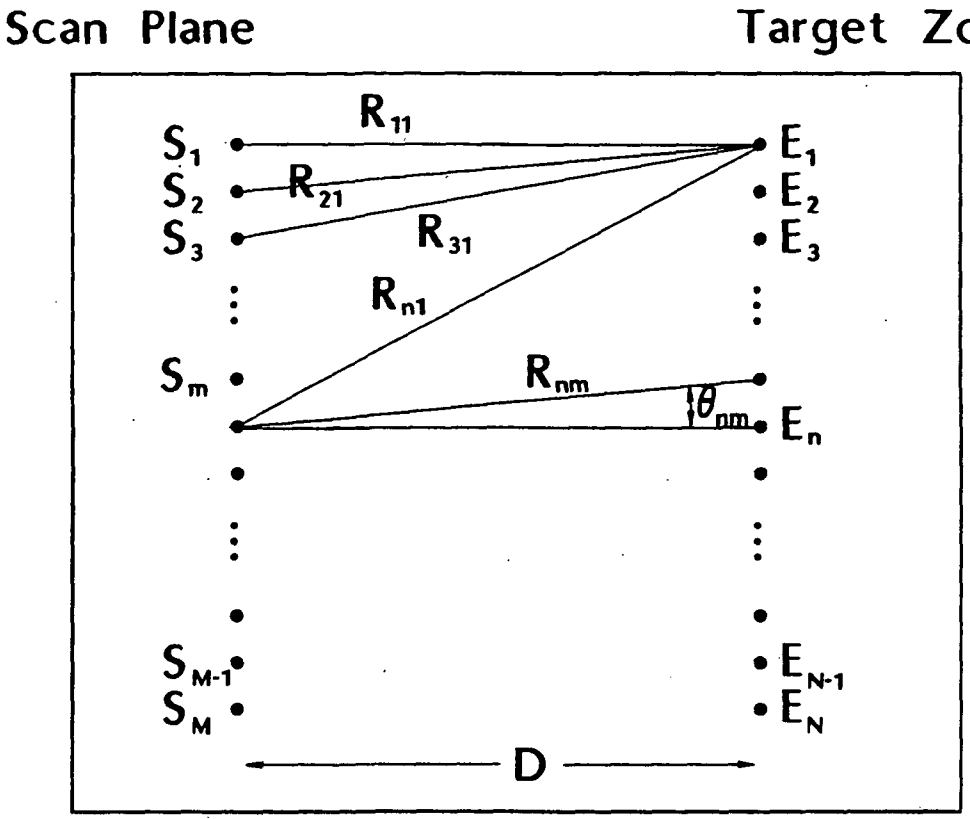

$$E_m = \frac{1}{N} \sum_{n=1}^{N} T(n) P(\theta_{nm}) \frac{e^{jkR_{nm}}}{R_{nm}} \tag{4.1}$$

where

E_m	=	Computed projection in the target zone
S_n	=	$T(n)P(\theta_{nm})$
$T(n)$	=	Taper function
$P(\theta_{nm})$	=	Scan plane element pattern
θ_{nm}	=	Angle of line from n^{th} to m^{th} elements
R_{nm}	=	Distance between n^{th} and m^{th} elements
N	=	Number of elements in scan plane
D	=	Distance between scan plane and target zone

Figure 4.3: Visualization of equation used to analytically project the aperture taper function to the target zone.

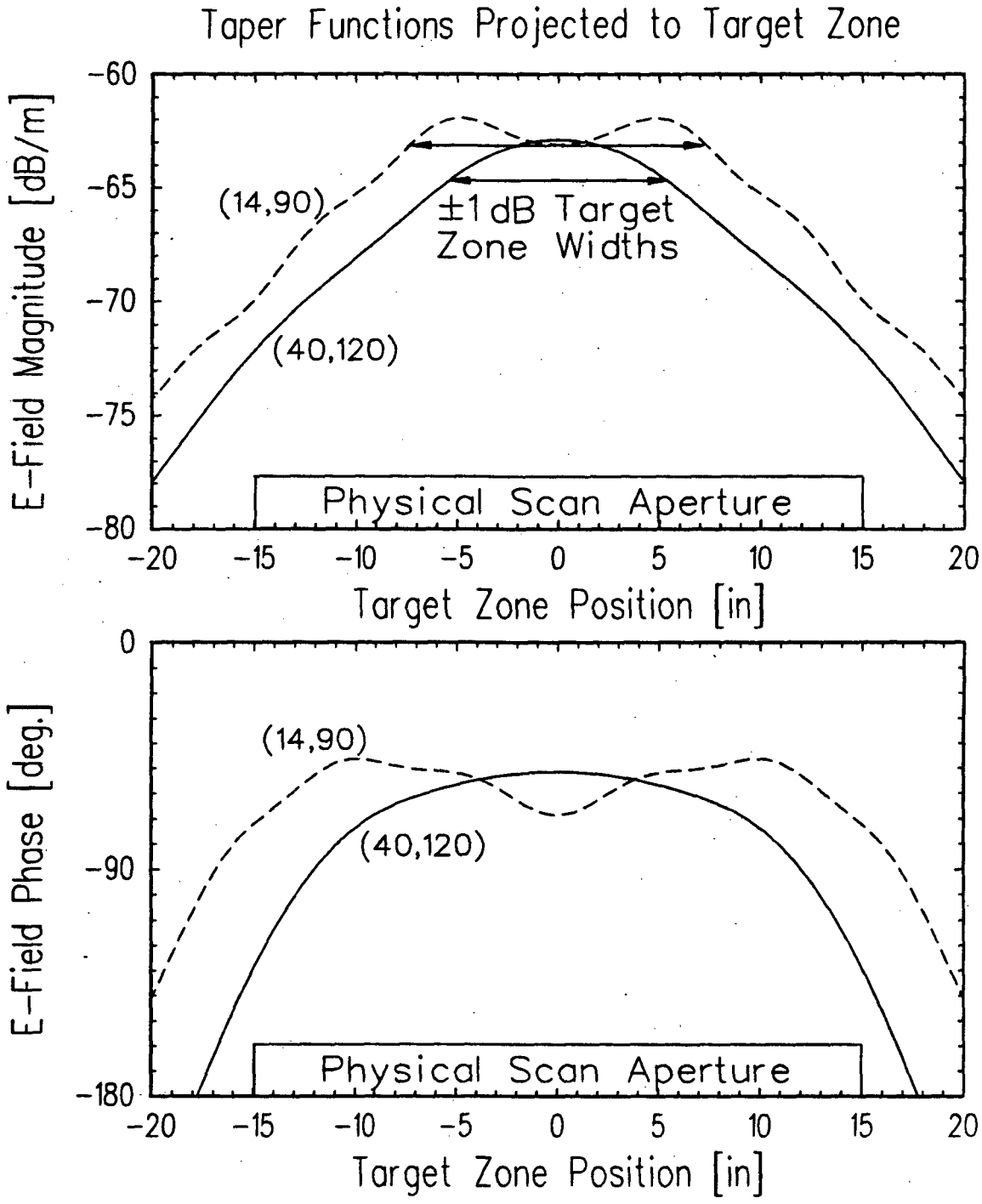

Figure 4.4: Taper functions (x%=14,MPD=90) and (x%=40,MPD=120) projected to the target zone, 18 GHz.

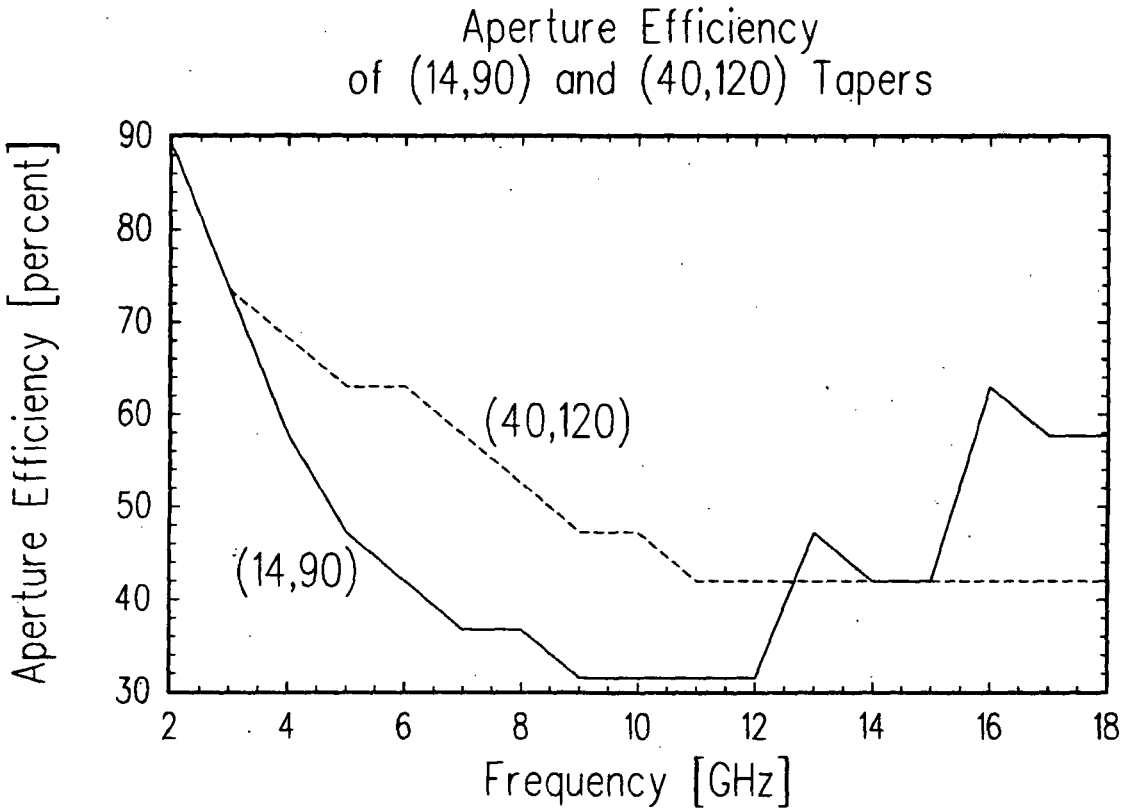

Figure 4.5: Aperture efficiency of (x%=14,MPD=90) and (x%=40,MPD=120) taper functions projected to the target zone as a function of frequency.

11 inch width resulting in an aperture efficiency of 37%. The aperture efficiency as a function of frequency of these two taper functions is shown in Figure 4.5. Note that for some frequencies the (40,120) taper has a greater aperture efficiency. Scanning is not necessary for some target and frequency combinations since the $\frac{2D^2}{\lambda}$ far field definition criteria is satisfied. For example, at 18 GHz a target 8.3 inches or larger already satisfies the far field criteria. At 2GHz (and thus the entire frequency band), a 25 inch target or larger will be in the far field. This explains the increase in aperture efficiency at the lower frequencies for both taper functions. These two window taper functions will be used in the data processing and the results compared.

The effects of (1) amplitude and phase taper variations, (2) increasing the element spacing, ΔS, beyond $\lambda/2$, (3) changing the distance between the test zone and scan plane, and (4) the response of this computer model to frequencies from 1 to 35 GHz are reported by Tuhela-Reuning and Walton [14].

4.3 Erroneous File Detection

Due to what appears to be a synthesizer problem, there was a 5 percent error rate in the approximately nine thousand measurement files created. The cause of the error has not yet been positively identified, and re-measurement of the data was too costly. Therefore, a procedure for error control was established. The errors were difficult to detect in uncalibrated raw data files and were only noticeable after calibrating the target data using the background and reference targets on a position by position basis. Groups of these calibrated files were plotted in a format where each subsequent file was artificially displaced in the y direction. This type of plot, named waterfall–plot, clearly indicated the erroneous files. Figure 4.6 is an example of the waterfall plots used to detect the error files "by hand." This was a system specific error, which affected several other research groups in the time period of the measurements for this project.

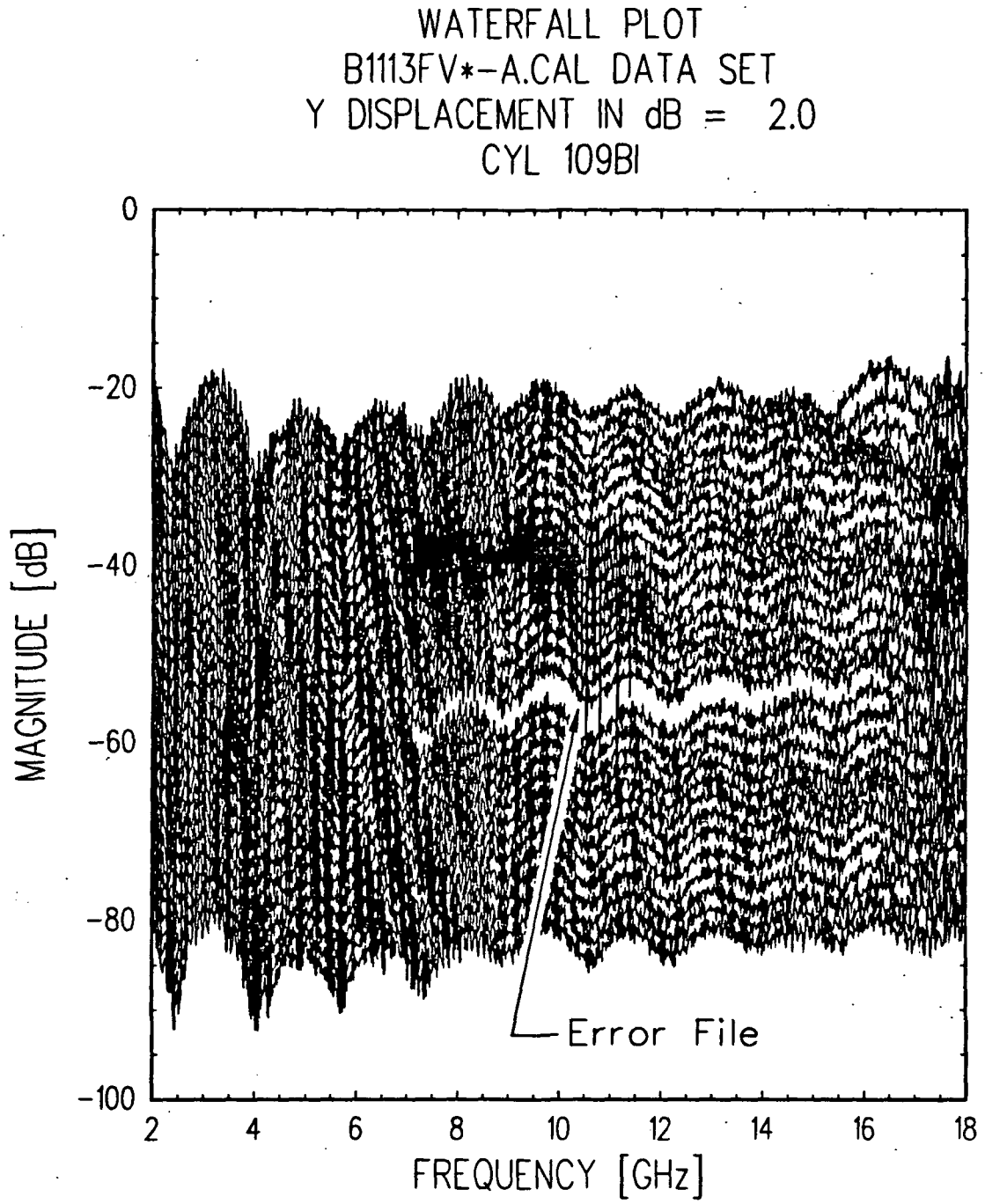

Figure 4.6: Waterfall plot of calibrated measurements used in detection of erroneous files.

4.4 Backprojection Algorithm

The backprojection algorithm was necessary to determine the location of the test target scattering centers. For the prototype scanner system built, the scan aperture was only 30 inches by 30 inches. The resulting target zone plane wave approximation section is typically only 50 percent of the aperture size. Due to small offsets in alignment of the scanner structure relative to the location of the test target and the change in location of the scattering centers for different targets, there was a need to steer or aim the main beam of the scanner to intercept the specular scattering term of the different targets. Therefore, a method which indicated the location of the scatterers intrinsically derived from the measured data (not test geometry length measurements) was used to provide the information for the aiming procedure.

The backprojection algorithm is a near field focused technique which reverses the effects of spherical wave propagation on the probe antenna measured data, and reconstructs the fields in the target zone [15]. The algorithm is displayed in Figure 4.7. Note that the only dimensions needed are the width of the scan aperture, the sample spacing, and the distance R_o. Not detailed in Figure 4.7 is the windowing of the aperture data S_m, set by a cosine squared taper as suggested by Beard [15].

Each focus-cell position is the sum of the measured fields of the m probe antenna positions with amplitude and phase adjustments related to the backprojected distance R_{nm}. The amplitude adjustment in equation (4.2) compensates for the energy density loss in an outward propagating spherical wave, and the phase term adjusts for the distance traveled, R_{nm}.

Avoidance of erroneous files was accomplished by locating a row and column from the two dimensional scan which did not contain any error files. The algorithm was verified by comparing the backprojection response curves to the measured geometry of the target and pedestal configuration for the 6 inch diameter and 18 inch diameter spheres. This is shown in Figure 4.8.

In this figure it is seen that the backprojection algorithm accurately locates

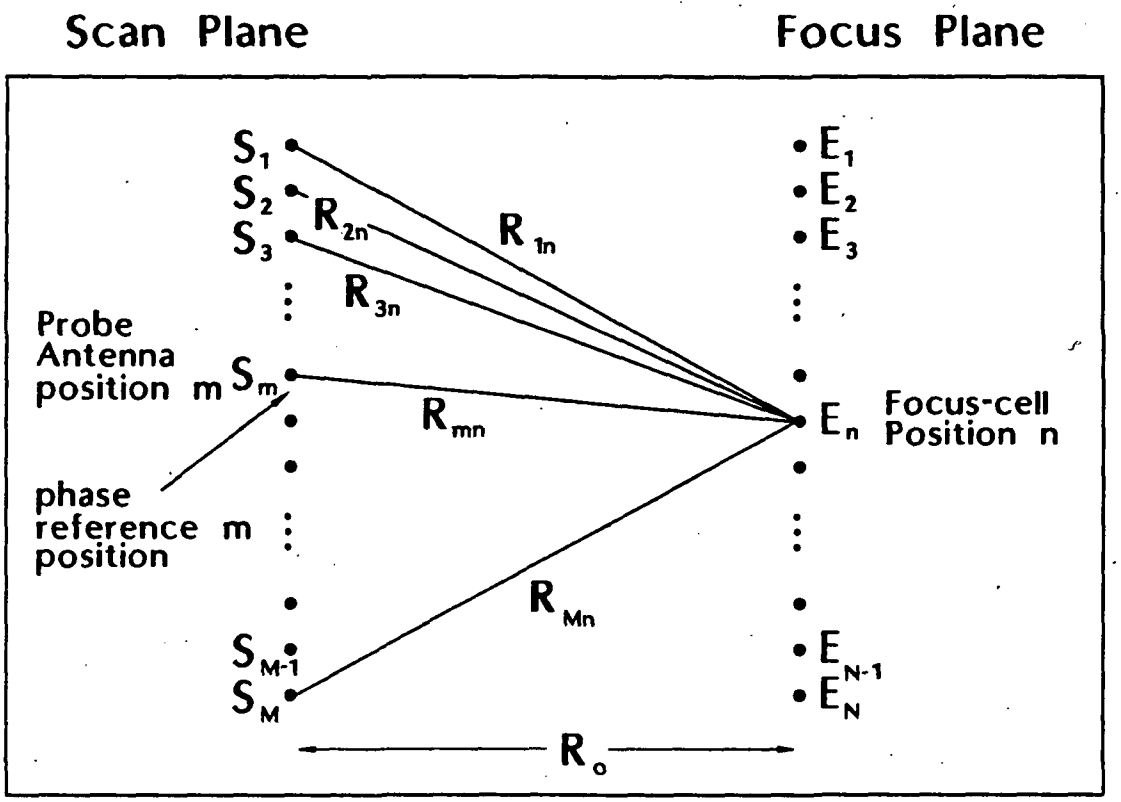

$$E_n = \frac{1}{M} \sum_{m=1}^{M} \left[\frac{R_{nm}}{R_o} \right] S_m e^{jkR_{nm}} \tag{4.2}$$

where

S_m	=	Measured m^{th} probe antenna amplitude and phase
E_n	=	Computed n^{th} focus-cell amplitude and phase
R_o	=	Distance between scan plane and focus plane
R_{nm}	=	Distance between n^{th} and m^{th} elements
n	=	Focus-cell position
m	=	Probe antenna position

Figure 4.7: Visualization of focused backprojection algorithm.

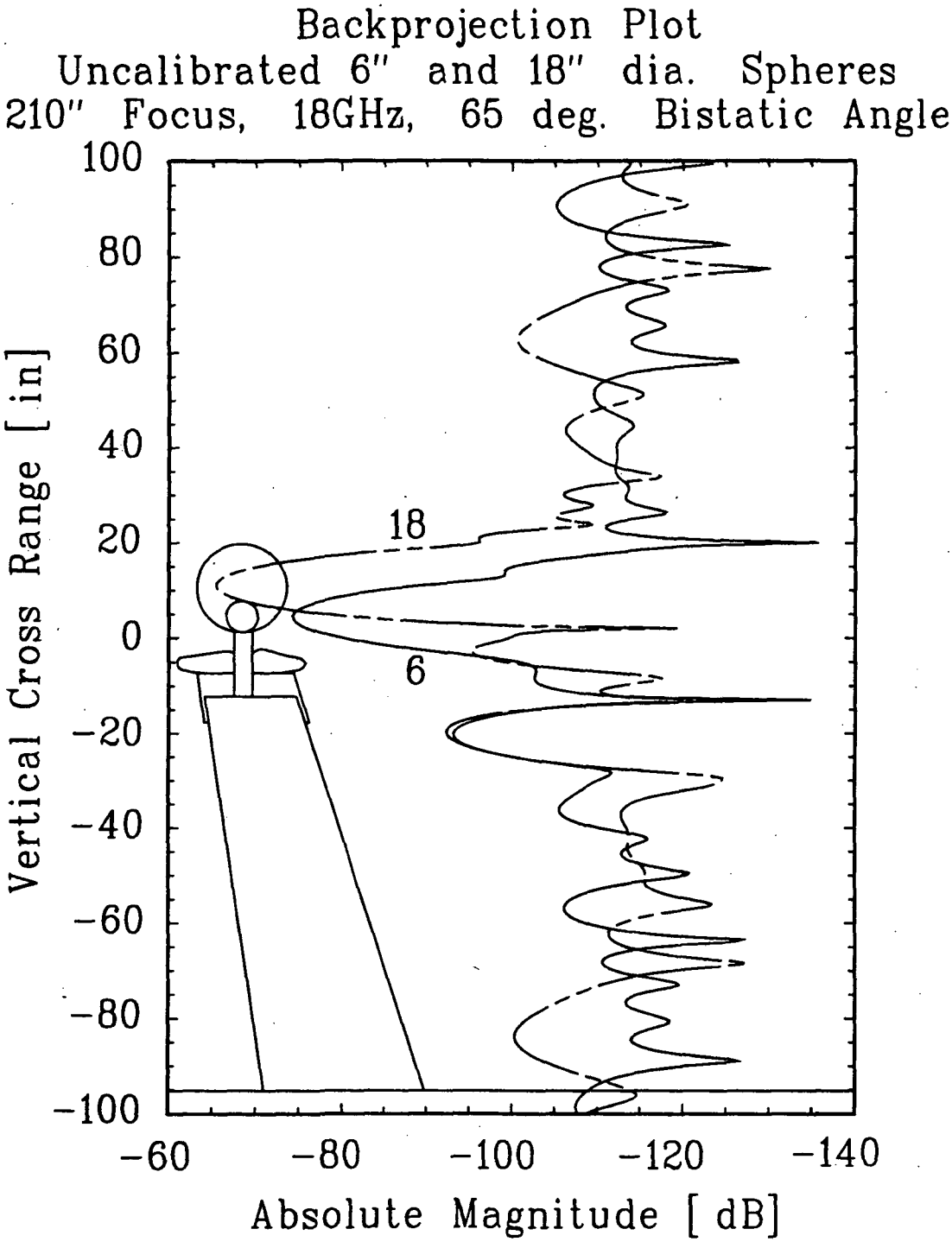

Figure 4.8: Backprojection plots for uncalibrated 6 inch diameter and 18 inch diameter spheres with overlay of target and ogival support structure geometry, 18 GHz.

Target	x' [in.]	y' [in.]
18 in. diameter Sphere	-1	11.0
6 in. diameter Sphere	-4	4.5
Cylinder	-5	2.5

Table 4.1: Target scattering center positions, 65 degree bistatic angle

the specular scattering terms of the two spheres to within approximately an inch resolution. This accuracy is sufficient for the aiming procedure due to the large size (with respect to one inch) of the plane wave section generated in the target zone by the scan plane taper function. It is also interesting to note the term which appears to emanate from the junction of the metal ogival support and absorber cap for both the 6 and 18 inch diameter sphere cases. This strongly suggests a bistatic scattering response from the support structure.

To locate the position of the specular scattering term of each target, two one-dimensional backprojection plots were made, one each in the horizontal and vertical directions. Along with the knowledge of the target to scanner separation, these plots provided information which could locate the specular scattering of the test target in three dimensions. Figure 4.9 shows both a horizontal and vertical backprojection plot of the 6 inch diameter sphere at 65 degree bistatic angle.

The zero position in Figure 4.9 corresponds to the z' axis of the scan aperture (see Figure 2.1) and is directly in front of the middle of the scan plane aperture. The location of the scattering from the sphere is seen as 4 inches to the left of and 4.5 inches above the middle of the scan plane. These offset distances were obtained by increasing the scale of the backprojection plot over the scale of Figure 4.9.

Tables 4.4 and 4.4 contain the scattering center position of each target measured. This information was used in aiming the beam of the scanner during plane wave processing.

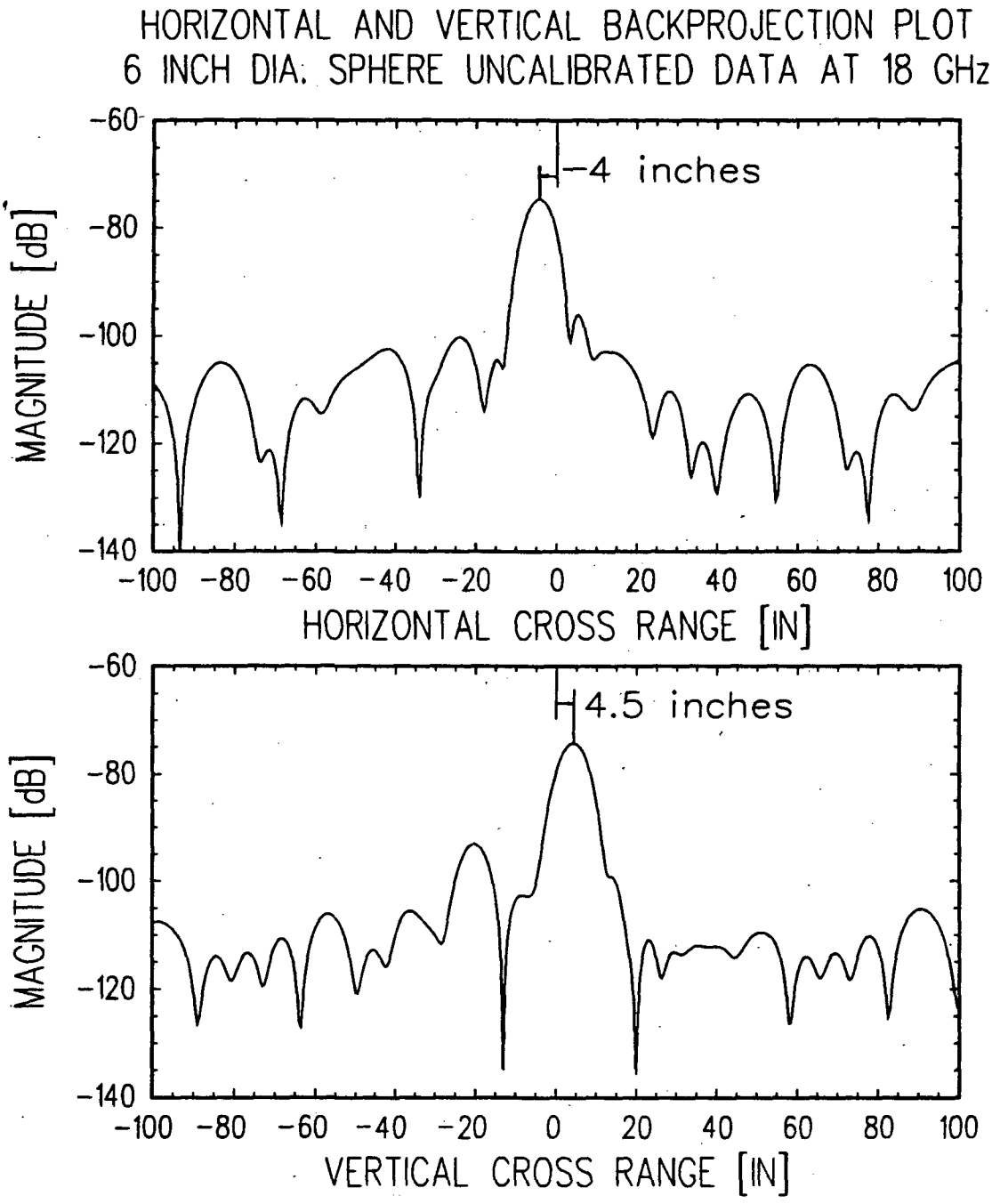

Figure 4.9: Horizontal and vertical backprojection plots of 6 inch diameter sphere, 65 degree bistatic angle, 18 GHz.

Target	x' [in.]	y' [in.]
18 in. diameter Sphere	9	9.5
6 in. diameter Sphere	5	3.5
Cylinder	3	2.5

Table 4.2: Target scattering center positions, 109 degree bistatic angle

4.5 Beam Aiming Process

The necessity of using beam aiming for the 30 inch square scan aperture has already been discussed in Section 4.4. However, it should be noted that beam aiming would not be needed for a larger scan aperture system with a plane wave region large enough to completely cover the test target. The aiming process is implemented by introducing a phase difference term ΔP, which is a function of the aim angle, into each antenna measurement. Referring to Figure 2.1 for coordinate definitions, if the desired aim angle is (θ,ϕ) then the aiming equation is

$$A_n = S_n e^{jk\Delta P} \tag{4.3}$$

where

$$\begin{aligned} \Delta P &= \Delta S \sin(\theta)\cos(\phi) \\ A_n &= \text{aimed data set} \\ S_n &= \text{measured data set} \end{aligned}$$

Over the aperture, this corresponds to a linear phase gradient applied to the measured data. The aim direction is only changed to intercept the specular term of the test target since the scan aperture generates too small of a plane wave region. The aiming was not used to sweep the bistatic angle across the target zone. The Fortran code for the aim process which was implemented in the same program as the plane wave processing is included in appendix 8.

4.6 Plane Wave Processing Algorithm

The plane wave processing procedure performs the estimation of the far field scattering response from the scan aperture data set. Ideally, the scanner would receive only a single plane wave from the test target. However, in practice many plane waves are received by the scanner and the plane wave processing must filter out the plane waves which do not have near normal incidence angles. An intuitive understanding of this process is that the spatial windowing decreases measurement sidelobe levels and acts as a plane wave filter. The algorithm is illustrated in Figure 4.10.

Each measurement file contains a frequency sweep from 2 to 18 GHz at a single location in the scan aperture. The frequency sweep files are organized by position into a three dimensional array in x, y, and frequency. The window function, discussed is Section 4.2, is applied to the x-y plane at each individual frequency, spatially windowing the measured data. The application of the window function at each individual frequency allows for a window function which is unique to each frequency value, but this was not explored in this work. After spacial windowing, each x-y frequency layer is summed over x and y and normalized by the number of elements and a power correction factor (not shown) which corrects for the power loss in the windowing process. The power correction factor (PCF) for a one-dimensional aperture is

$$PCF = \left[\frac{100}{100 - (x)}\right] \tag{4.4a}$$

and for a two-dimensional aperture is

$$PCF = \left[\frac{100}{100 - (x)}\right]^2 \tag{4.4b}$$

where x is the taper function parameter, x% of W.

The summations result in far field estimates of the bistatic scattering at each frequency which are then returned to a frequency sweep file format and stored for later calibration. The FORTRAN computer code which executed this procedure is included in appendix 8.

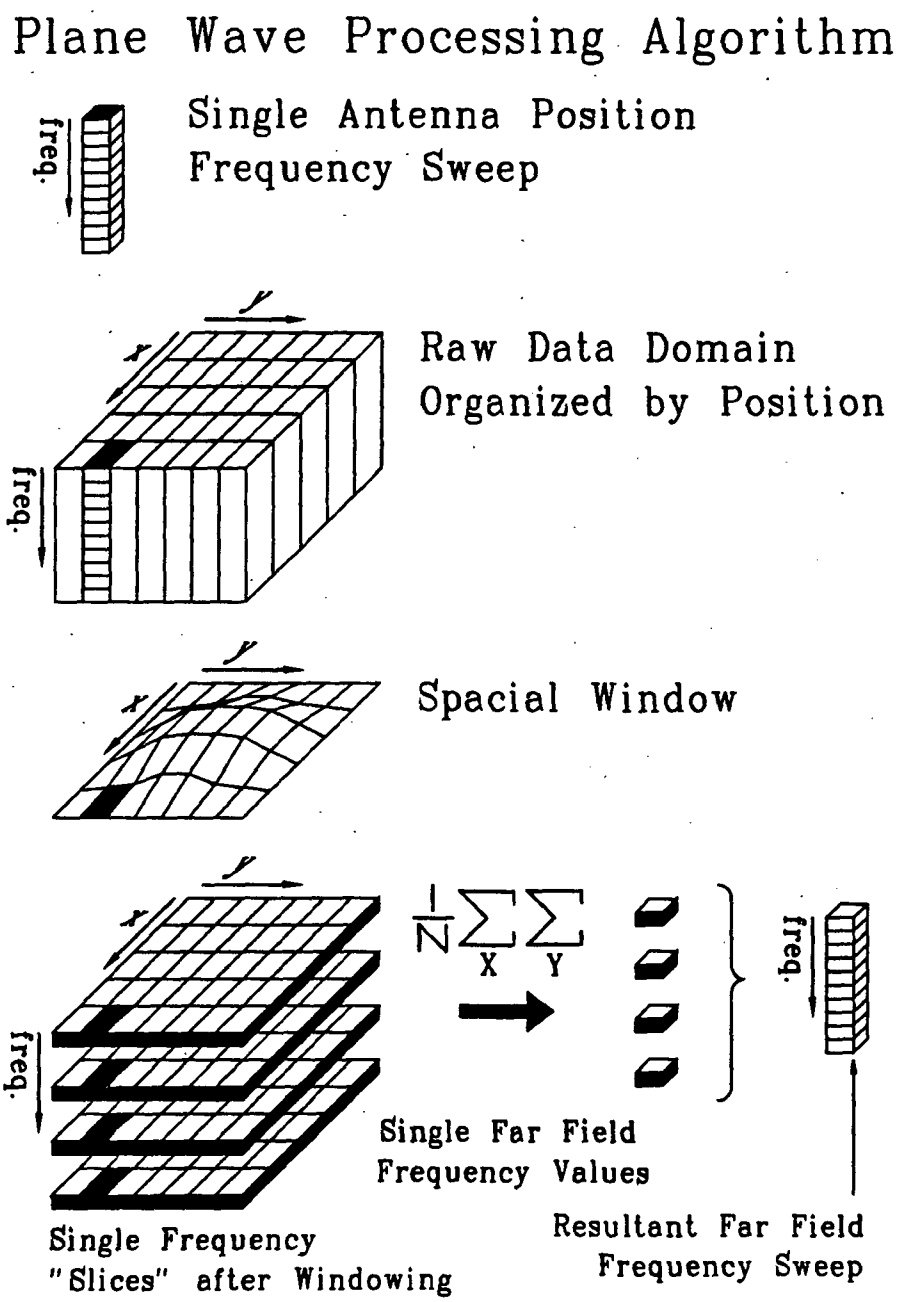

Figure 4.10: Illustration of Plane Wave Processing Algorithm.

Comparing the plane wave processing algorithm to the plane wave spectrum near field to far field transformation equations (4.5) given by Yaghjian [2],

$$E_t(x,y,z) = \frac{1}{2\pi}\int_{-\infty}^{\infty}\int_{-\infty}^{\infty} T_t(k_x,k_y)e^{j\gamma z}e^{jk_x x}e^{jk_y y}dk_x dk_y \tag{4.5a}$$

$$T_t(k_x,k_y) = \frac{e^{-j\gamma z_o}}{2\pi}\int_{-\infty}^{\infty}\int_{-\infty}^{\infty} E_t(x,y,z_o)e^{-jk_x x}e^{-jk_y y}dxdy \tag{4.5b}$$

shows that the windowing of the plane wave processing algorithm performs the same spatial filtering of the plane wave spectrum that the near field to far field transformation accomplishes by converting to the spectral domain, changing z coordinate position and transformation back to the field domain.

Effects of the erroneous data files were minimized in the plane wave processing algorithm by setting the data of those files to zero and decreasing the number of contributing sample positions appropriately. Setting measurement data to zero in this algorithm has a small affect on the averaging outcome because the summation is not dependent upon the relative positions of the sample locations.

4.7 Calibration

Plane wave processing was performed on test target, reference target, and background measurement sets, resulting in a far field frequency sweep scattering estimate for each measurement set. A vector background subtraction and calibration against a known theoretical reference target were then performed. This calibration

is described by the following equation.

$$C_t = \left[\frac{S_t - S_{bt}}{S_r - S_{br}}\right]^2 E_r \tag{4.6}$$

where

C_t = Calibrated Far Field Bistatic RCS of Target (area)

S_t = Meas. Bistatic Scattering of Target (Volts)

S_{bt} = Meas. Bistatic Scattering of Target Background (Volts)

S_r = Meas. Bistatic Scattering of Reference (Volts)

S_{br} = Meas. Bistatic Scattering of Reference Background (Volts)

E_r = Exact Far Field Bistatic RCS of Ref. Target (area)

All quantities in equation (4.6) are complex. It should be noted that E_r is a function of the bistatic angle, the incident polarization, and their relationship to each other.

Chapter 5

Experimental Measurements

Experimental measurements of targets with known bistatic responses were made at two bistatic angles, 65 and 109 degrees to evaluate the scanner system performance. The targets measured were an 18 inch diameter sphere, a 6 inch diameter sphere, and a 6 cm tall right circular cylinder with a 4 cm diameter. Duplicate processing using the two taper functions (14,90) and (40,120) (discussed in Section 4.2), was investigated. The backprojection algorithm was used to obtain beam aiming information and the results of two aim implementations were compared. The spatial filtering function of the plane wave processing procedure was verified in the removal of a direct reflected signal from the rolled edge of the compact range parabolic reflector.

5.1 Measurement Procedure

The majority of the measured data was obtained in two sessions, 16 hours long separated by 8 hours. The first session measured scattering at the acute 65 degree bistatic angle, the second, at the obtuse 109 degree bistatic angle. The target measurement sequence listed below was identical for each session.

1. 18 inch diameter sphere with absorber cover on support pedestal.

2. 6 inch diameter sphere with absorber cover on support pedestal.

3. Absorber cover on support pedestal (background measurement).

4. Cylinder with absorber cover on support pedestal.

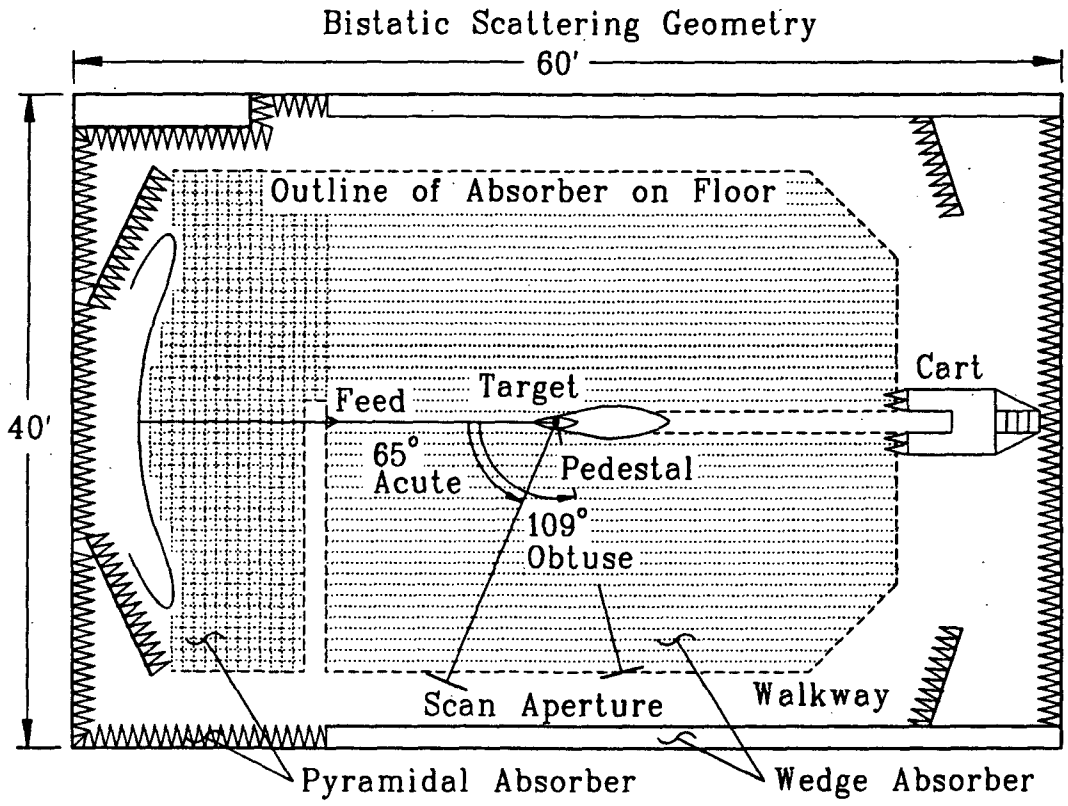

Figure 5.1: Geometry of the OSU-ESL compact range and scanner structure.

The geometry of the measurement process is shown in Figure 5.1. The parabolic reflector produced the incident plane wave signal which was scattered by the target and received by the scanner at the bistatic angle. The scan plane was positioned by eye sighting to be perpendicular to the direction of arrival of the bistatically scattered signals from the target.

Once properly positioned and aligned with the horizontal, the scanner bistatic angle was determined by placing a flat plate on the target pedestal, aligning it 90 degrees off broadside with respect to the parabolic reflector, and then rotating the plate until a maxima was observed with the probe antenna located in the center of the scan aperture. The bistatic angle could then be computed. At this point, the hardware range gating delays were set. A transmit pulse width of approximately 30

nsec and a receive range gate width of approximately 10 nsec centered on the target were used.

In all measurements, vertical transmit and receive antenna polarizations were used. The instrumentation computer controlled the operation of the pulsed CW radar system and the stepper motor power supplies. The speed of the horizontal motors was slowed by a 7 msec delay between steps to increase the torque produced.

During data acquisition, software looping structures allowed for realization of the aperture width and sample spacing parameters and automated data acquisition for an entire two dimensional scan. Each target was scanned over a 30 inch square aperture using a 1 inch sample spacing. The initial position of the probe antenna (the "zero" position) was set at 0.1 inches off both the horizontal and vertical Unislide limit switches. At each sample position a frequency sweep was performed which measured the amplitude and phase of the bistatically scattered signal relative to the transmitted signal for frequency values of 2 to 18 GHz at 20 MHz steps. Each measured value recorded was the average of sixteen samples of the scattered signal. Upon completion of a frequency sweep, the data was sent to the VAX 8550, stored for later processing, and the probe antenna moved to the next sample location. The group of frequency sweep files associated with a single two-dimensional scan of a target is referred to as that target's "measurement file set".

After all measurements were completed, each target's measurement file set was plane wave processed using the algorithm discussed in Chapter 4, resulting in a far field frequency sweep or "far field file" associated with each target measurement file set. These far field files were stored for use in the calibration process.

All calibrated results presented are the result of plane wave processing of the test target data, reference target data, and background data measurement file sets. It is possible to reverse the order of plane wave processing and calibration, however performing calibration first requires more data storage space. For our 30 inch square aperture and 1 inch sample spacing, calibrating first would produce 961 calibrated

files, one for each sample location, whereas only 4 files would be generated by first plane wave processing the target, reference and associated background uncalibrated measurement file sets. Since the calibration process uses the theoretical far field target response, the measured files in the calibration should also be far field quantities. Our tests produced similar results for either order of calibration and plane wave processing, therefore to save computer data storage space, which was at a premium, the calibration was performed after plane wave processing.

5.2 Spatial Filtering Verification

The planar scanner was designed to perform bistatic measurements in a compact range environment. Most compact range designs minimize the effect of undesired spurious signals in the target zone, and the effect of structures which cause a strong monostatic scattering response. Examples of these designs are the rolled edge of a parabolic reflector and the ogival cross–sectioned target support structure. The rolled edge on a compact range reflector reflects the fields incident upon the edge of the reflector away from the target zone and out to the sides of the measurement chamber. This is desirable for monostatic measurements since it helps create good plane wave performance in the target zone, but for bistatic measurements it has the undesired side effect of reflecting energy directly towards the bistatically positioned receiver. The ogival target support structure in the OSU-ESL compact range was designed and aligned for a very small monostatic scattering return. However at certain bistatic angles the shape of the ogive sides can cause large bistatic scattering. The data processing discussed in Chapter 4 included two features which can eliminate some of these types of unwanted signals.

The first algorithm was background subtraction, implemented as part of the calibration procedure. Ideally, background subtraction would eliminate signals which are caused by structures which are immobile during both target and associated background measurements and which are not due to target interactions. Therefore,

background subtraction of the measurement data should remove the bistatic scattering terms of the ogival support column, but not interactions between the target and support column. The second algorithm, plane wave processing, spatially filters the measured data, ideally suppressing signals which are incident upon the scanner from outside the target zone plane wave region of the scan-aperture synthetic-array pattern.

Figure 5.2 shows the signal paths that were observed in time domain plots for the acute and obtuse bistatic angles. Also shown are two pulse timing diagrams which indicate (by the arrows) the time of arrival of each signal at the scan aperture and the 30 nsec extent of each signal pulse. The position of the 10 nsec wide receive gate was unable to be exactly calculated, but the position shown in both cases agrees with the time of arrival and the amplitude of signals observed in the time domain plots. The positioning of the hardware receive gate can remove some undesired signals as can be seen in the acute case where the signals which emanate directly from the feed without reflecting off the parabolic reflector have been completely gated out. However in the obtuse case, both the direct illumination of the scan plane by the feed backlobe and the scattering of the feed backlobe off the target were received by the hardware range gate window. A feed antenna for the parabolic reflector with better than the -20 dB backlobes of the AEL horn antenna used in this research would reduce these undesired signals.

Figure 5.3 shows the impulse response of an 18 inch diameter sphere including the background, and the impulse response of the background without the sphere. These were created from measurements taken at a single scan position for the 109 degree bistatic angle. The large response at +8 nsec in the 18 inch diameter sphere impulse response plot indicates the presence of the sphere. The impulse response terms are labeled according to the paths described in Figure 5.2. The term which appears in the target measurement at +15 nsec but not in the background measurement has not been positively identified, but is most certainly a target interaction since both

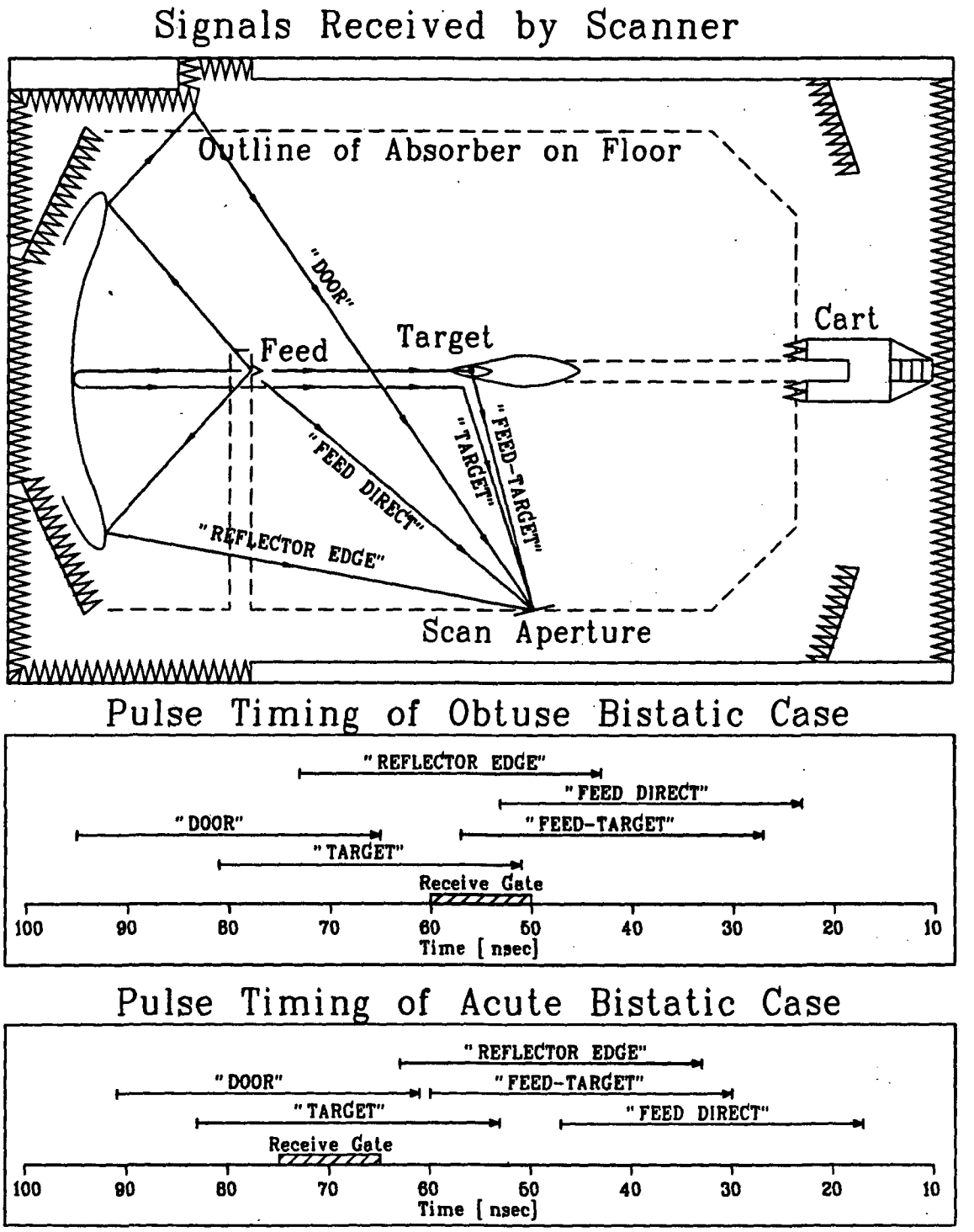

Figure 5.2: Signal bounce path diagram and timing diagrams for the acute and obtuse bistatic angles.

background subtraction and plane wave processing do not remove it, as shown in Figure 5.4.

Figure 5.4 shows the results of background subtraction on the data of Figure 5.3 and plane wave processing on the 18 inch diameter sphere measurement file set. The plot labeled "plane wave processed 18 inch diameter sphere" was created by plane wave processing the 18 inch diameter sphere measurement file set (including background interactions). Thus, the entire scan aperture data was utilized but not background subtracted.

The sphere term is retained by both background subtraction and plane wave processing algorithms as expected. Both the reflector edge reflection term and the feed backlobe are independently removed by both algorithms since they are not caused by the target and their incidence angles are outside of the target zone plane wave region. From analysis of the magnitude of the reflector edge term in the time domain plots, it was calculated that the background subtraction algorithm reduced the magnitude of the reflector edge signal by at least 29 dB and the plane wave processing reduced it by at least 35 dB. The term due to the scattering by the target from the feed backlobe however can not be removed by either algorithm. The background subtraction cannot remove it because it is directly caused by the presence of the target, and the plane wave processing cannot remove it because it has the same incidence angle as the desired bistatic scattering response term. In future research, the hardware range gate should be positioned such that this term is not received. This was the case for the acute bistatic angle, as was detailed in Figure 5.2.

Figure 5.5 shows the impulse response of an 18 inch diameter sphere including the background, and the impulse response of the background without the sphere for the acute bistatic angle case. These were created from measurements taken at a single scan position. The large response at 20 nsec in the 18 inch diameter sphere impulse response plot indicates the presence of the sphere. The impulse response

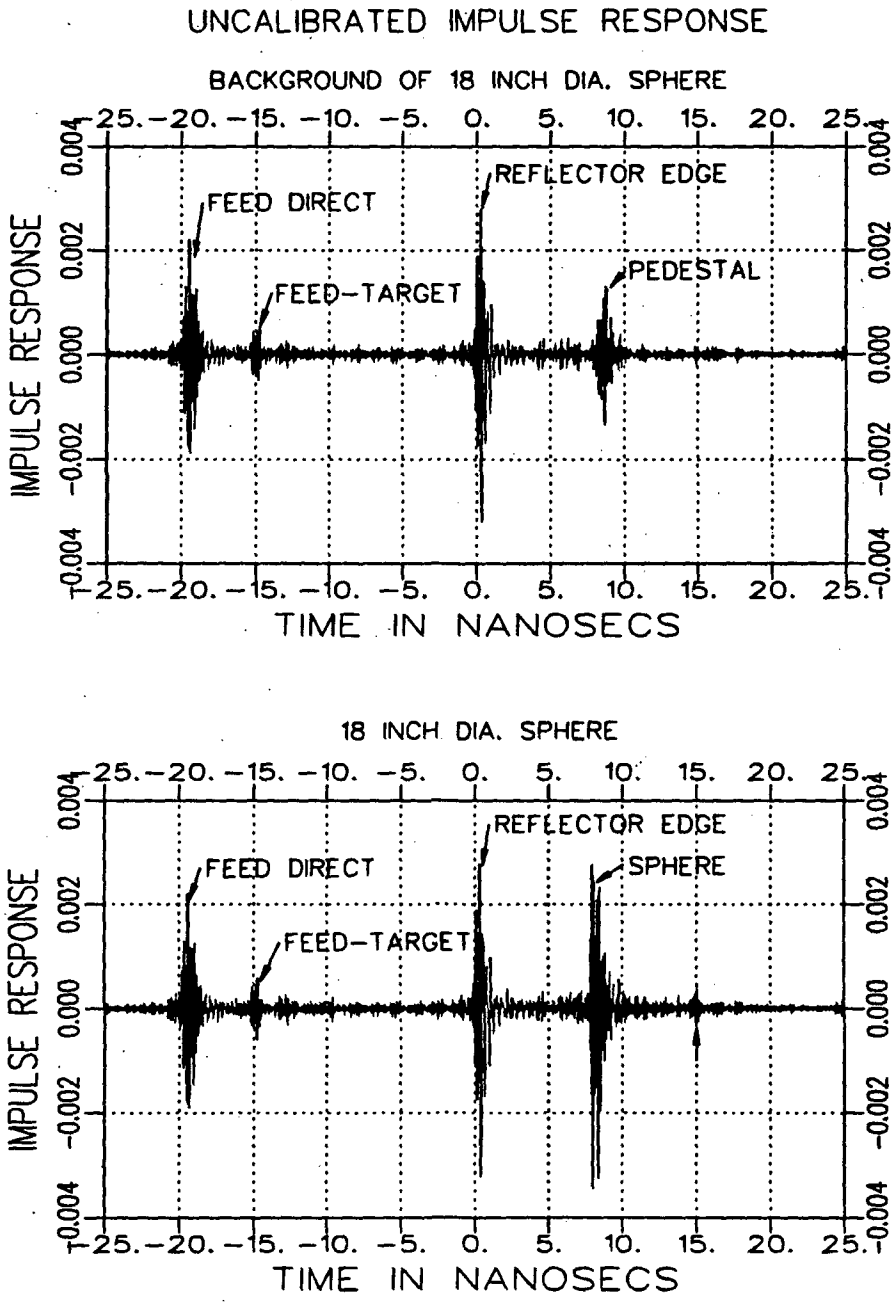

Figure 5.3: Uncalibrated 109 degree bistatic impulse response of an 18 inch diameter sphere plus background, and background alone. Single scan position measurements.

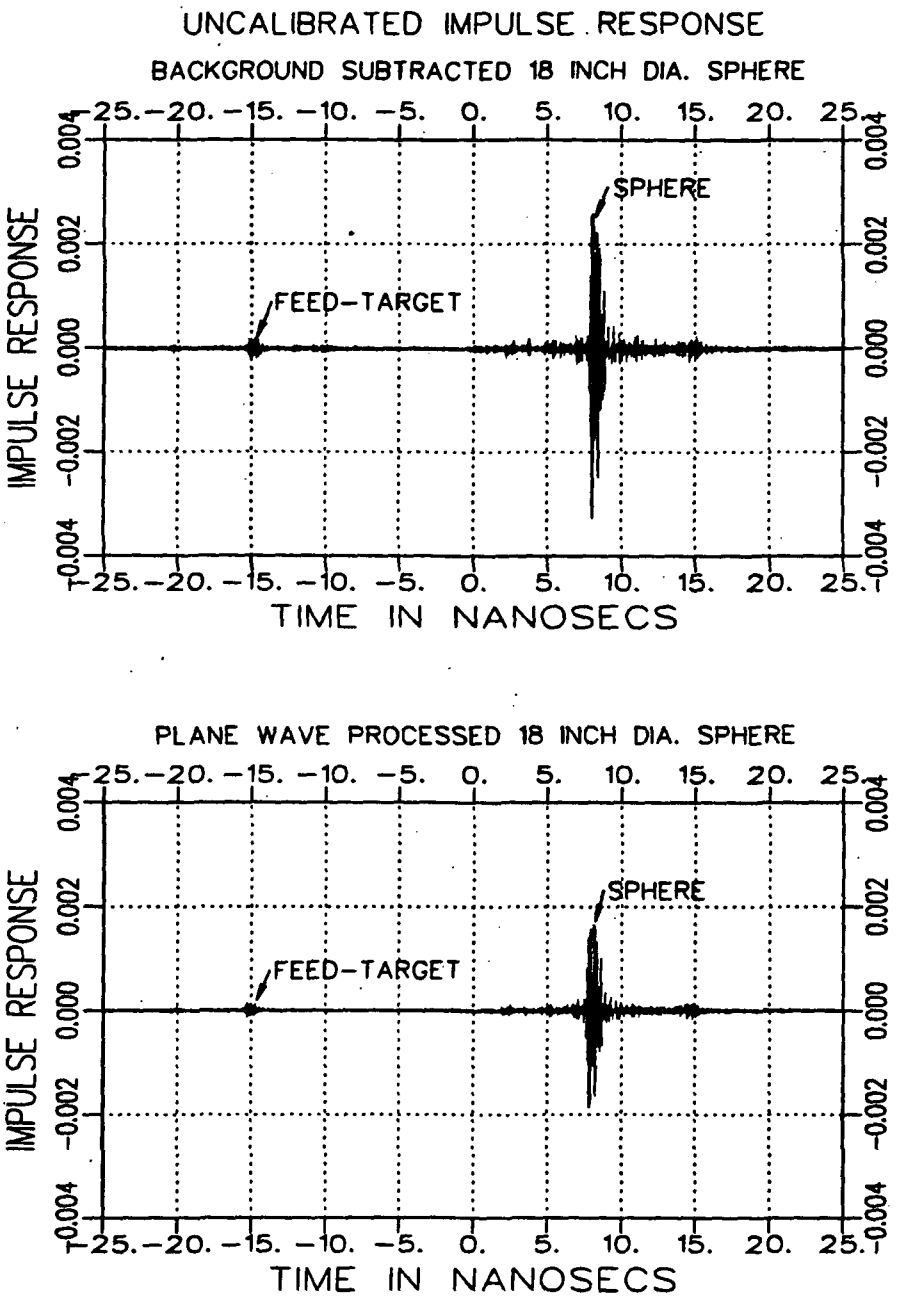

Figure 5.4: Uncalibrated 109 degree bistatic impulse response of single scan position background subtracted 18 inch diameter sphere, and plane wave processed 18 inch diameter sphere plus background. (40,120) Taper.

term labeled "DOOR" actually corresponds to two terms; the "DOOR" bounce path shown in Figure 5.2 and the unidentified target interaction term discussed in the obtuse case, approximately 7 nsec after the sphere response.

Figure 5.6 shows the results of background subtraction on the data of Figure 5.5 and plane wave processing on the 18 inch diameter sphere measurement file set. The plot labeled "plane wave processed 18 inch diameter sphere" was created by plane wave processing the measurement file set of the 18 inch diameter sphere including background interactions. As expected the sphere term is retained by both algorithms and the term labeled "DOOR" has been decreased in magnitude. This decrease is due to the removal of the "DOOR" path bounce part but not the target interaction part.

5.3 Data Presentation Format

Figures 5.7 and 5.8 show the impulse and frequency response of a 6 inch diameter sphere, calibrated against an 18 inch diameter sphere for the acute and obtuse bistatic angles, respectively. Note the terms which appear near -21 in Figure 5.7 and -24 nsec in Figure 5.8. These terms can be identified as interactions between the target and room since neither background subtraction nor plane wave processing removed them. Yet, they are far enough removed in time from the expected response, that they can be removed without altering the bistatic RCS response due to the direct illumination and scattering from the target. The removal of these terms can be accomplished by a frequency smoothing process (a 7 point average was used in this case). Figure 5.9 shows the result of this frequency smoothing on the data of Figure 5.8, note that the term at -24 nsec in the impulse response and the extremely fast oscillations in the magnitude response have been removed. All obtuse bistatic angle results presented here utilize this 7 point frequency smoothing for more accurate measurement comparison. Results presented here for the acute bistatic angle case do not use the frequency smoothing process. Time domain plots

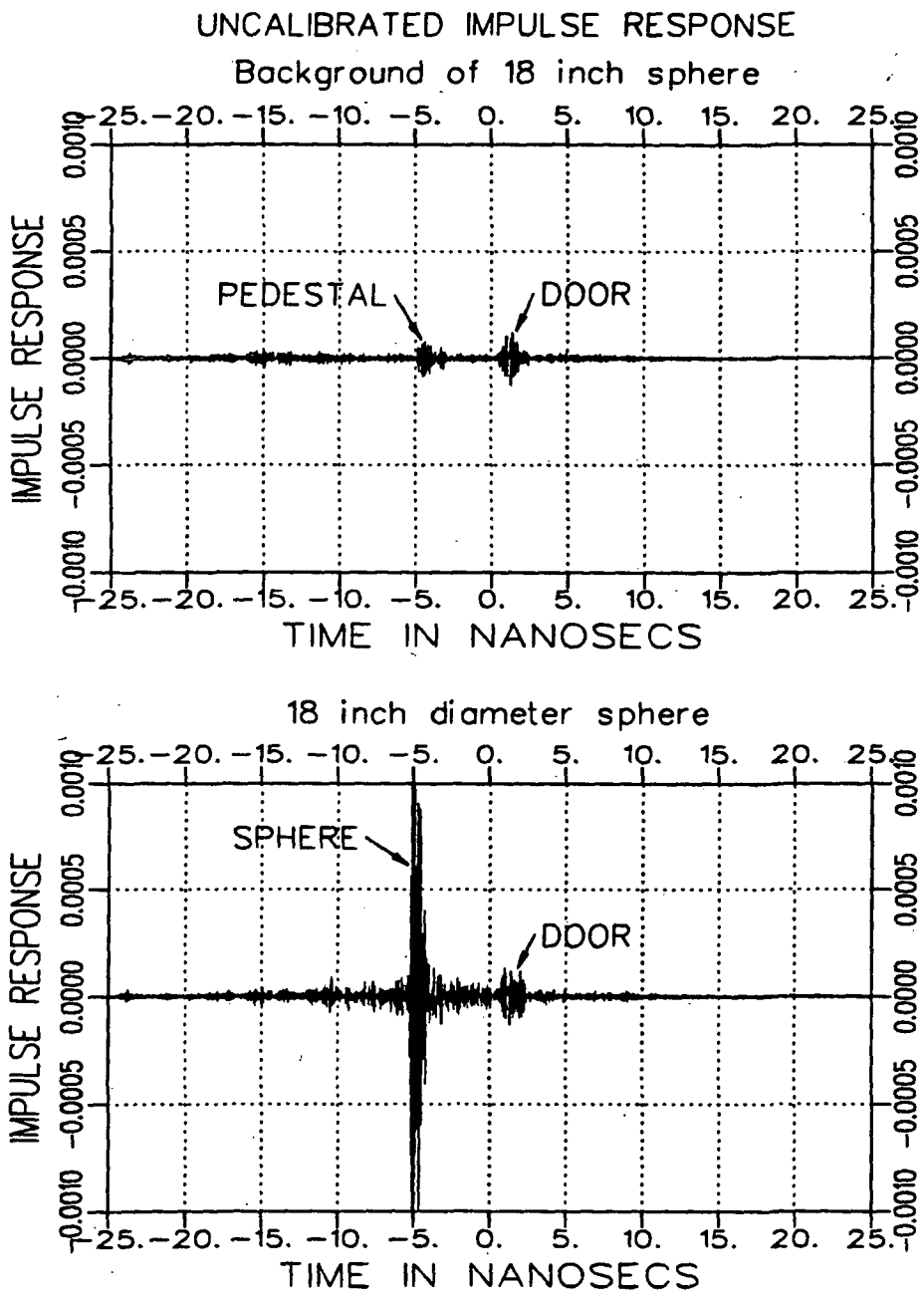

Figure 5.5: Uncalibrated 65 degree bistatic impulse response of an 18 inch diameter sphere plus background, and background alone. Single scan position measurements.

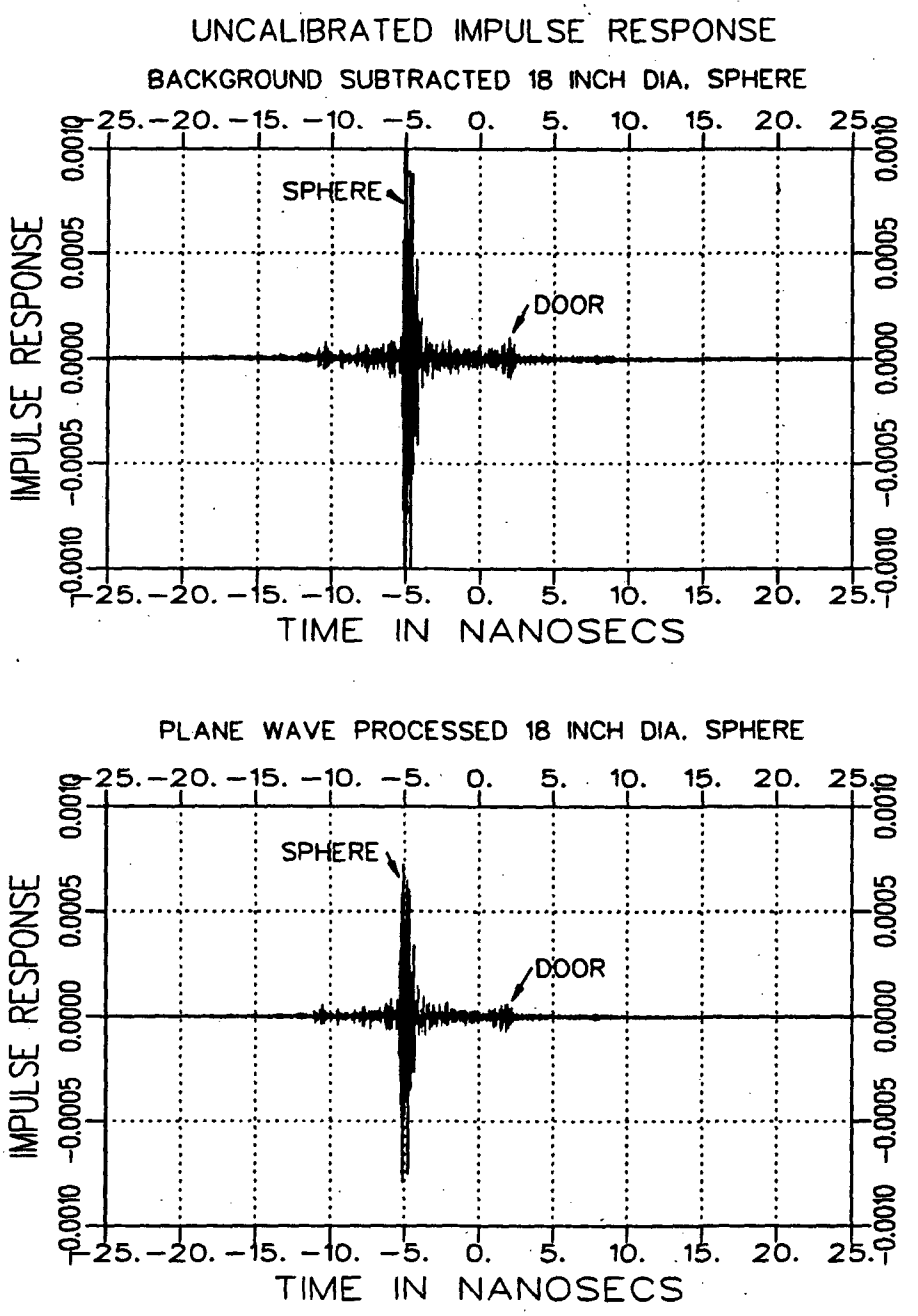

Figure 5.6: Uncalibrated 65 degree bistatic impulse response of single scan position background subtracted 18 inch diameter sphere, and plane wave processed 18 inch diameter sphere plus background. (40,120) Taper.

presented were produced by windowing the frequency domain with a Kaiser-Bessel taper function (alpha=2), and Inverse Fourier transforming the measurement data.

5.4 Aiming Comparison

Although not necessary for a scanning system with an adequate scan aperture size, the aiming process was necessary in our case to receive the specular scattering terms within the scan aperture window. Once the locations of the scattering centers were found by the backprojection algorithm, the beam of the scanner could be steered. A comparison was made between two aiming procedures. The calibration process requires four measured data sets; the target, the background associated with the target, the reference target, and the background associated with the reference target. The first aiming procedure was a compromise technique which aimed the beam of the scanner at a point midway between the locations of the target and reference target scattering centers and used that aim angle to plane wave process the target, reference, and background measurement data sets. For the acute bistatic angle, the compromise aim location chosen was $(x' = -2.5, y' = 7.75, z' = 210)$ in inches. The obtuse compromise aim location choice was $(x' = 7.0, y' = 6.5, z' = 180)$ in inches.

The second procedure was an independent aim technique in which the beam of the scanner was aimed directly at the scattering center of the target for plane wave processing of the target and associated background data sets, and then aimed at the scattering center of the reference target for plane wave processing of the reference and associated background. Tables 4.4 and 4.4 gave the scattering center locations for the specific targets and bistatic angles used in this work. After either aiming procedure, the far field files were used in the calibration process.

To compare the processing options of two bistatic angles, two aim procedures and two taper functions, a set of calibrated measurements where each member is created from 6 inch diameter sphere calibrated to the 18 inch diameter sphere but processed with different bistatic angles, aim procedures, and taper functions was

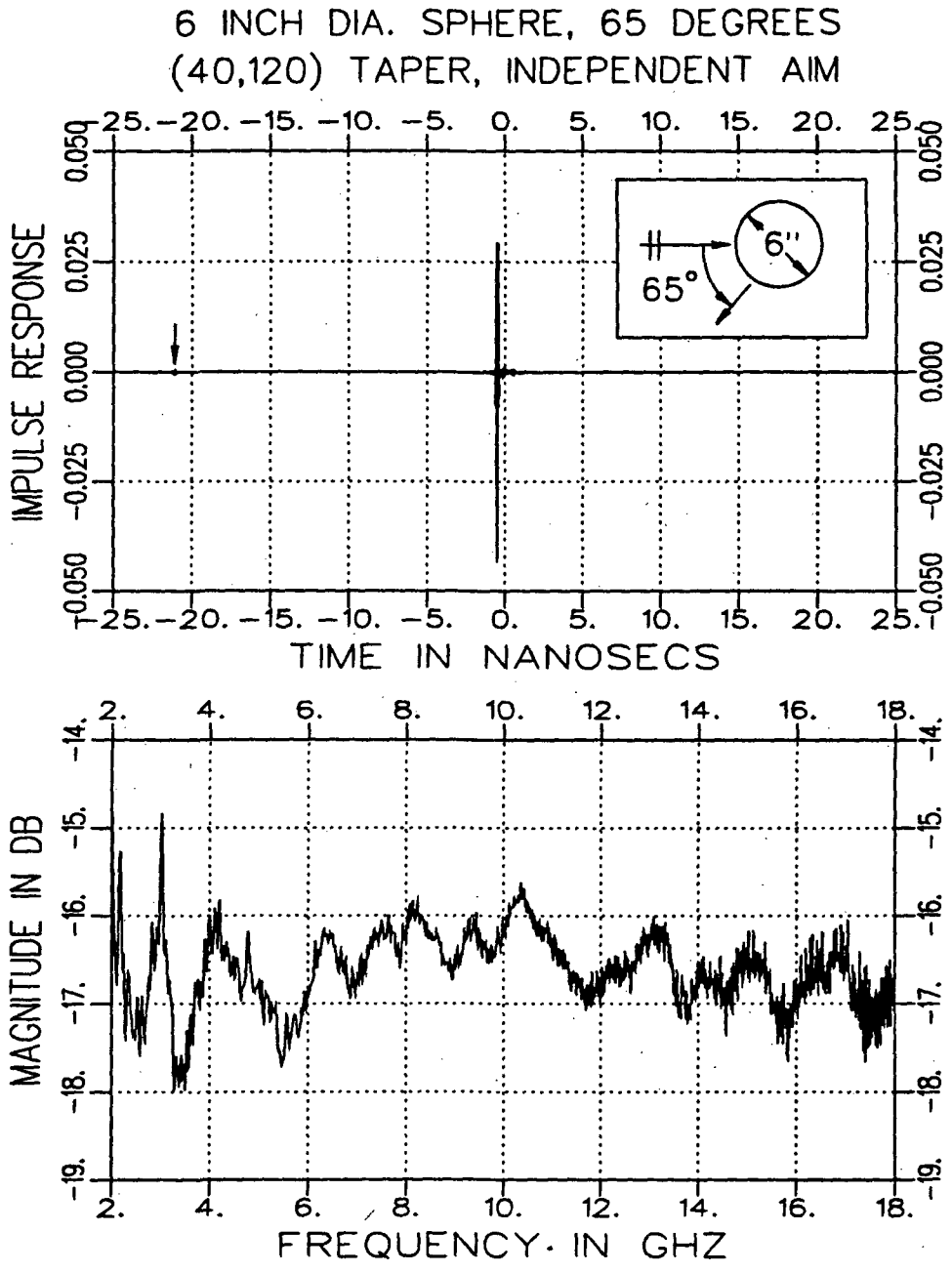

Figure 5.7: Calibrated, unsmoothed 65 degree bistatic RCS magnitude and impulse response of a 6 inch diameter sphere, (40,120) Taper, Independent Aim.

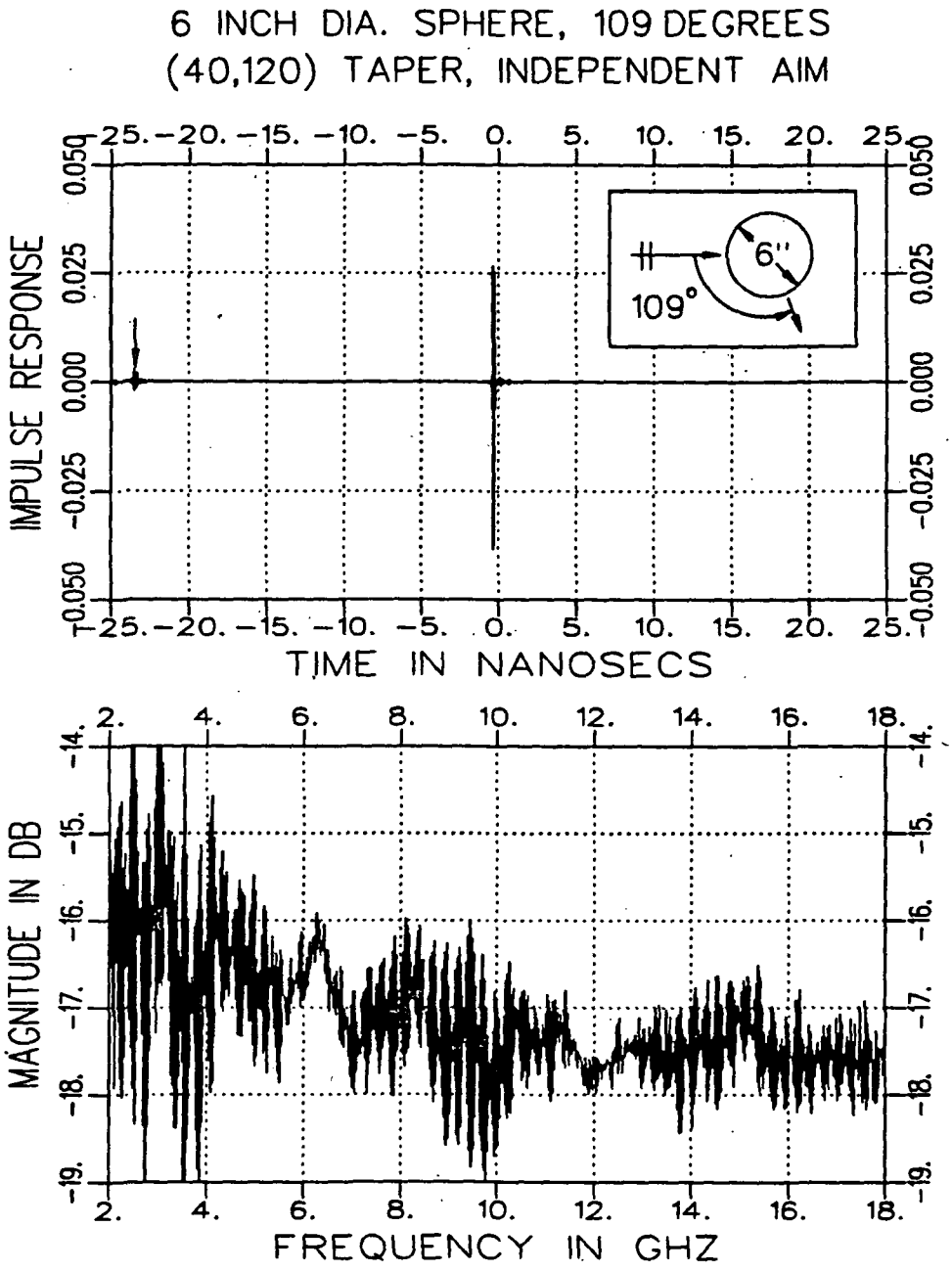

Figure 5.8: Calibrated, unsmoothed 109 degree bistatic RCS magnitude and impulse response of a 6 inch diameter sphere, (40,120) Taper, Independent Aim.

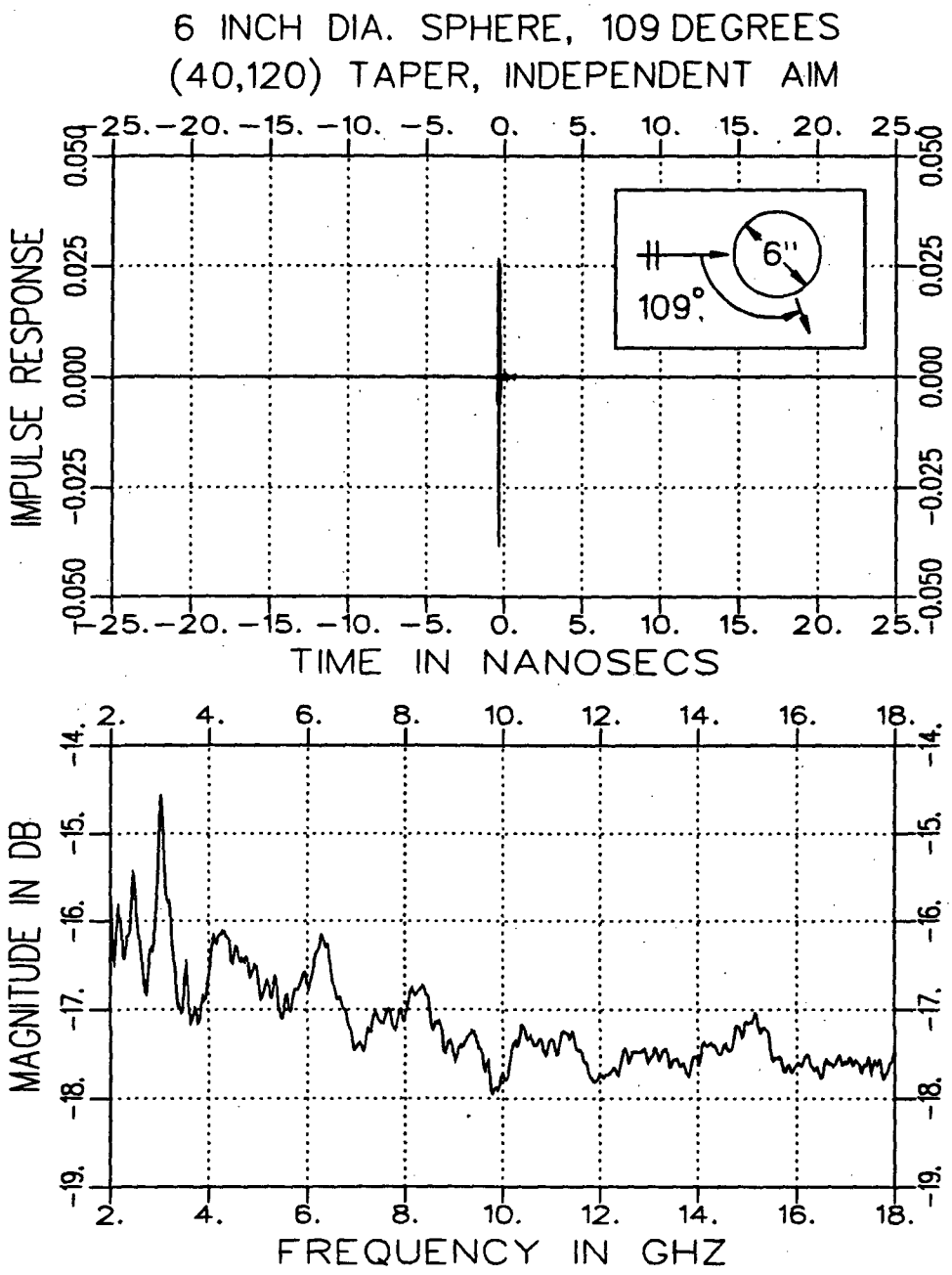

Figure 5.9: Calibrated, 7 point smoothed 109 degree bistatic RCS magnitude and impulse response of a 6 inch diameter sphere, (40,120) Taper, Independent Aim.

made. This set, shown below, can be organized to compare the performance of the aiming procedure or the taper functions for both bistatic angles.

Permutations of processing options.

Bistatic Angle	Aim procedure	Taper
Acute	Comp	(14,90)
Acute	Comp	(40,120)
Acute	Indv	(14,90)
Acute	Indv	(40,120)
Obtuse	Comp	(14,90)
Obtuse	Comp	(40,120)
Obtuse	Indv	(14,90)
Obtuse	Indv	(40,120)

Figure 5.10 compares the calibrated 109 degree bistatic RCS response of the 6 inch diameter sphere on an ogival support pedestal for the two aiming procedures described above. The theoretical 109 degree bistatic RCS magnitude response of a 6 inch diameter sphere is shown for comparison. These curves were chosen as a worst case comparison where the difference between the compromise and individual aim procedures was maximum. It shows that the individual aim process performed better for the obtuse bistatic angle, (14,90) taper case. Figure 5.11 shows the comparison of the two aiming procedures for the 65 degree, (14,90) taper case, with good agreement between the two aiming procedures. The two other possible comparisons from the processing options, [109°,(40,120)] and [65°,(40,120)] also showed good agreement between the two aiming procedures. From these figures it is seen that the independent aim procedure is preferred over the compromise aim procedure.

In all measurements of the 6 inch diameter sphere calibrated to the 18 inch diameter sphere, the oscillatory nature of the measured responses have the same oscillatory period (along the frequency axis) as the oscillations of the theoretical response. This indicates reception of the small creeping wave term for the vertical-

vertical antenna polarizations. However, there is an offset or bias to the measured data over the entire frequency range when compared to the theoretical response. In the acute bistatic case the magnitude of the measured response is offset from the theoretical response by approximately 1 dB and in the obtuse case, the measured response is offset 0.5 dB below the theoretical response. This may be due to bistatic scattering from the target support structure or target and pedestal interactions which are not included in the theoretical response curve.

5.5 Taper Function Comparison

Figure 5.12 shows the calibrated 109 degree bistatic RCS magnitude and impulse response of the 6 inch diameter sphere for the compromise aim procedure, and the (14,90) and (40,120) taper functions. It is interesting to note that for the compromise aim case, which was shown in the previous section to be less desirable than the independent aim, the (40,120) taper function comes closer to the theoretical response. The (40,120) taper function can compensate for the poor aim process performance since it's aperture efficiency is greater than the (14,90) taper function's aperture efficiency in the 3 to 12 GHz frequency range.

Figure 5.13 shows the 65 degree bistatic RCS response for a 6 inch diameter sphere calibrated to an 18 inch diameter sphere for the independent aim process. In this case the measured response of the two window functions match closely since the independent aiming process makes the plane wave region width (and the aperture efficiency) irrelevant for the size targets used in these measurements.

5.6 Bistatic Angle Comparison

Figures 5.14 and 5.15 show the best and worst processing procedure choices respectively for the 6 inch diameter sphere calibrated to the 18 inch diameter sphere with the theoretical magnitude response included for comparison at the acute bistatic

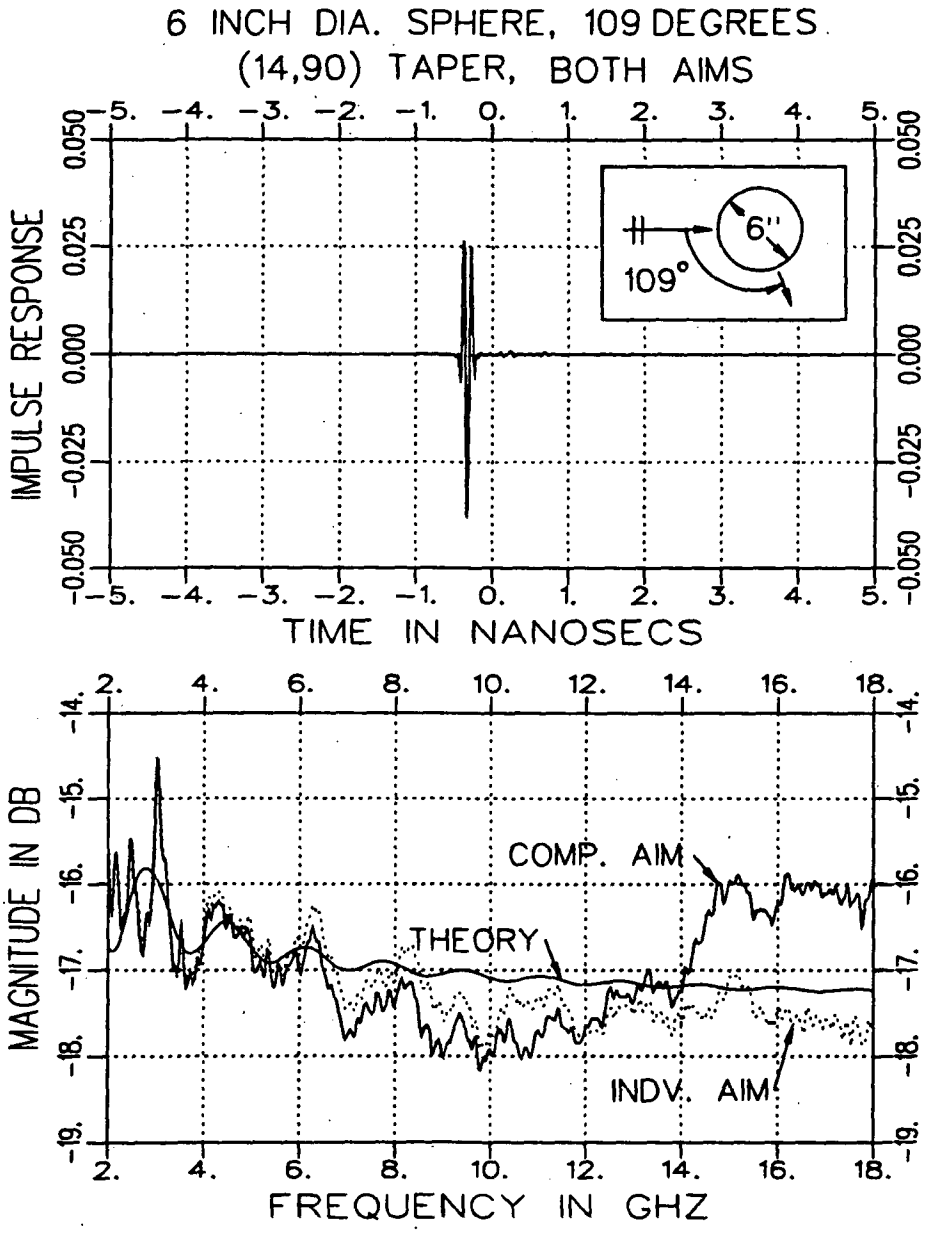

Figure 5.10: Calibrated 109 degree bistatic RCS magnitude and impulse response of a 6 inch diameter sphere for compromise and individual aim procedures with theoretical bistatic RCS magnitude overlay. 18 inch diameter sphere reference target, (14,90) Taper.

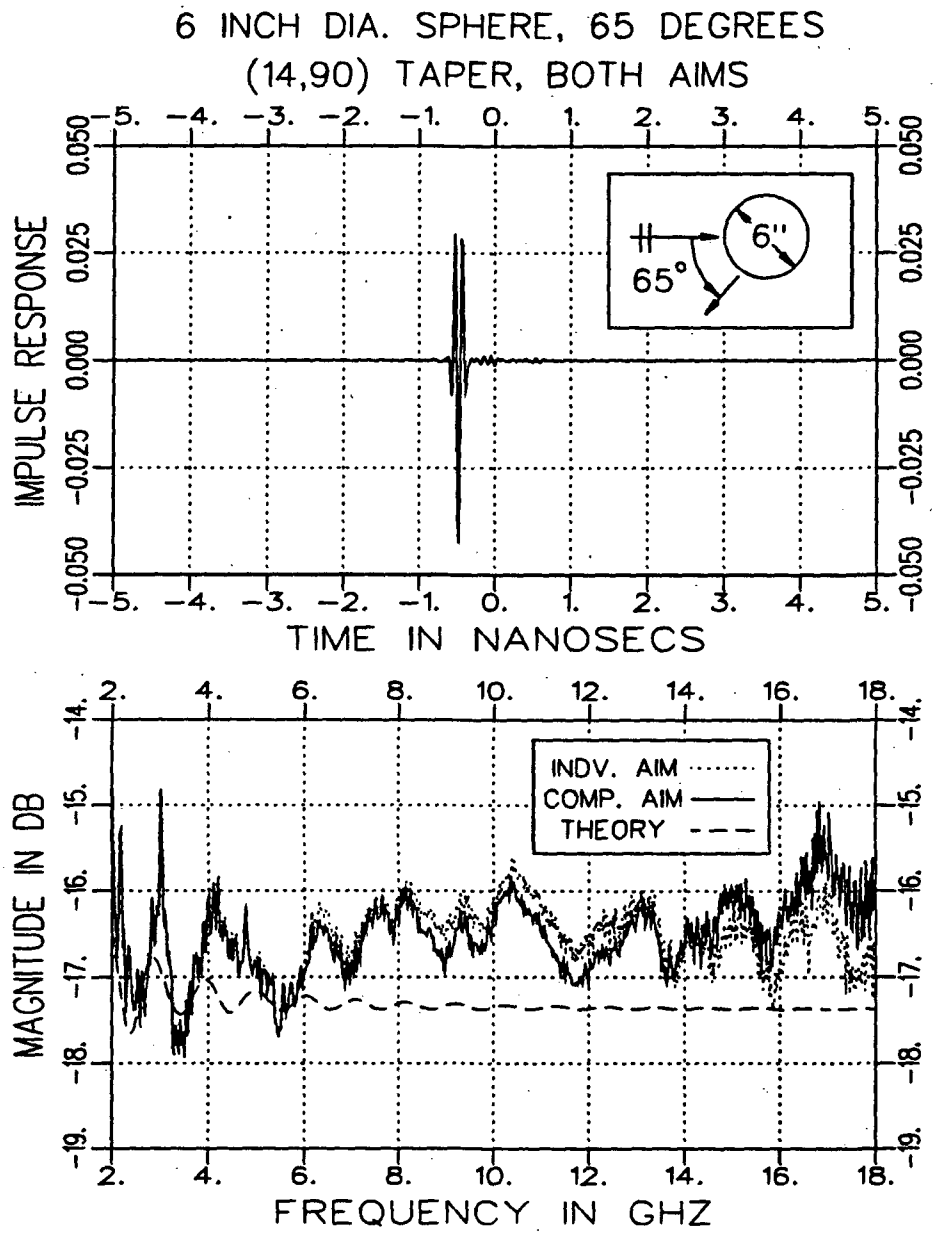

Figure 5.11: Calibrated 65 degree bistatic RCS magnitude and impulse response of a 6 inch diameter sphere for compromise and individual aim procedures with theoretical bistatic RCS magnitude overlay. 18 inch diameter sphere reference target, (14,90) Taper.

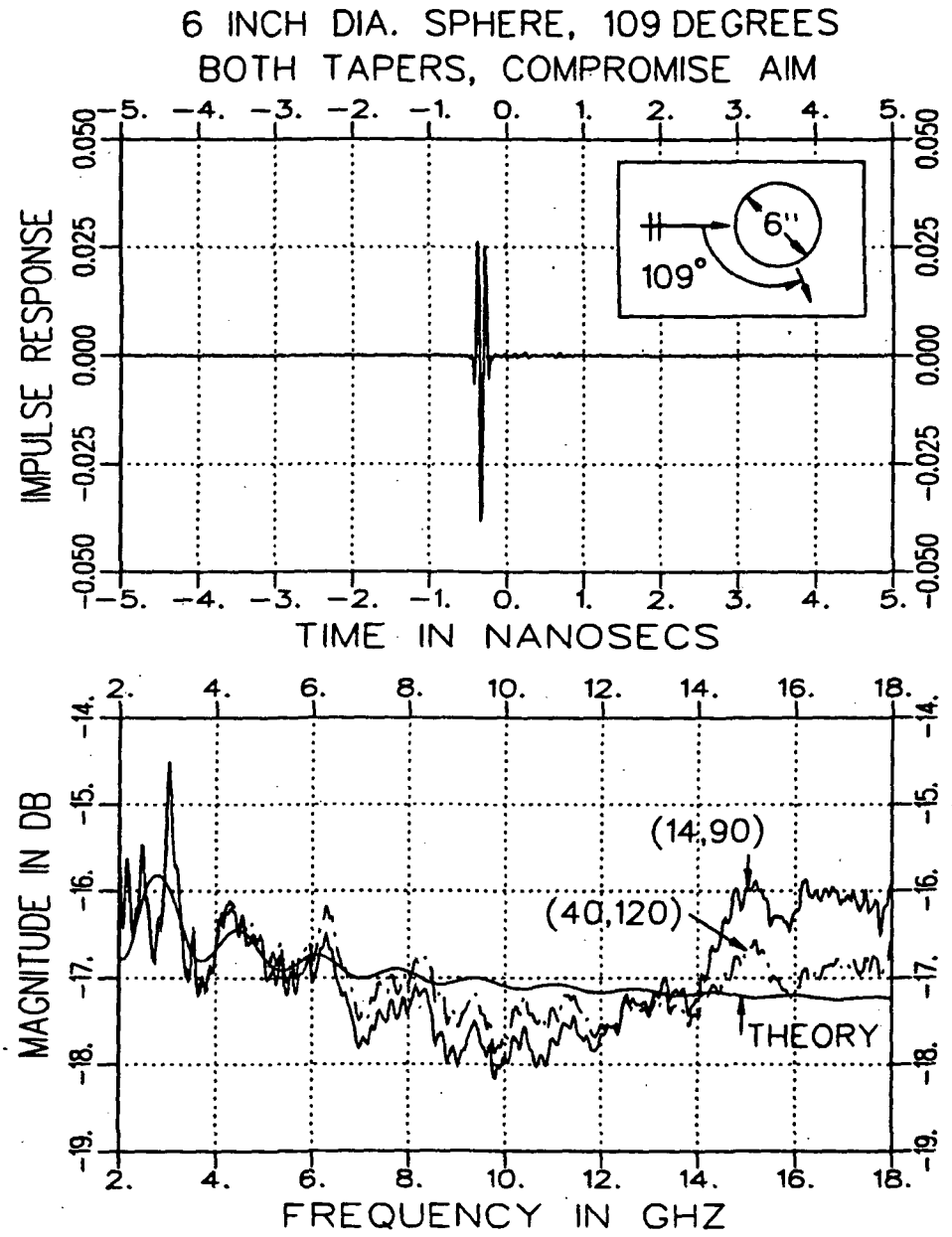

Figure 5.12: Calibrated 109 degree bistatic RCS magnitude and impulse response of a 6 inch diameter sphere for (14,90) and (40,12) taper functions with theoretical bistatic RCS magnitude overlay. 18 inch diameter sphere reference target, Compromise Aim.

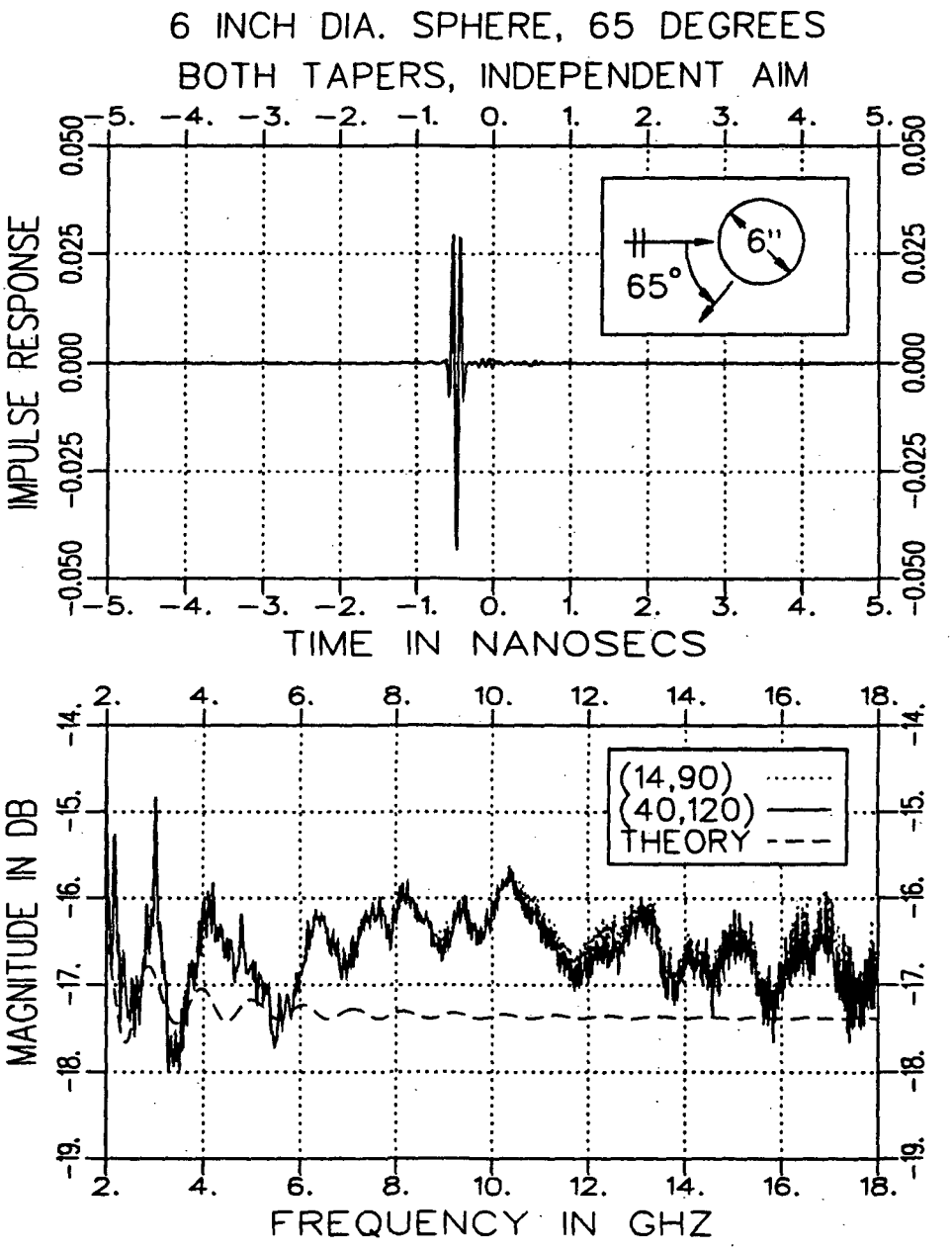

Figure 5.13: Calibrated 65 degree bistatic RCS magnitude and impulse response of a 6 inch diameter sphere for (14,90) and (40,120) taper functions with theoretical bistatic RCS magnitude overlay. 18 inch diameter sphere reference target, Independent Aim.

angle. The theoretical curve is not the expected result since it does not include the target and pedestal interaction terms, but if those terms are assumed small (not always the case) the theoretical curve does provide a means of comparison of the measured data to an idealized expected response. The best processing procedure for the acute bistatic angle was the (40,120) taper and independent aim. Note in Figure 5.14 that the oscillation period of the measured and theoretical responses are similar, and at the higher frequencies the measured result is closer to the theoretical response than for the worst case of Figure 5.15. Figures 5.16 and 5.17 show the best and worst processing procedure choices, respectively, for the obtuse bistatic angle case. There was no clear choice for the best taper function, but independent aiming performed much better than the compromise aiming.

A comparison can be made between Figures 5.14 and 5.16. Notice in the obtuse case that there is a 0.5 dB bias to the measured data, but that it is below the theoretical curve and is evident only above 9 GHz. The acute case has a 1 dB bias above the theoretical response over almost the entire frequency range. These characteristics were also evident in the calibrated measurements of the cylinder, to be discussed in the next section.

Referring to the impulse response of Figure 5.16, the large response at -0.5 nsec is the specular scattering term from the 6 inch diameter sphere. The small responses at approximately 0 and 0.5 nsec occur in the time frame where target and pedestal interactions as well as the small creeping wave term for this polarization are expected. It is impossible to distinguish these causes from each other by background subtraction or plane wave processing since they both are caused by the presence of the target and arrive at nearly the same incidence angles.

From these best–worst comparisons, and the aim and taper comparison sections, the choice of independent aim and the (40,120) taper function is evidently best for the small prototype scanner system. Once again it should be stated that the aiming procedure was only necessary to overcome the limitations of the small scan aperture.

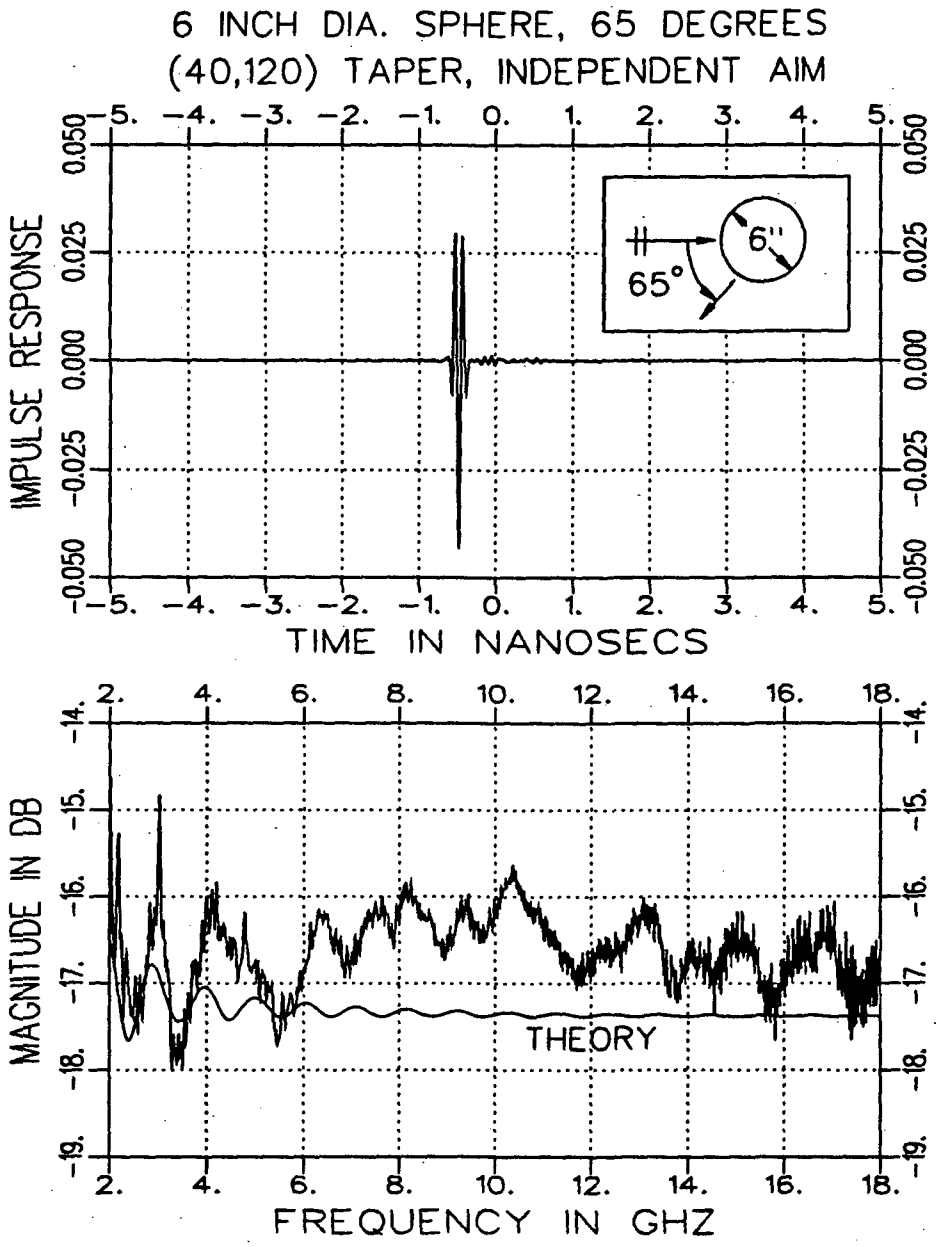

Figure 5.14: Best calibrated 65 degree bistatic RCS magnitude and impulse response of a 6 inch diameter sphere with theoretical bistatic RCS magnitude overlay. (40,120) Taper, Independent Aim, 18 inch diameter sphere reference target.

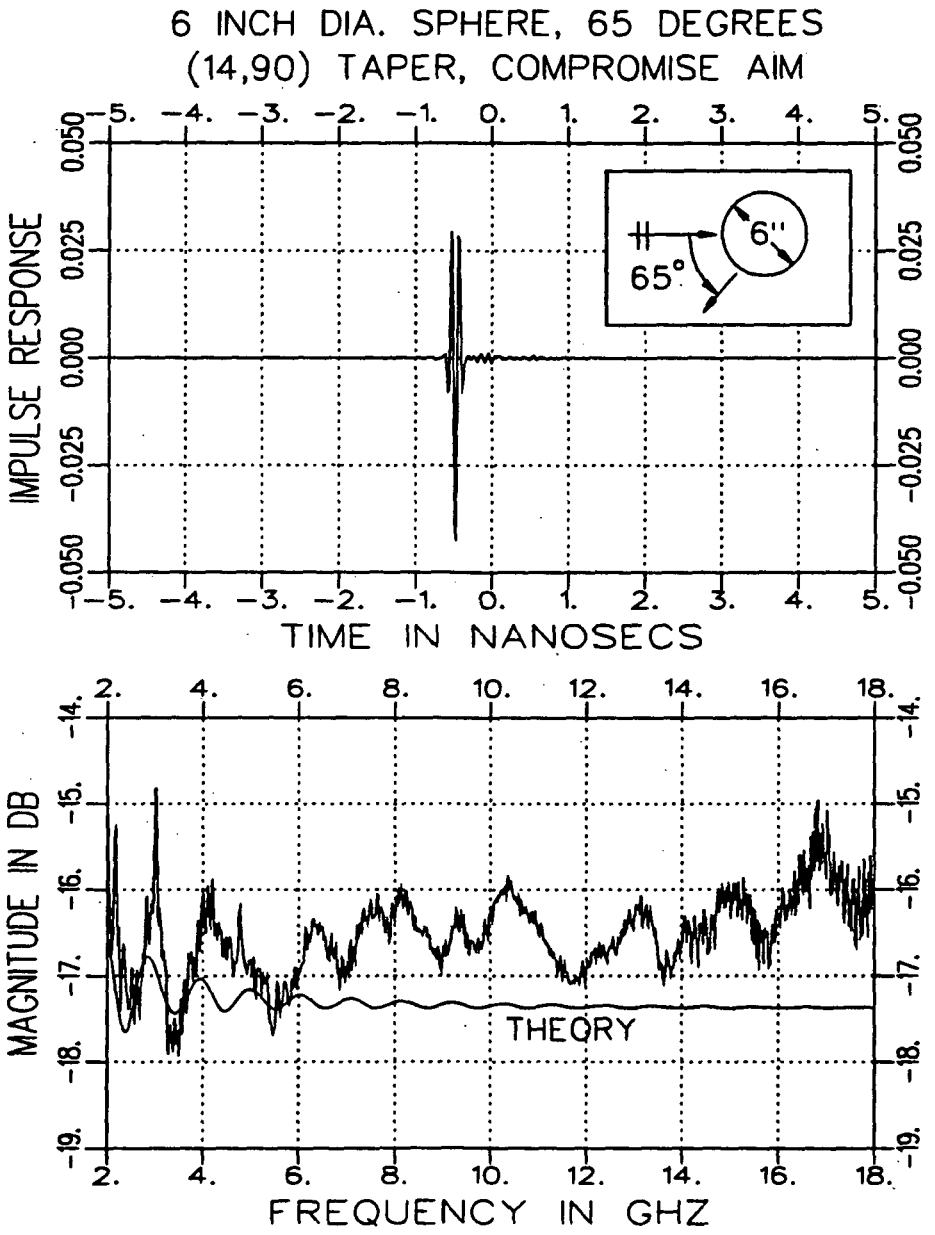

Figure 5.15: Worst calibrated 65 degree bistatic RCS magnitude and impulse response of a 6 inch diameter sphere with theoretical bistatic RCS magnitude overlay. (14,90) Taper, Compromise Aim, 18 inch diameter sphere reference target.

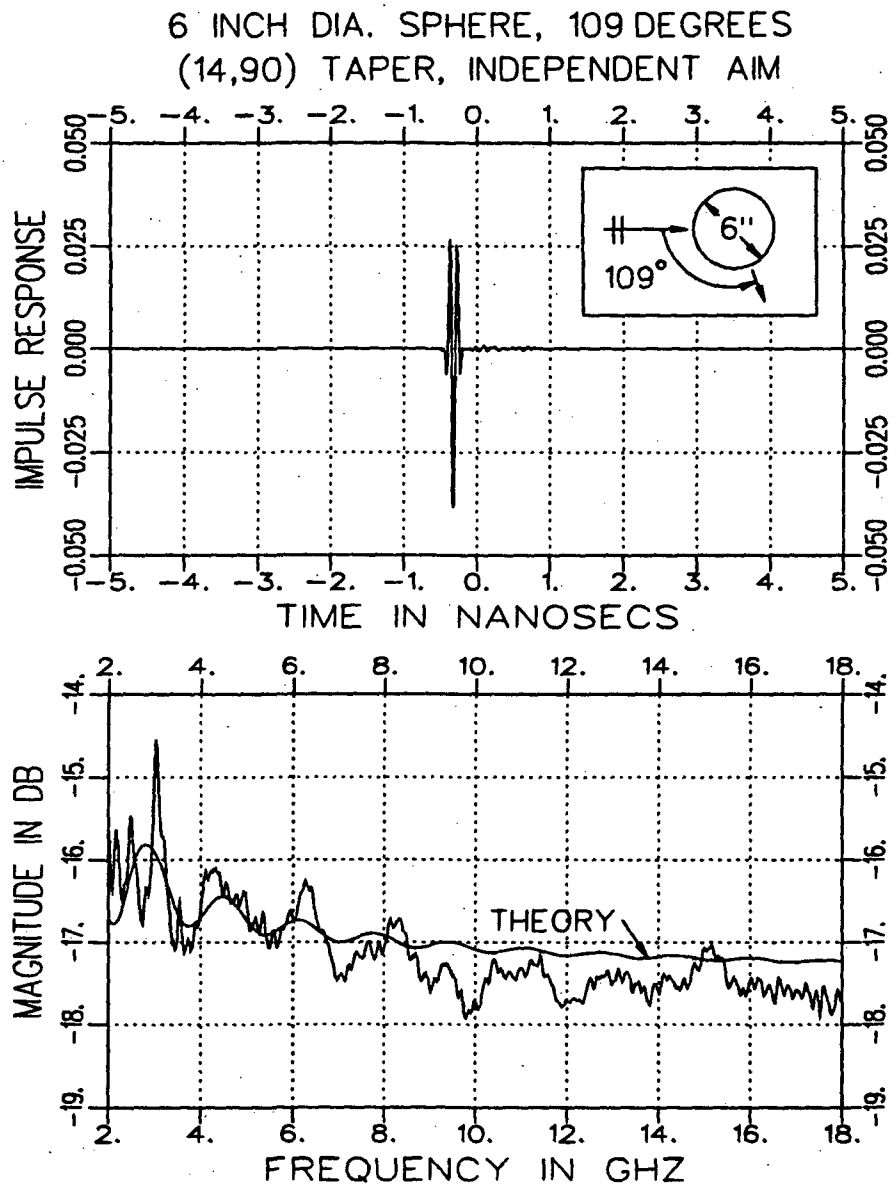

Figure 5.16: Best calibrated 109 degree bistatic RCS magnitude and impulse response of a 6 inch diameter sphere with theoretical bistatic RCS magnitude overlay. (14,90) Taper, Independent Aim, 18 inch diameter sphere reference target.

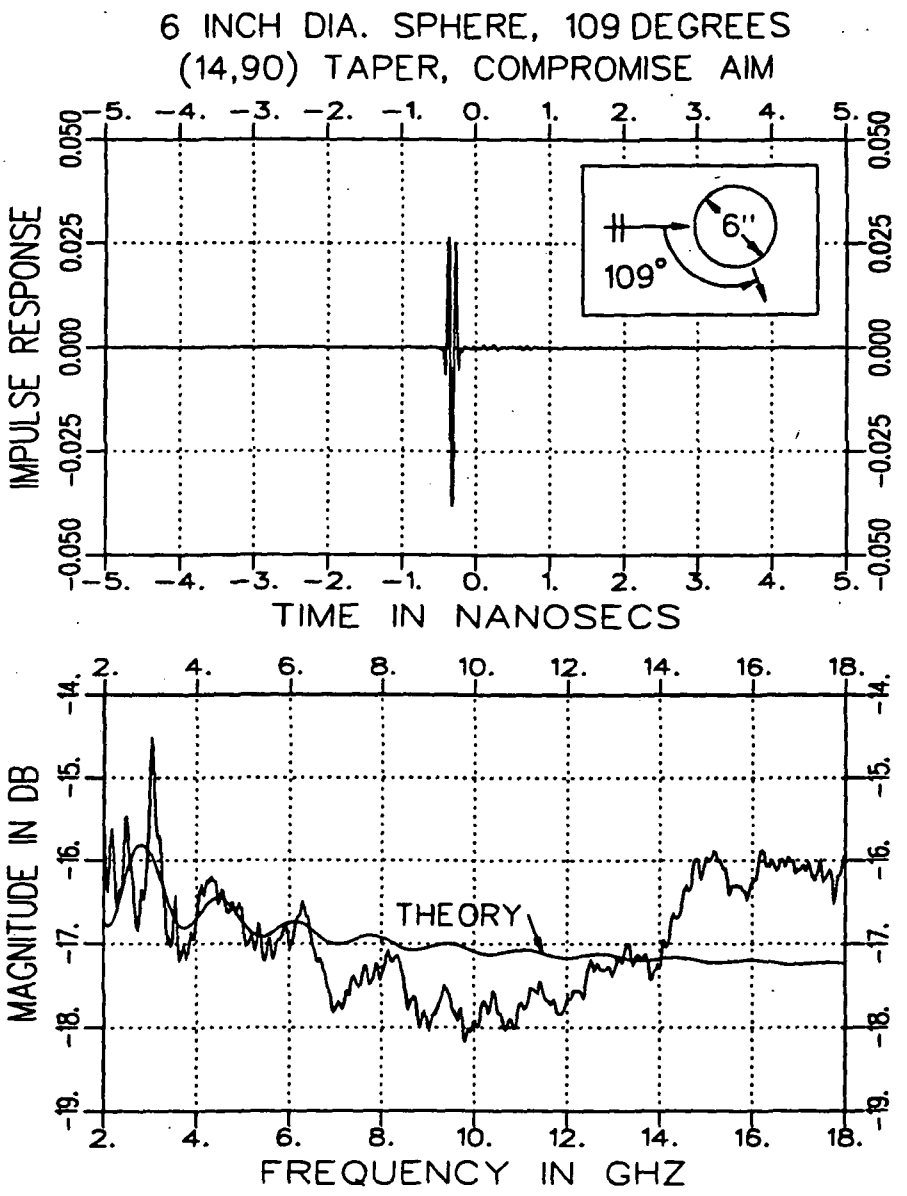

Figure 5.17: Worst calibrated 109 degree bistatic RCS magnitude and impulse response of a 6 inch diameter sphere with theoretical bistatic RCS magnitude overlay. (14,90) Taper, Compromise Aim, 18 inch diameter sphere reference target.

5.7 Different Reference Target Comparison

For the 6 inch diameter sphere, the only appropriate reference target choice was the 18 inch diameter sphere. However, the cylinder could be calibrated against either the 6 or 18 inch diameter spheres. Figure 5.18 shows the calibrated 65 degree bistatic RCS magnitude and impulse response of the 4 cm diameter by 6 cm tall cylinder calibrated against the 6 and 18 inch diameter sphere reference targets with the theoretical response curve for comparison. The (40,120) taper and independent aiming was used for accurate results.

The theoretical curve for the cylinder was obtained by analytically computing the bistatic echo width of an infinitely long circular cylinder and applying the common two-dimensional to three-dimensional RCS approximation:

$$RCS_{3-D} \approx \frac{2l^2}{\lambda} RCS_{2-D} \tag{5.1}$$

This approximation is only valid for frequencies where l, the length of the cylinder, is larger than one wavelength.

The cylinder response calibrated against either sphere follows the theoretical response to within about 2 dB, except for below 5 GHz, where the length of the cylinder, 6 cm, is less than one wavelength. It is interesting to note that the cylinder response calibrated against the 18 inch diameter sphere is offset by approximately 1 dB from the response of the cylinder calibrated against the 6 inch diameter sphere. This indicates that the offset in the 6 inch sphere data presented earlier which was calibrated against the 18 inch diameter sphere was probably due to using the 18 inch diameter sphere as the reference target. The best match of the cylinder calibrated response with the theoretical response is given by calibrating against the 6 inch diameter sphere.

Figure 5.19 shows the 109 degree bistatic RCS response of the cylinder calibrated against the 6 and 18 inch diameter spheres. The (40,120) taper function and independent aiming was used. As expected for the acute case and the offset of the 6

inch sphere when calibrated against the 18 inch diameter sphere, the two measured curves differ by approximately 0.5 dB, with the 6 inch reference curve being closer to the theoretical response.

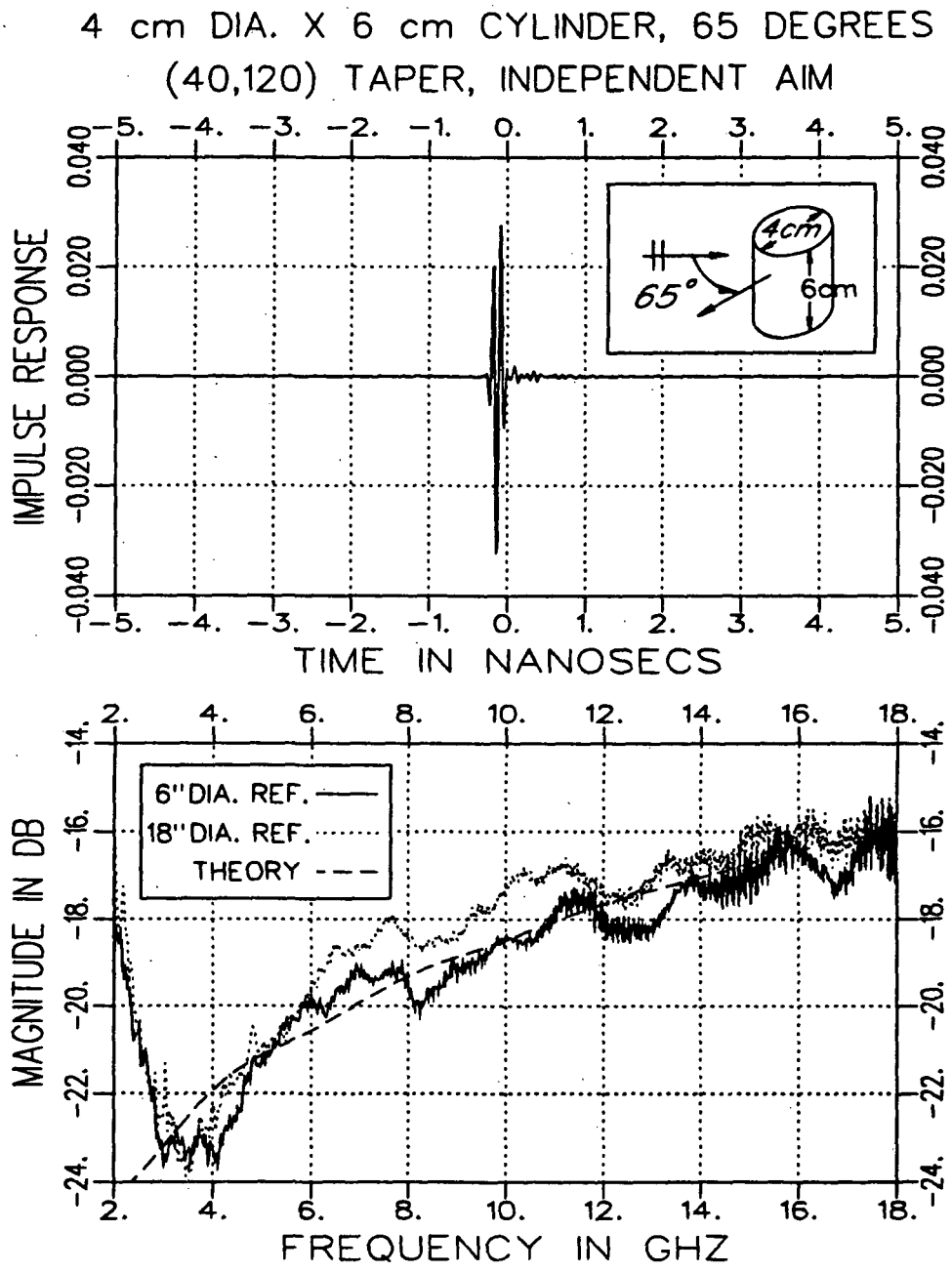

Figure 5.18: Calibrated 65 degree bistatic RCS magnitude and impulse response of a 6 cm tall, 4 cm diameter cylinder for 6 and 18 inch diameter reference targets with exact bistatic RCS magnitude overlay. Independent Aim, (40,120) Taper.

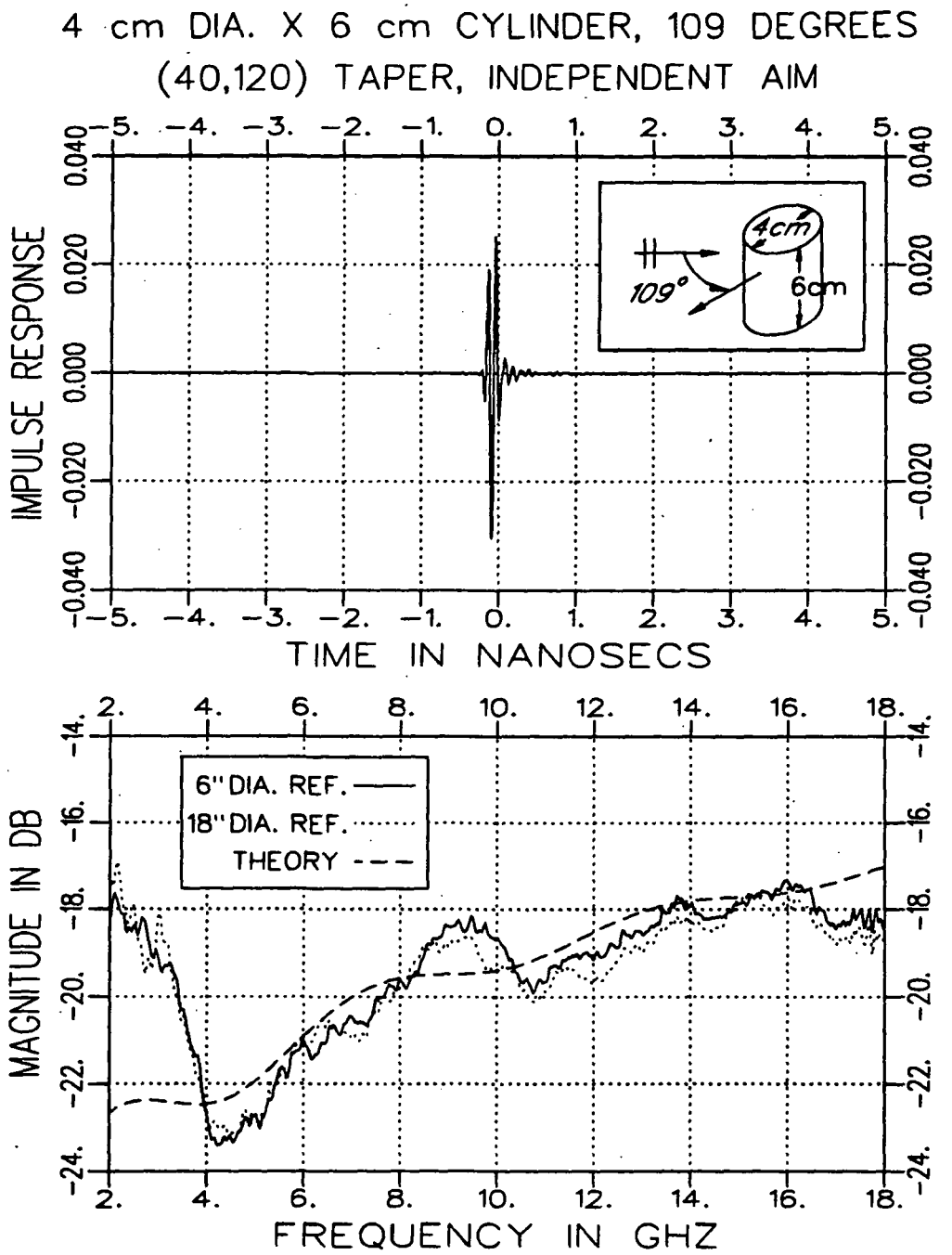

Figure 5.19: Calibrated 109 degree bistatic RCS magnitude and impulse response of a 6 cm tall, 4 cm diameter cylinder for 6 and 18 inch diameter reference targets with exact bistatic RCS magnitude overlay. Independent Aim, (40,120) Taper.

Chapter 6

Conclusions

The purpose of this project was to design, build, and test a planar near field scanning system for the measurement of bistatic RCS data in a compact range environment. Chapter 2 discussed some of the theory of planar near field scanning and its application to the measurement of bistatic RCS. Chapter 3 detailed the design and construction of the prototype planar scanner and analysis of its mechanical performance.

The planar scanner implementation is a low construction cost alternative to a second parabolic reflector for bistatic measurements. The basic idea behind the measurement and data processing system is that planar scanner probe measurements can be synthetically combined and digitally spatially windowed such that the scanner behaves as a receiving antenna array which selectively receives plane waves incident from the target zone. The spatial window in this work was based on the aperture distribution of a compact range parabolic reflector with rolled edges.

The bistatic RCS measurements made in the compact range chamber at The Ohio State University, ElectroScience Laboratory were successful in estimating the far field scattered signal of the test targets. The calibrated measured responses of all test targets were within 1 dB of the theoretical responses. The measurement and data processing systems which suppressed undesired signals, some of which were caused by the monostatic chamber design, were:

- HARDWARE RANGE GATING

  Hardware range gating was used to remove the direct illumination of the target by the feed horn backlobe.

- PLANE WAVE PROCESSING

  Plane wave processing was used to remove signals from angles outside the target zone. The scattered signal from the parabolic reflector edge, for example, was reduced by at least 35 dB.

- BACKGROUND SUBTRACTION

  The background subtraction algorithm removed signals which did not change between target and background measurement sets. For example, the reflection from the reflector edge was reduced by at least 29 dB by background subtraction alone.

- FREQUENCY SMOOTHING

  Frequency smoothing (time domain gating) was used to remove signals which were separated in time from the target signals.

Each of these four processes were used to reduce the effect of signals which were not due to the illumination of the target by the collimated beam of the reflector and received by the scan aperture.

Verification of system performance was accomplished through time domain analysis of the undesired signal reduction discussed above, and by comparing measured data with theoretical predictions of the test targets. The conclusions drawn from these comparisons include information about the interaction between target and target support pedestal since the theoretical predictions were for a test target floating in free space, and the actual measurements contained the response and interactions of the target support pedestal.

The primary limitation of this method of obtaining bistatic RCS measurements is the long scan time required, up to 3 hours for a full scan of our prototype 30

inch square aperture at 1 inch sample spacings. This may make the system cost inefficient in the long run due to data measurement time expenses. Bistatic RCS measurements as a function of bistatic angle would be impractical with this system. However, the theory applied here to a two dimensional aperture is directly applicable to measurement systems which require only one dimensional scanning.

As a final note, the aiming process used here to slightly adjust the location of the plane wave region is not necessary for all scanning systems since a larger scan aperture would produce a correspondingly larger plane wave region in the target zone, completely encompassing the test target. Given the necessity of the aim process for our prototype system which had a small scan aperture, the independent aiming process was shown to be preferred over the compromise aim. This is useful information even for larger aperture scanning systems since it allows a small change in the scanner beam direction without actual scanner repositioning and it can be done after the measurements are made.

Chapter 7

Two-Dimensional Backprojection

This appendix describes the application of a two-dimensional backprojection algorithm to the experimental data examined in Stephen Tuhela-Reuning's master's thesis. As discussed in Chapter 5, bistatically scattered fields from the test target were scanned over a square aperture, enabling a two-dimensional backprojection plot of the region near the target. The two-dimensional backprojection algorithm detailed in equation (7.1) is similar to the one-dimensional backprojection algorithm of Section 4.4 except that it involves a double summation over both the x and y directions. Two dimensional backprojection allows investigation of the location and strength of signals in the compact range, some of which can corrupt far field response estimates.

$$\tilde{S}_{m,n} = \frac{1}{N} \sum_{x} \sum_{y} \frac{R_{m,x,n,y}}{R_o} \tilde{E}_{x,y} \, e^{jkR_{m,x,n,y}} \tag{7.1}$$

where

$\tilde{S}_{m,n}$	=	Field estimate in focus plane
$\tilde{E}_{x,y}$	=	Measured field
R_o	=	Distance between focus and scan planes
$R_{m,x,n,y}$	=	Distance between focus and measurement positions

N = Total number of scan plane measurement positions

x = Scan plane horizontal position

y = Scan plane vertical position

m = Focus plane horizontal position

n = Focus plane vertical position

k = Free space propagation constant

Six backprojection tests were performed on raw, uncalibrated measurement file sets as listed below. The erroneous files were discussed in Section 4.3.

1. 18 GHz, 1 inch resolution, erroneous files included
2. 18 GHz, 1 inch resolution, erroneous file compensated
3. 10 GHz, 2 inch resolution, erroneous files included
4. 10 GHz, 1 inch resolution, erroneous file compensated
5. 16 GHz, 2 inch resolution, erroneous files included
6. 16 GHz, 1 inch resolution, erroneous file compensated

In each test, four backprojection plots were generated: the 6 inch diameter sphere, the 18 inch diameter sphere, the cylinder, and the background. (Refer to Chapter 5 for detailed target descriptions.) Plot resolution of 1 inch was obtained for this analysis. Each backprojection plot in this appendix displays $\left|\tilde{S}_{m,n}\right|$ in dB-volt as a function of both m (horizontal location) and n (vertical location) at the "down range" position of the target and support pedestal. Over-layed on each plot is a scale drawing of the support pedestal and all targets. This overlay is shown in Figure 7.1. Note that all three targets are shown on the overlay, even though the backprojection plots are for a single target only. Each backprojection plot title gives the actual target which was present.

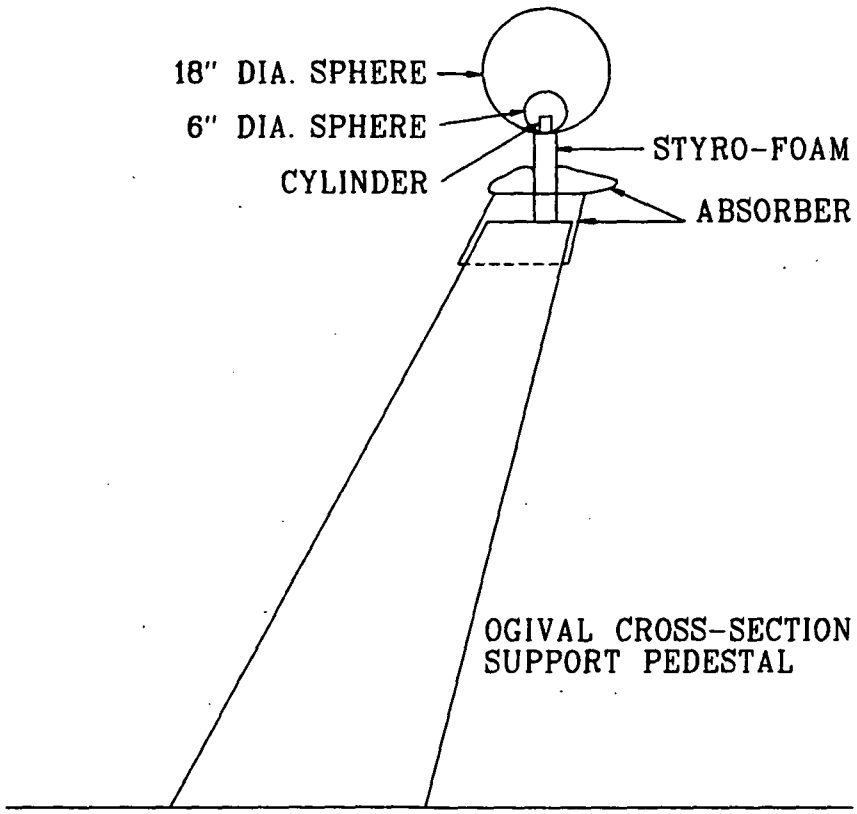

Figure 7.1: Overlay of support pedestal and targets. Same scale as backprojection plots.

7.1 Erroneous File Problems

The effects of erroneous files were eliminated in the linear backprojection plots presented in Chapter 4 by choosing error free linear scans from the full two-dimensional scan. In the two-dimensional backprojection algorithm, two methods were used to deal with the erroneous files.

The first method included the erroneous files as if they were accurate. Since the error had a random frequency onset and a maximum deviation of 3-4 dB from the expected frequency response, the effect was hoped to be small. The second method set the erroneous file data to zero, and appropriately decreased the total sample number. This second method can cause periodic variations in a backprojection plot if the erroneous files are not randomly distributed by position.

Neither method is perfect. However, the background "noise" level produced by including the erroneous files was greater than the periodic error effect observed when the erroneous files were removed. A good example of this is seen in Figures 7.2 and 7.3. These figures show a backprojection of the cylinder at the obtuse bistatic angle with and without the erroneous files, respectively. Note that erroneous file removal lowers the background level of Figure 7.3 by approximately 20 dB compared to Figure 7.2.

All backprojection plots generated contain many terms which are periodic in space, regardless of the method of erroneous file compensation. These responses could be induced by the side-lobe structure of the probe antenna, the data processing, or caused by an aliasing of signals from beyond the focus-plane window of interest.

7.2 Resolution and Aliasing

Backprojection plot resolution increases as the frequency increases. However, the increased aliasing of signals from outside the scan plane window into the plot is sacrificed for better resolution.

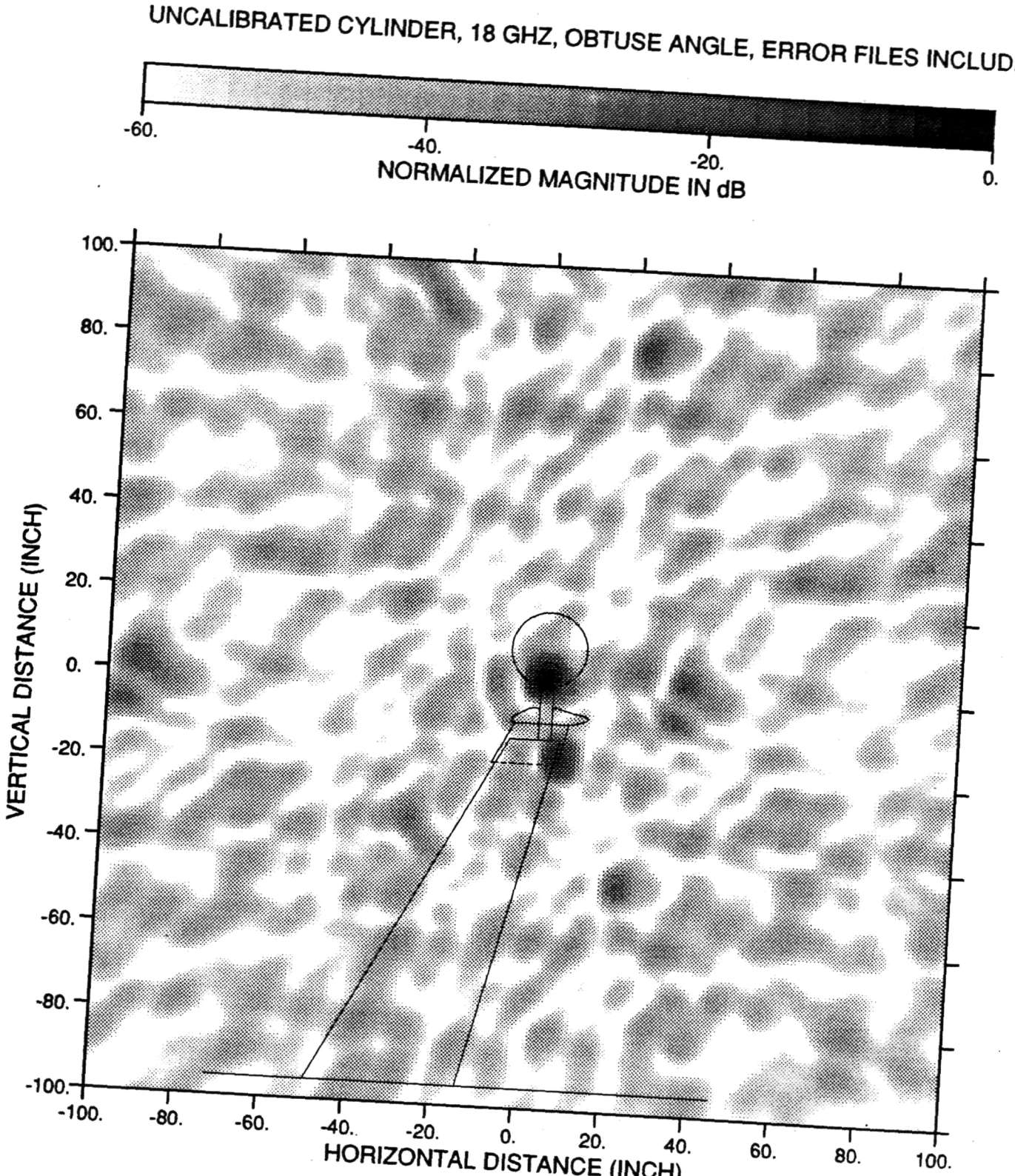

Figure 7.2: Uncalibrated cylinder backprojection plot. 18 GHz, Obtuse bistatic angle, Erroneous files included, Normalized by -42 dB

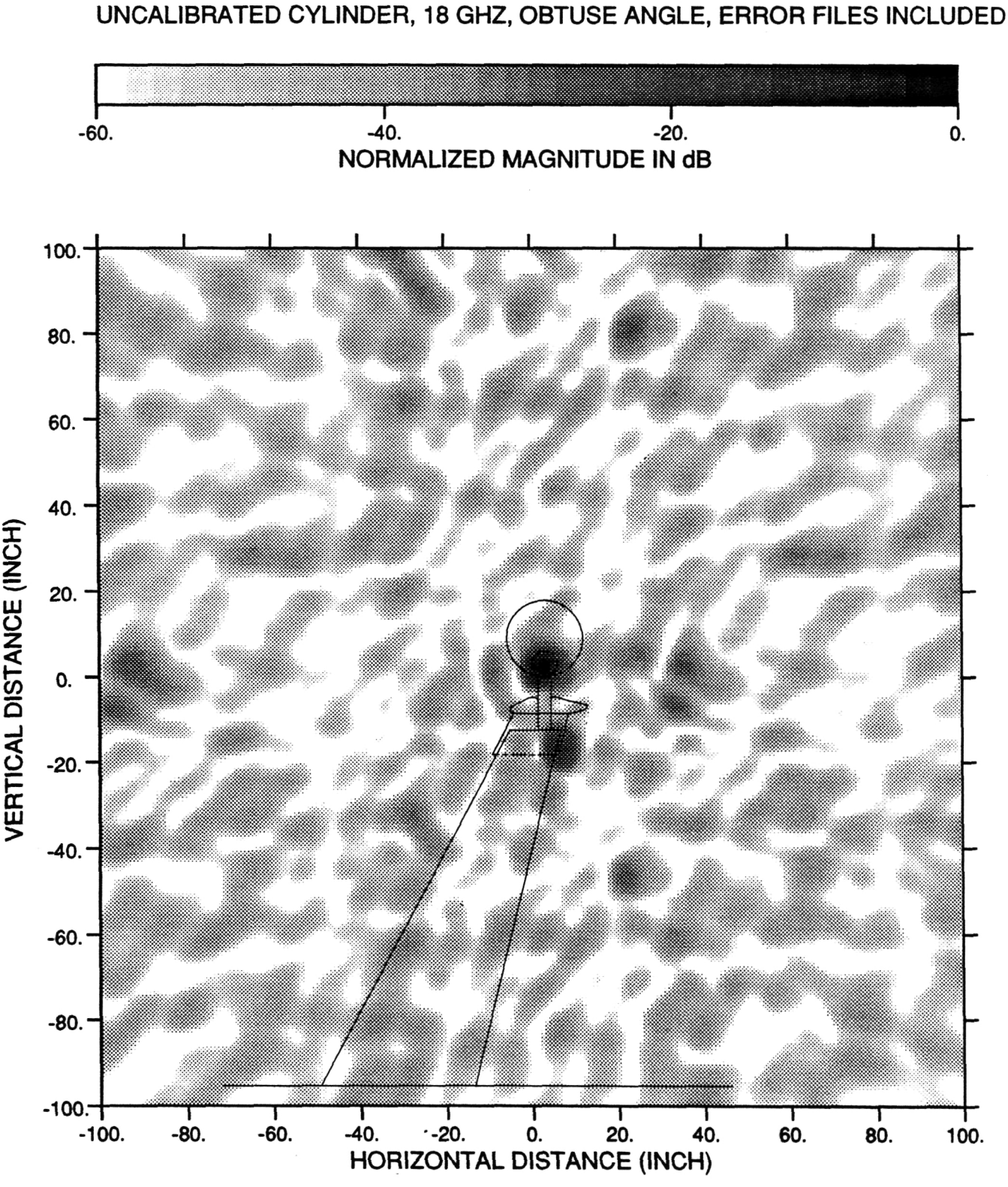

Figure 7.3: Uncalibrated cylinder backprojection plot. 18 GHz, Obtuse bistatic angle, Erroneous files removed, Normalized by -42 dB

C-2

Our first tests were performed at 18 GHz, at which the direct reflection off the main reflector edge is aliased to positions which are removed from the target zone, but still appear in the backprojection plot of Figure 7.6. To remove these reflector-edge aliases further from the target, 10 GHz test were performed (See Figure 7.4). The closest observed alias term at 10 GHz is approximately 60 inches from the target, the second alias term can not exist below 12.5 GHz.

The resolution ability of the backprojection algorithm can be estimated as the half-power beam-width of the aperture distribution far-field pattern. In this case the taper function was a cosine squared function which gives a 3 dB beam width of $83.2\lambda/D$ degrees, which for 10 GHz at 17.5 feet down range results in a resolution of approximately 1 foot. This resolution is larger than the separation of the scattering mechanisms of interest.

Therefore, 16 GHz tests were performed to increase the resolution to 7 inches, at the expense of increased alias effects. At 16 GHz, the alias of the main reflector edge is only 30 inches away from the target. At approximately 13 GHz, this alias would appear at the target position. Below 5.9 GHz, there is no aliasing for the one inch sample spacing.

The expected alias location of the direct reflection off the rolled edge of the reflector was computed for the obtuse bistatic angle case and is noted in the 10, 16 and 18 GHz background backprojection plots of Figures 7.4, 7.5, and 7.6.

7.3 Scattering Term Identification

It is important to remember that the response locations of specific scattering structures are frequency independent. Terms due to aliasing effects will move as the frequency changes. We also observed terms which corresponded to locations of specific chamber scattering structures which did not appear in all frequency plots. The scattering from such structures may be frequency dependent.

Scattering from the ogival target support pedestal can be characterized by ex-

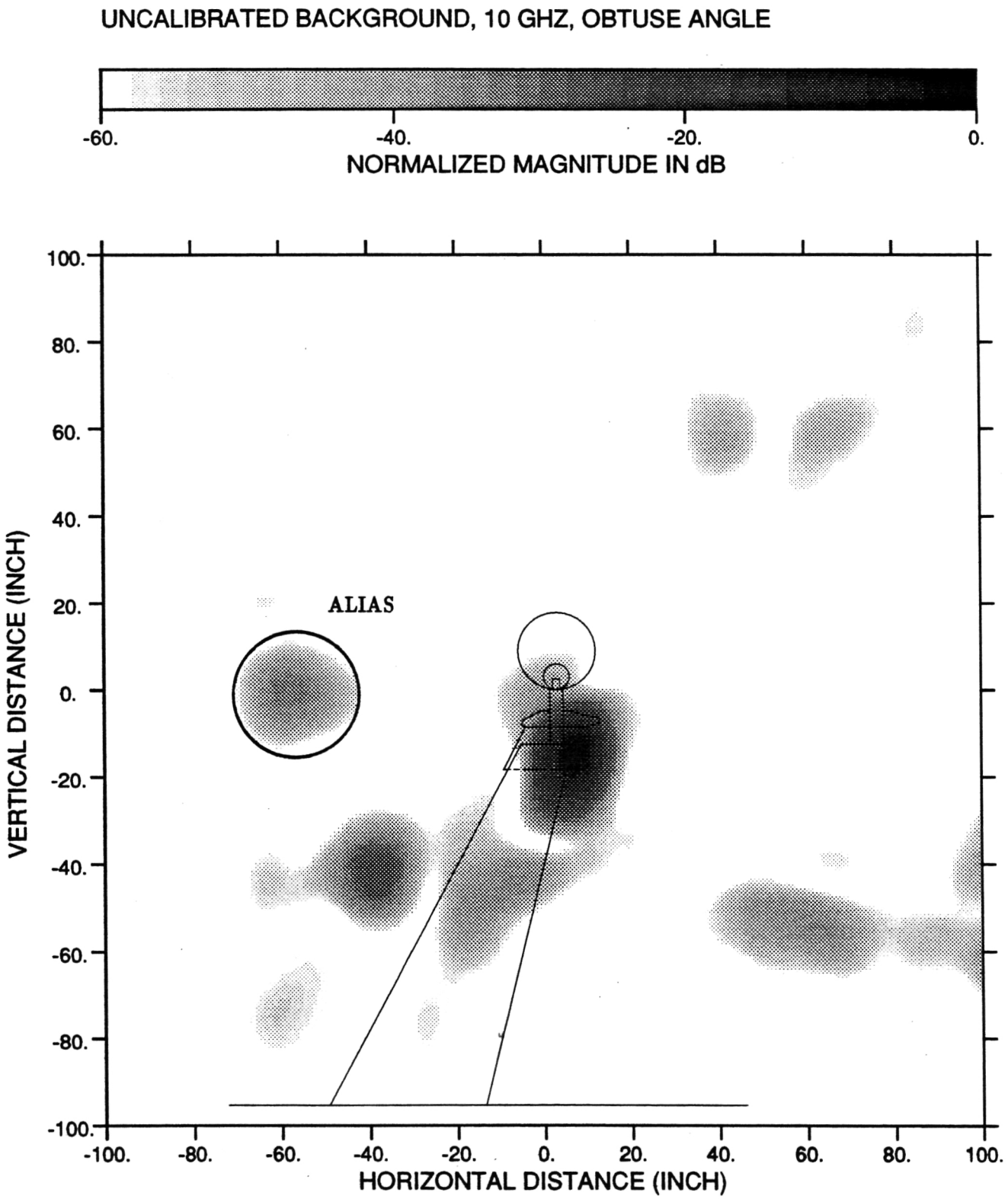

Figure 7.4: Uncalibrated background backprojection plot. 10 GHz, Obtuse bistatic angle, Erroneous files removed, Normalized by -5 dB

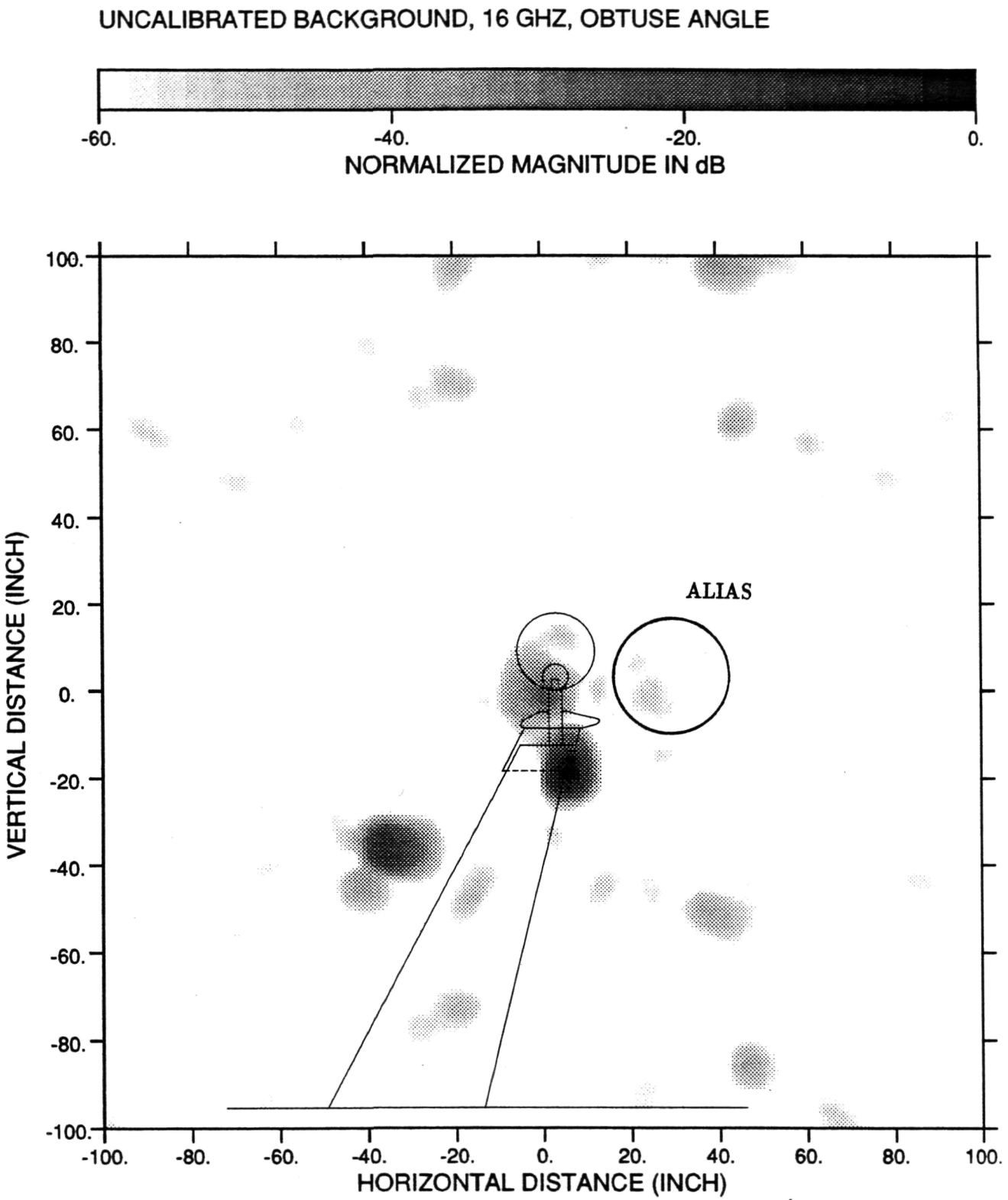

Figure 7.5: Uncalibrated background backprojection plot. 16 GHz, Obtuse bistatic angle, Erroneous files removed, Normalized by -24 dB

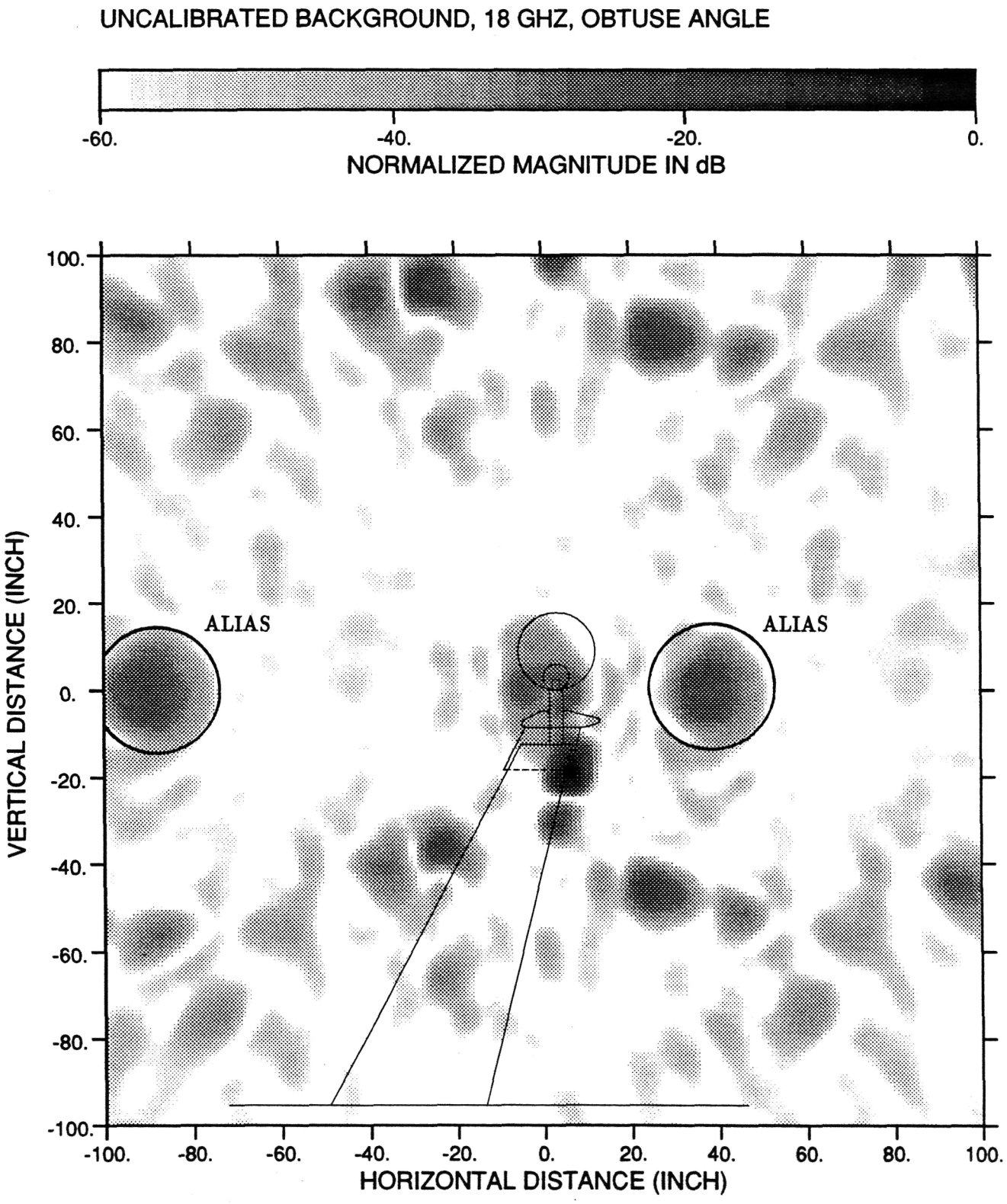

Figure 7.6: Uncalibrated background backprojection plot. 18 GHz, Obtuse bistatic angle, Erroneous files removed, Normalized by -58 dB

amining Figures 7.4, 7.5, and 7.6 presented earlier. In all three plots, there are two terms emanating from near the top of the pedestal. One term appears to be originating from the junction of the absorber cover and the metal side of the ogive. The other term originates at the top of the absorber cap. A third term found in all three plots occurs approximately 20 inches to the left of, and two-thirds as high as the support pedestal. This term may be due to a signal from the far side of the ogive coming around the surface and diffracting off the back edge.

Figures 7.7, 7.8, and 7.9 show the backprojection of the background measurement for the 10, 16, and 18 GHz cases at the acute bistatic angle. As was the case for the obtuse bistatic angle there are two terms occurring near the top of the pedestal, at the absorber cap and metal side junction, and near the styrofoam column. However, there is no signal which could be attributed to a wave coming around from the far side of the ogive support pedestal. This agrees with the geometrical differences between the acute and obtuse test setups described in Section 5.1. Note once again the spatial periodic terms near the edges of the 16 and 18 GHz plots.

The bistatic scattering in dBsm of the support pedestal can be estimated from the data in Figures 7.5, 7.9, 7.12, 7.13, 7.15, and 7.16. This was done by normalizing the response of the pedestal alone by the response of the 6 and 18 inch spheres independently and then scaling to the known far field RCS in dBsm of the spheres and taking the average of the two answers. [1] This process resulted in an RCS estimate for the pedestal of -42.5 dBsm for the 65 degree bistatic angle at 18 GHz and -22 dBsm for the 109 degree angle at 16 GHz. An accepted approximation for the monostatic RCS of this pedestal is -80 dBsm.

Backprojection plots enable analysis of signals from the room and associated structures. The plot of the cylinder at 10 GHz for the obtuse bistatic angle in Figure 7.10 is a good example. Many of the terms have been labeled as to their known or suspected causes. These scatterers were identified by a graphical projection

[1] Note that values read from the backprojection plots need division by 2.0 to compare with values in dBsm.

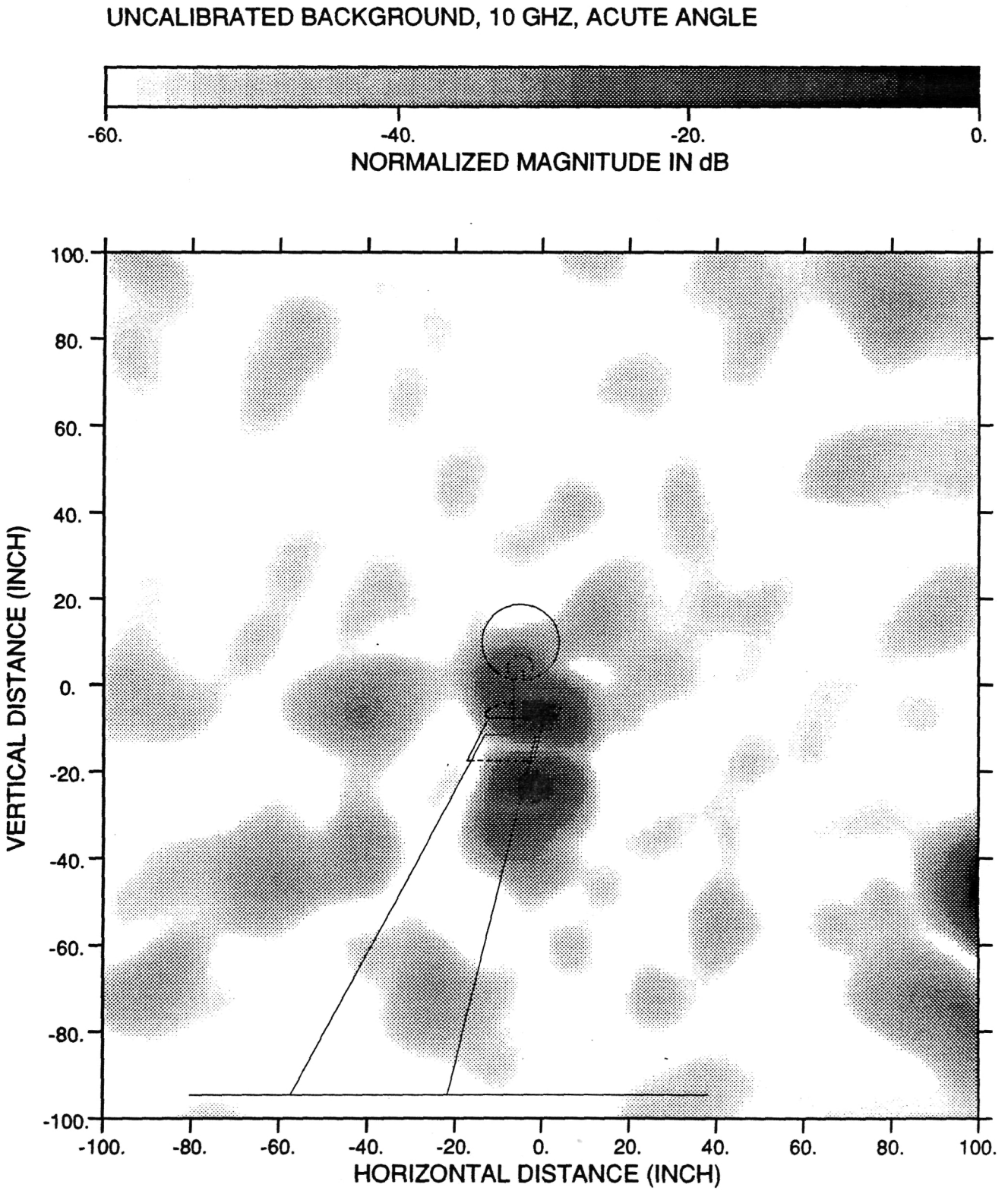

Figure 7.7: Uncalibrated background backprojection plot. 10 GHz, Acute bistatic angle, Erroneous files removed, Normalized by -62 dB

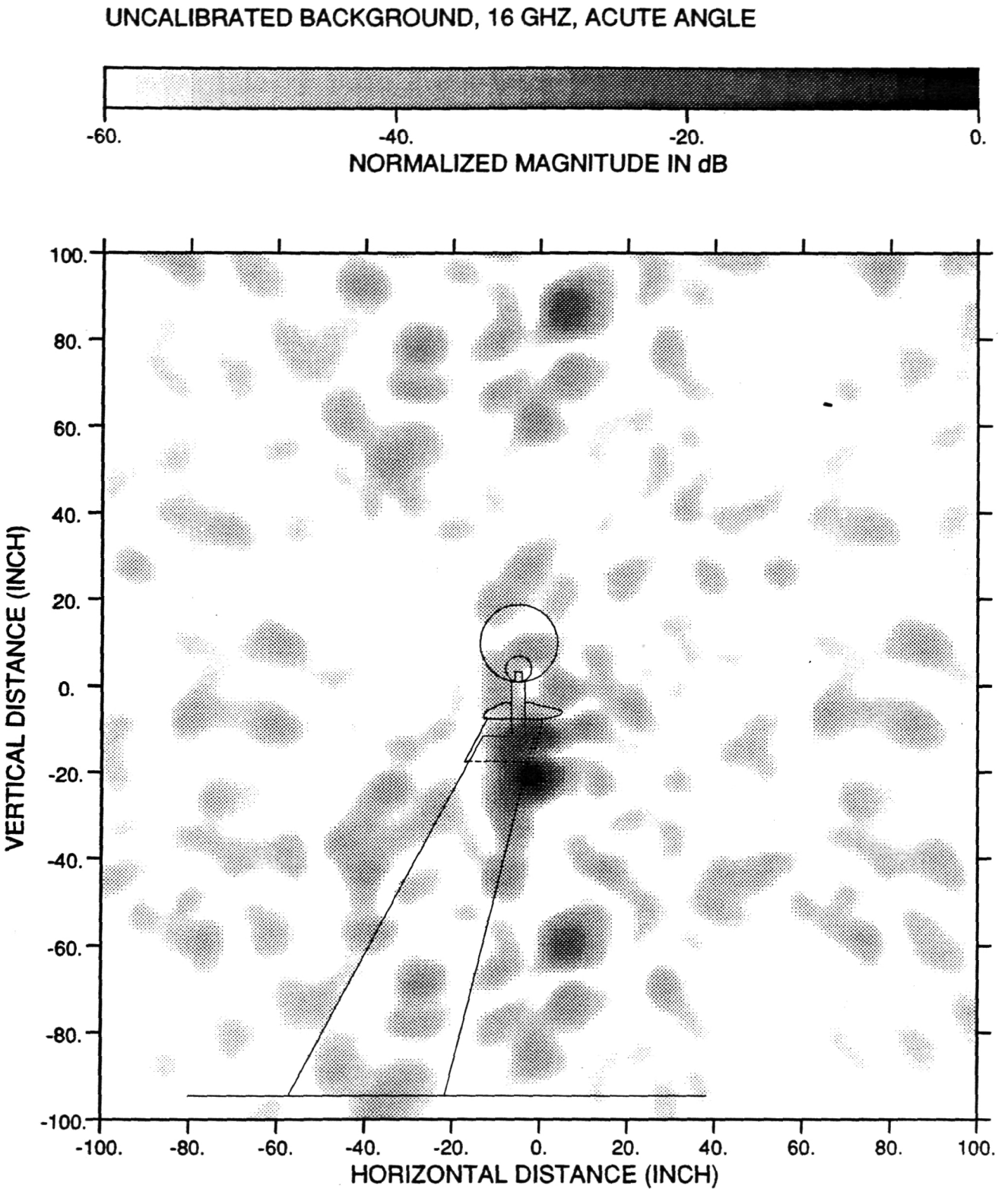

Figure 7.8: Uncalibrated background backprojection plot. 16 GHz, Acute bistatic angle, Erroneous files removed, Normalized by -71 dB

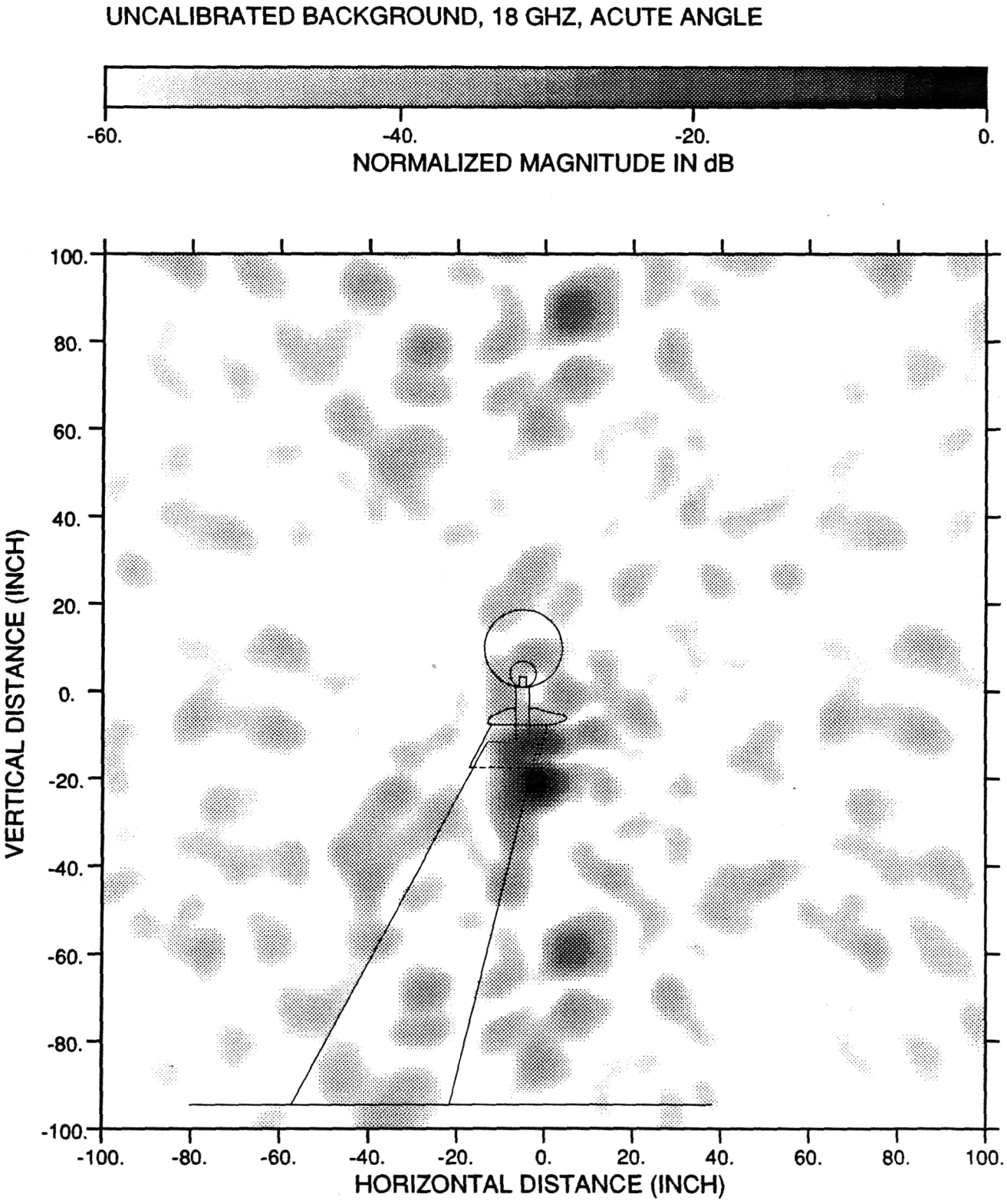

Figure 7.9: Uncalibrated background backprojection plot. 18 GHz, Acute bistatic angle, Erroneous files removed, Normalized by -99 dB

process using top and side view scale drawings of the compact range and the known locations of the suspected scattering structures.

Terms such as the aliased main beam, the ceiling lights, and the absorber on the floor must each be removed by data processing to compute accurate far-field scattering due to the test target alone. Recalling from Chapter 4 that the plane wave processing induces a spatial window of at most 30 inches square on this data, and the aim process was used to center the window on the target response, it is easily visualized how many of these terms were removed.

Figures 7.11 through 7.16 show backprojection plots of the three targets for both the acute and obtuse bistatic angles. As expected, the specular scattering term moves relative to the target position. It corresponds to geometrical optics location predictions. Note in Figure 7.12, the term just below the specular scattering of the 6 inch diameter sphere is located where interactions between the sphere and the top of the absorber are expected. Examination of the associated background plot (Figure 7.9) indicates that this term is approximately 40 dB above the background measured at that location. This term is classified as a target–pedestal interaction.

The cylinder was chosen as a test target because it was expected that the interactions between the cylinder and the support column would be smaller than the interactions between the spheres and the column due to the cylinder geometry. Although the difference in scattering center height between the cylinder and the 6 inch diameter sphere in Figures 7.11 and 7.12 obscures the top of the absorber cap somewhat, it can be seen in these figures that the cylinder does not contain a target–pedestal interaction term. The 18 inch diameter sphere shown in Figure 7.13 contains an interaction term which is not visible for the dynamic range shown, but it is visible in Figure 7.16, at the obtuse angle.

Figure 7.15 shows the 6 inch diameter sphere at 16 GHz for the obtuse bistatic angle. Note the response located just to the left and below the specular response of the sphere. This term is also seen at 18 GHz, but at 10GHz the plot is not resolved

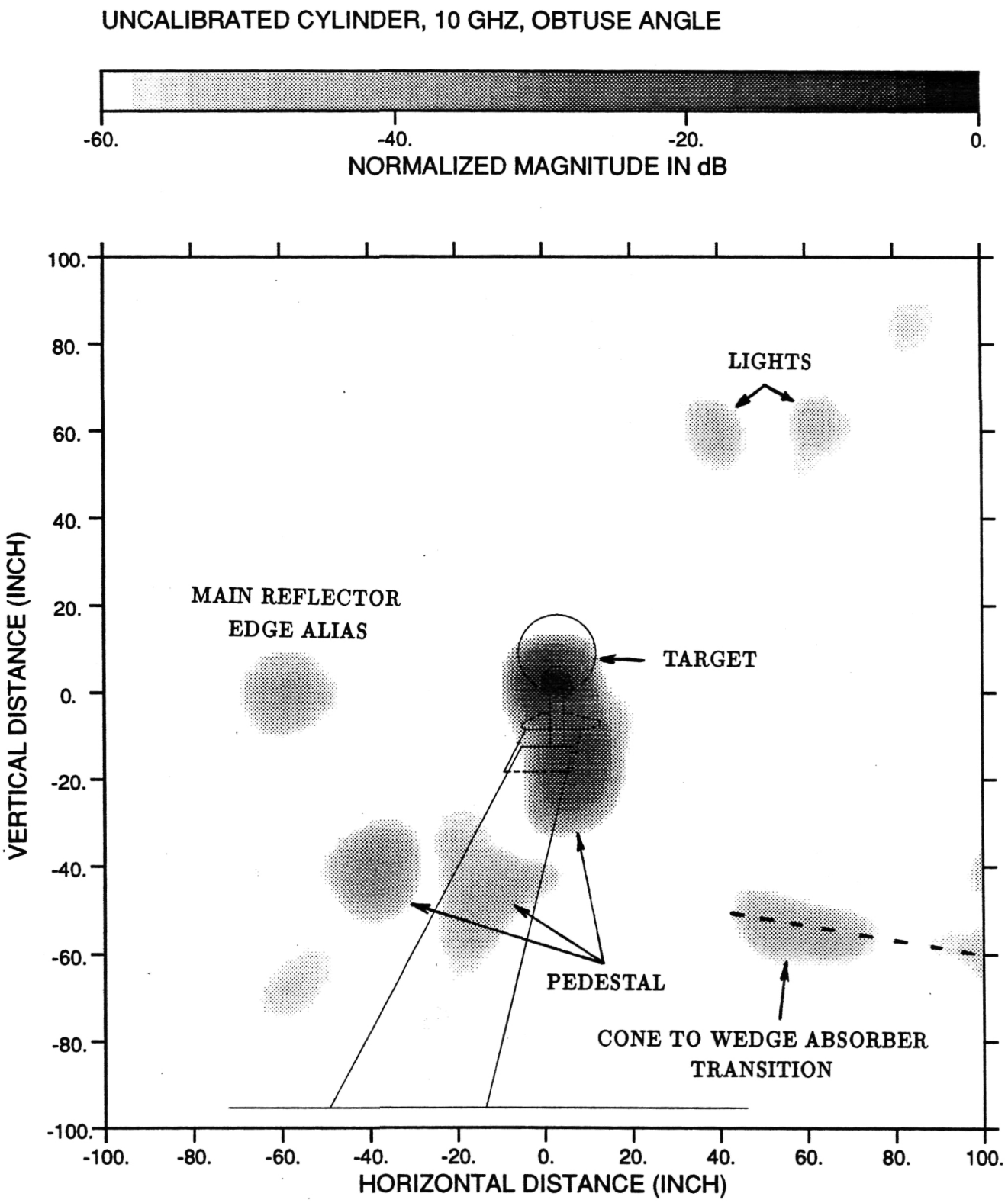

Figure 7.10: Uncalibrated cylinder backprojection plot. 10 GHz, Obtuse bistatic angle, Erroneous files removed, Normalized by 3 dB

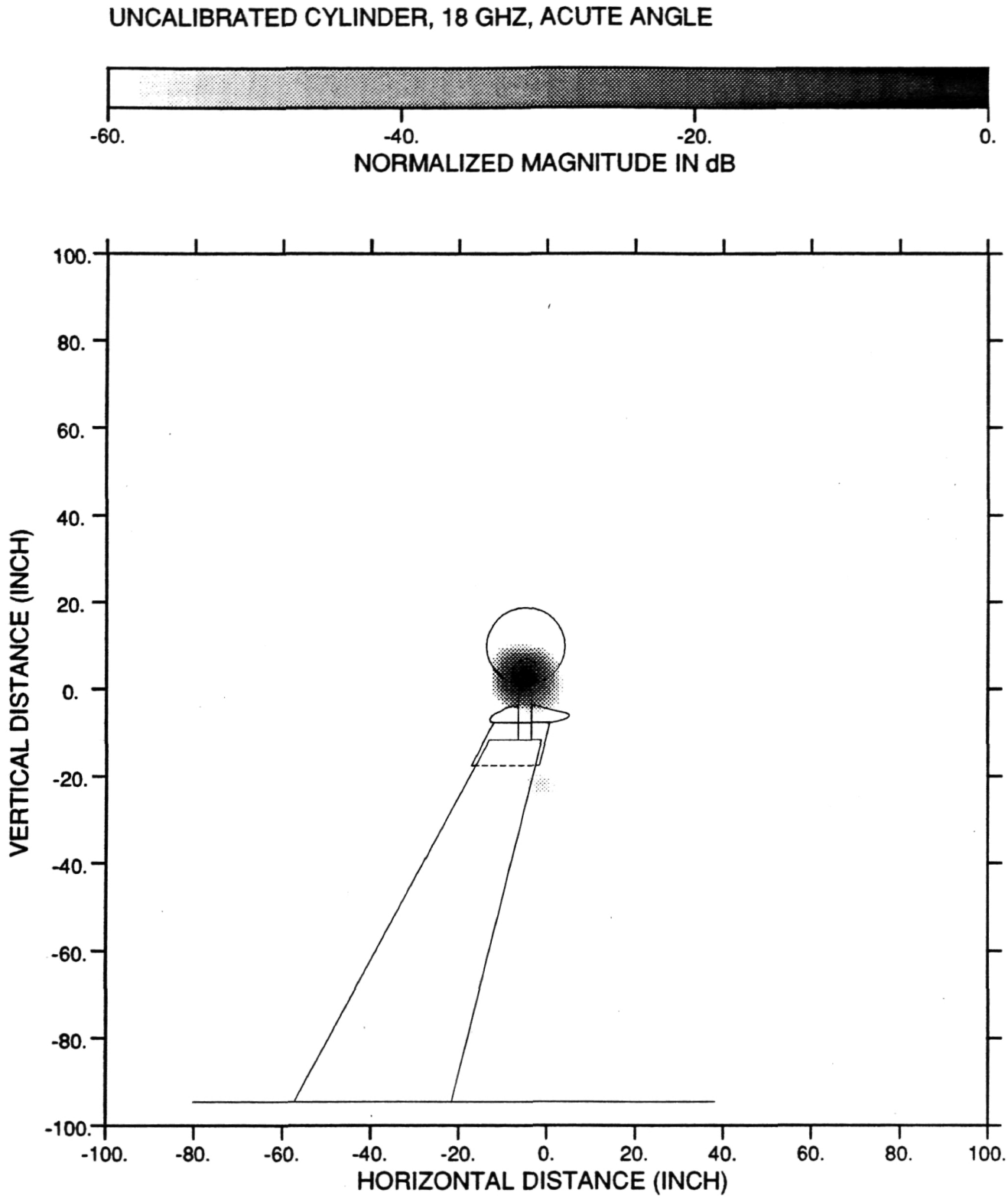

Figure 7.11: Uncalibrated cylinder backprojection plot. 18 GHz, Acute bistatic angle, Erroneous files removed, Normalized by -46 dB

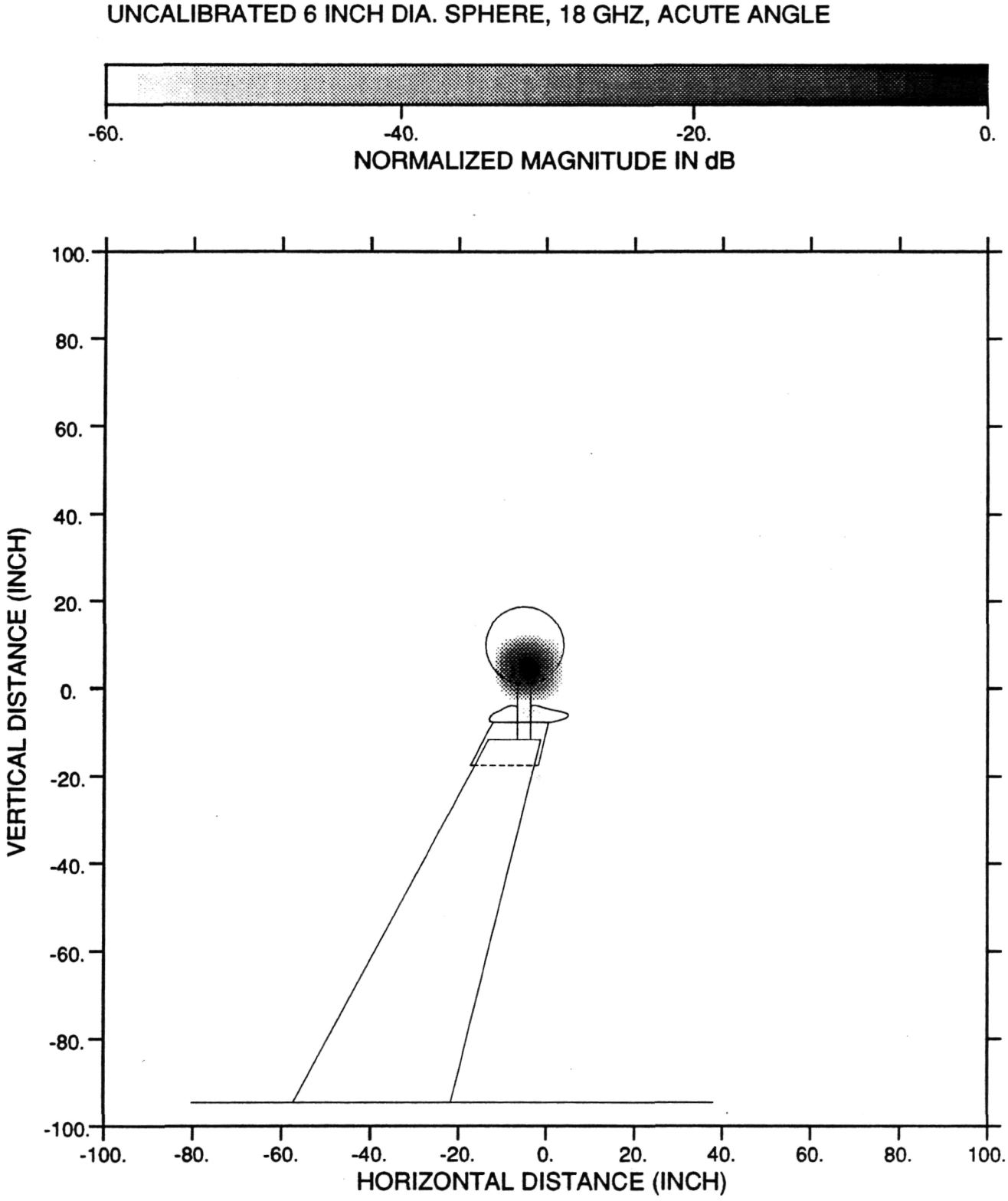

Figure 7.12: Uncalibrated 6 inch diameter sphere backprojection plot. 18 GHz, Acute bistatic angle, Erroneous files removed, Normalized by -49 dB

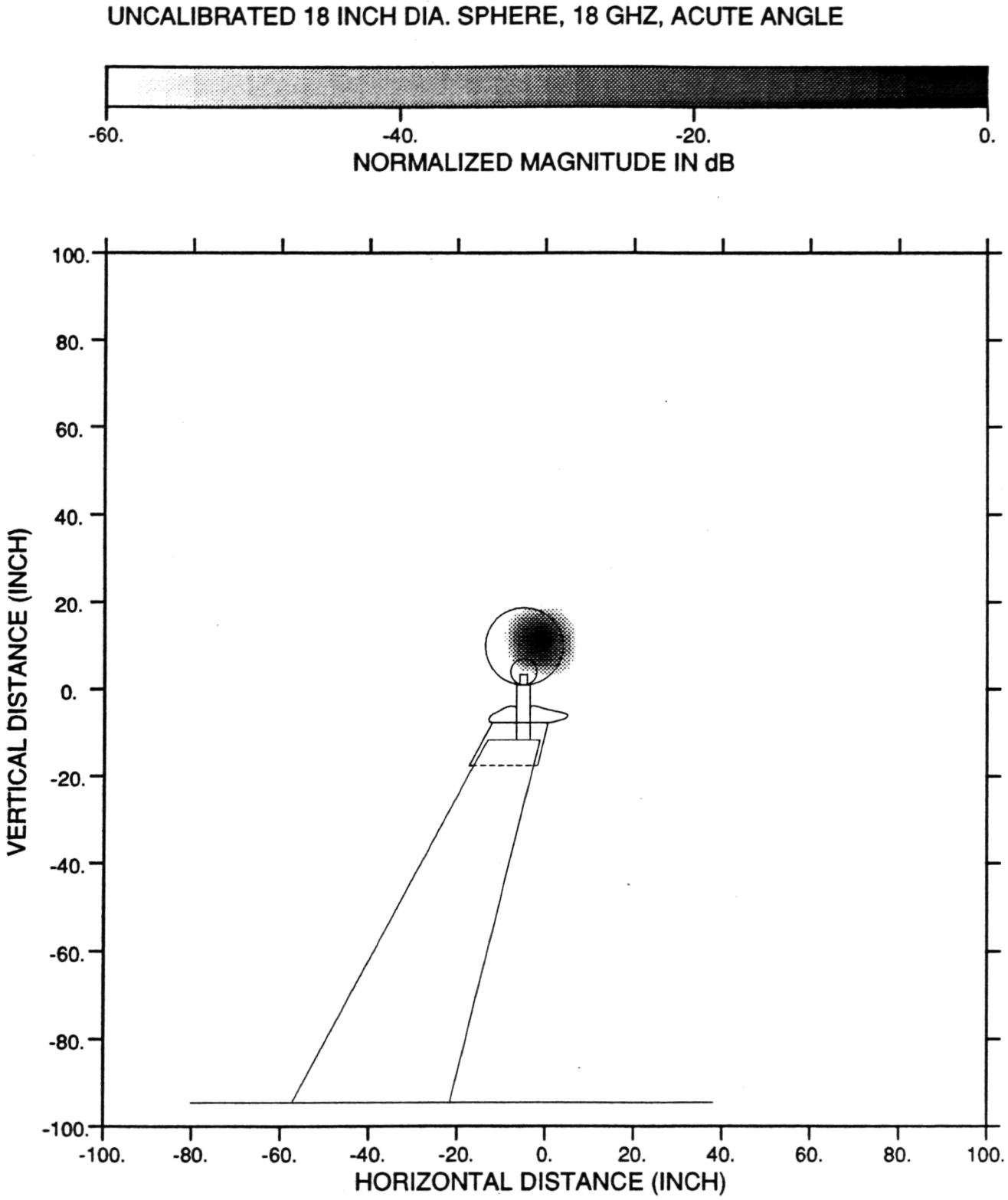

Figure 7.13: Uncalibrated 18 inch diameter sphere backprojection plot. 18 GHz, Acute bistatic angle, Erroneous files removed, Normalized by -28 dB

enough to determine if the same phenomena exists. We have not yet associated this term with a known physical scattering mechanism or an alias.

7.4 Conclusions

We have demonstrated the imaging of bistatic scattering data using the measurements of the planar scanner system. It was shown that specific terms due to the test target, the target support pedestal, and associated interactions can be identified and quantified. Techniques for the identification of spurious terms due to aliasing were given. Verification of the plane wave processing performance in removing non-target related signals was shown. An estimate of the bistatic RCS of the ogival target support column was given.

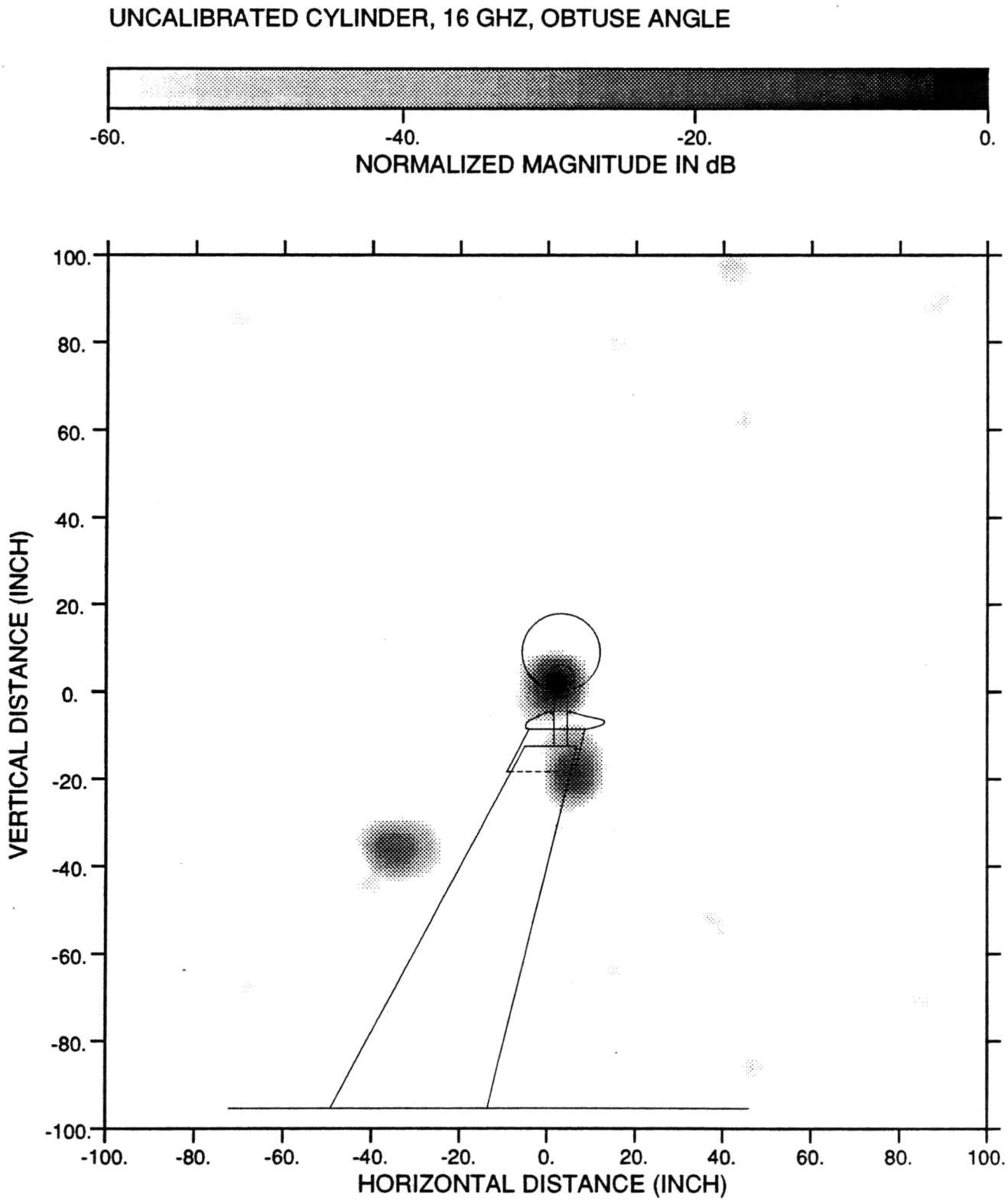

Figure 7.14: Uncalibrated cylinder backprojection plot. 16 GHz, Obtuse bistatic angle, Erroneous files removed, Normalized by -12 dB

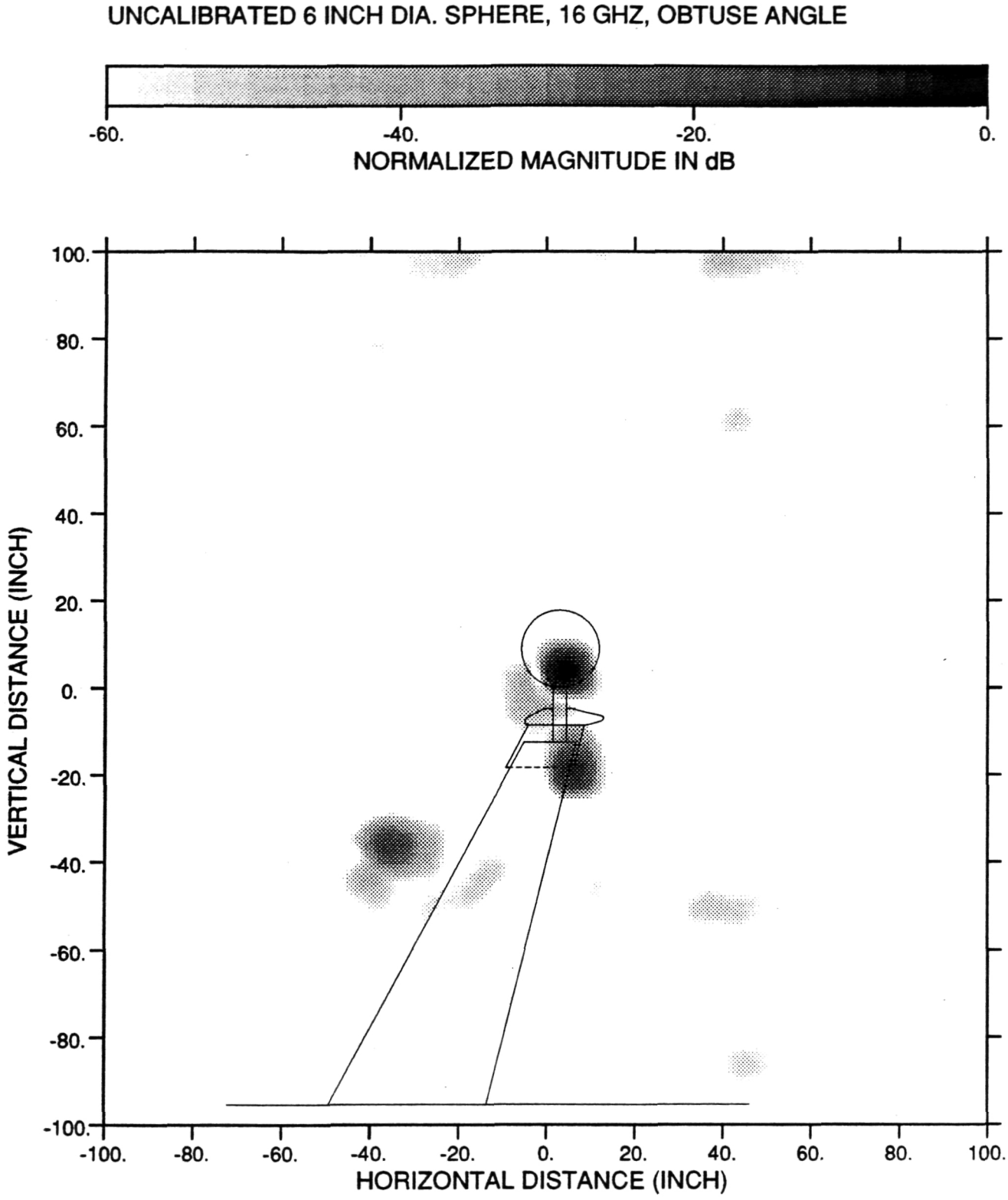

Figure 7.15: Uncalibrated 6 inch diameter sphere backprojection plot. 16 GHz, Obtuse bistatic angle, Erroneous files removed, Normalized by -15 dB

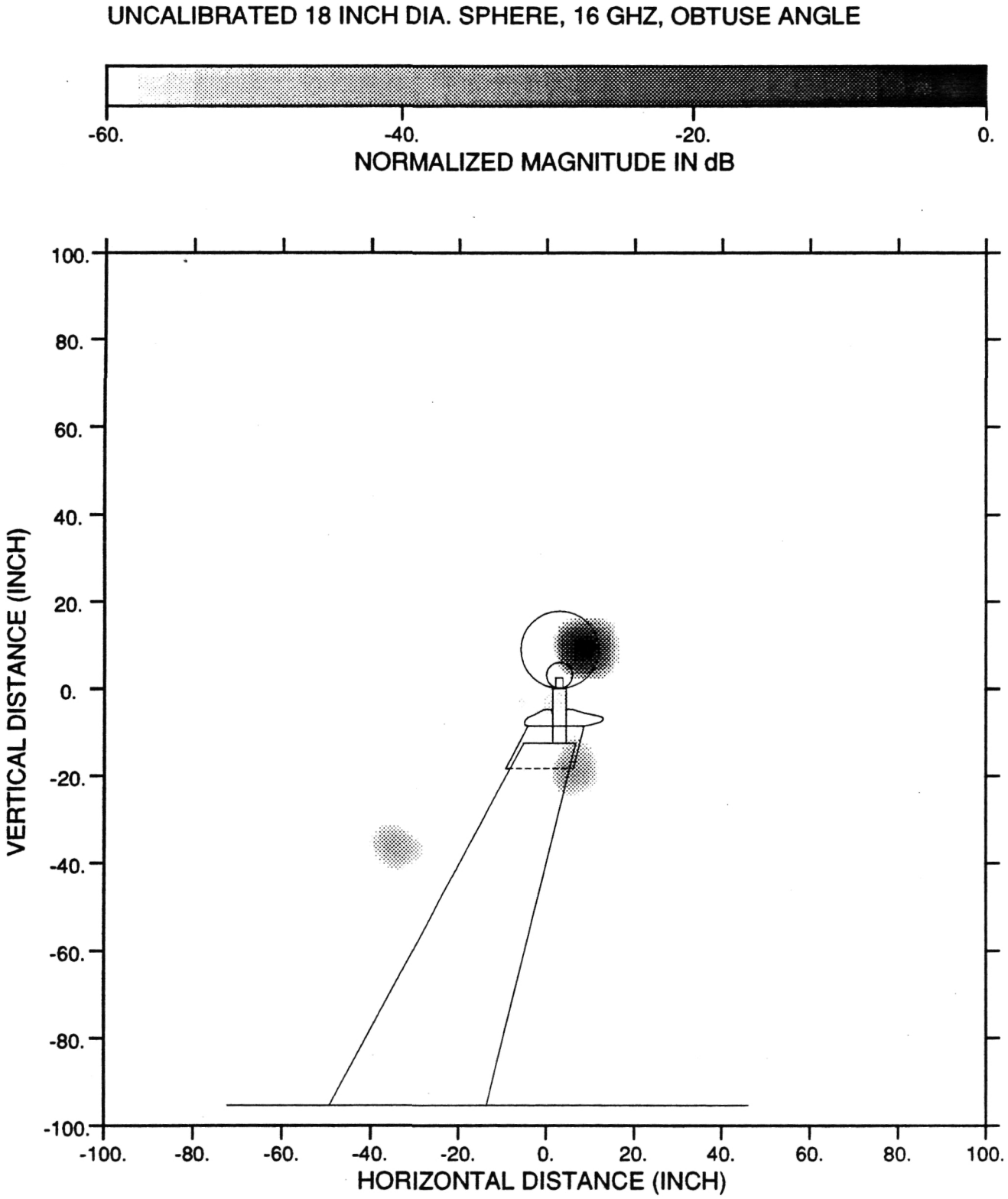

Figure 7.16: Uncalibrated 18 inch diameter sphere backprojection plot. 16 GHz, Obtuse bistatic angle, Erroneous files removed, Normalized by 8 dB

Chapter 8

Plane Wave Processing Fortran Code

```
OPTIONS /EXTEND_SOURCE
C*******$*********$*********$*********$*********$*********$******* PROGRAM
TDAP C*******$*********$*********$*********$*********$*********$******* C

This program inputs ttt files and combines them into a single  C
frequency scan file by the use of windowing functions and vector C
summation of all files at each frequency. C  C Stephen Tuhela-Reuning C

March 21, 1991
C*******$*********$*********$*********$*********$*********$*******

IMPLICIT NONE

C ************************************
C * function subroutine declarations *
C ************************************
REAL MULT,DELAY
INTEGER SEARCH

C ************************
C * Variable Declarations *
C ************************
REAL XBEG,XEND,XSTEP,YBEG,YEND,YSTEP,FBEG,FSTEP
REAL MAGMLT,PHSLAG,PERCNT,PHSDLY,M,P,NORML
REAL RO,REFHI,REFLF,FREQ,PDU,PDL,PD_UP,PD_LF
REAL IN(2,5000),OUT(2,5000),BLOCK(31,31,2,5000)
```

```
CHARACTER IFLNM*21,FLNM*21,HDR*512,IHDR*512,EXTN*3,WINDIS*4

INTEGER XLP,YLP,FLP,XNUM,YNUM,FNUM,REAERR,POS,LCV
INTEGER ERX(100),ERY(100),ERNUM,ERLCV,NUMTOTAL,FNDAT

FNDAT=1
C ****************************
C * GET USER INPUT           *
C ****************************
PRINT*,'ENTER THE X DIR: BEGIN,END,STEP'
READ*,XBEG,XEND,XSTEP
PRINT*,'ENTER THE Y DIR: BEGIN,END,STEP'
READ*,YBEG,YEND,YSTEP
PRINT*,'ENTER THE FIRST FILENAME'
READ(*,'(A)')IFLNM
PRINT*,'ENTER THE OUTPUT FILE EXTENSION'
READ(*,'(A)')EXTN

PRINT*,'ENTER THE NUMBER OF ERROR FILES'
READ*,ERNUM

IF (ERNUM.NE.0) THEN
    DO ERLCV=1,ERNUM
PRINT*,'ENTER THE COORDINATES (X,Y) OF THE (NEXT) ERROR FILE'
READ*,ERX(ERLCV),ERY(ERLCV)
    END DO
END IF

PRINT*,'ENTER THE WINDOW: PERCENT,PHASE_DELAY'
READ*,PERCNT,PHSDLY

WRITE(WINDIS,'(I4)')NINT((PERCNT*100)+(PHSDLY/10))

PRINT*,'ENTER THE REFERENCE TARGET DISTANCE [IN]'
READ*,RO
PRINT*,'ENTER THE REFERENCE TARGET HEIGHT DISPLACEMENT [IN]'
READ*,REFHI
PRINT*,'ENTER THE REFERENCE TARGET LEFT DISPLACEMENT [IN]'
READ*,REFLF

C ***************************************
C * PART OF THE PHASE DELAY COMPUTATION *
```

```
C ***************************************
PDU=5.31976356E-04*SIN(ATAN2(REFHI,R0))
PDL=5.31976356E-04*SIN(ATAN2(REFLF,R0))

C *********************************
C * Optional input data printout *
C *********************************
C PRINT*,'XBEG =',XBEG,', XEND =',XEND,', XSTEP =',XSTEP
C PRINT*,'YBEG =',YBEG,', YEND =',YEND,', YSTEP =',YSTEP
C PRINT*,'INITIAL FILENAME =',IFLNM

C ***************************************
C * Compute the num pts in x and y dir *
C ***************************************
IF ((XEND .EQ. XBEG).AND.(YEND .EQ. YBEG)) THEN
    XNUM=1
    YNUM=1
ELSE IF (XEND .EQ. XBEG) THEN
    XNUM=1
      YNUM=(YEND-YBEG+1.0)/YSTEP
ELSE IF (YEND .EQ. YBEG) THEN
    YNUM=1
    XNUM=(XEND-XBEG+1.0)/XSTEP
ELSE
    XNUM=(XEND-XBEG+1.0)/XSTEP
    YNUM=(YEND-YBEG+1.0)/YSTEP
END IF


C ***************************************
C * Main program loop: thru x and y dir *
C ***************************************
DO XLP=1,XNUM,1
  DO YLP=1,YNUM,1
    CALL MKNAME(IFLNM,FLNM,XLP,XBEG,YLP,YBEG,YSTEP) ! make filename
    CALL FRQREA(FLNM,IN,HDR,FBEG,FSTEP,FNUM,REAERR)     ! read file

C     ********************
C     * Error handlers *
C     ********************
    IF (REAERR .EQ. 1) THEN
PRINT*,'***FILE READ ERROR***'
```

```
STOP
    ELSE IF (REAERR .EQ. 2) THEN
PRINT*,'***FILE OPEN ERROR***'
STOP
    ELSE IF (REAERR .EQ. 4) THEN
PRINT*,'***HEADER DECODE ERROR***'
    END IF

    IF ((XLP.EQ.1).AND.(YLP.EQ.1)) THEN
IHDR=HDR      ! save first header
PRINT*,'NUMBER OF FREQ PTS PER FILE =',FNUM
    ENDIF

    IF((ERNUM.NE.0).AND.
+ (SEARCH(XBEG,XLP,YBEG,YLP,ERX,ERY,ERNUM,FNDAT).EQ.1))THEN
C **********************************
C               * SET ALL BLOCK VS FREQ TO ZERO *
C **********************************
PRINT*,FLNM,' IS BEING SKIPED.'
DO FLP=1,FNUM
    BLOCK(XLP,YLP,1,FLP)=0.0
    BLOCK(XLP,YLP,2,FLP)=0.0
END DO
    ELSE
C ****************************
C * Amplitude Taper function *
C ****************************
MAGMLT=MULT(XLP,XNUM,PERCNT)*
     + MULT(YLP,YNUM,PERCNT)

C ************************
C * Phase taper function *
C ************************
PHSLAG=DELAY(XLP,XNUM,PERCNT,PHSDLY)+
     + DELAY(YLP,YNUM,PERCNT,PHSDLY)

C *****************************
C * Loop thru each frequency *
C *****************************
DO FLP=1,FNUM,1
    FREQ=FBEG+((FLP-1)*FSTEP)
    PD_UP=PDU*FREQ
```

```
      PD_LF=PDL*FREQ
C       * change to mag/phs *
      M=SQRT((IN(1,FLP)**2)+(IN(2,FLP)**2))
      P=ATAN2(IN(2,FLP),IN(1,FLP))
C       * apply window functions *
      M=M*MAGMLT
      P=P+PHSLAG + (16-YLP)*PD_UP + (16-XLP)*PD_LF
C       * convert back to real/imag and store *
      BLOCK(XLP,YLP,1,FLP)=M*COS(P)
      BLOCK(XLP,YLP,2,FLP)=M*SIN(P)
END DO    ! FLP loop
      ENDIF
    END DO        ! YLP loop
    PRINT*,'COLUMN(S) READ =',XLP              ! User progress monitor
END DO            ! XLP loop

PRINT*,'PROCESSING...'
C ***************************************
C * Sum the layer at a single frequency *
C ***************************************
DO FLP=1,FNUM,1
      OUT(1,FLP)=0.0    ! initialize to zero
      OUT(2,FLP)=0.0
      DO XLP=1,XNUM,1
DO YLP=1,YNUM,1    ! vector addition
      OUT(1,FLP)=OUT(1,FLP)+BLOCK(XLP,YLP,1,FLP)
      OUT(2,FLP)=OUT(2,FLP)+BLOCK(XLP,YLP,2,FLP)
END DO
      END DO
C       * normalization *
      NUMTOTAL=(XNUM*YNUM)-ERNUM
      IF ((XNUM .EQ. 1).OR.(YNUM .EQ. 1)) THEN
NORML=(100.0/(100.0-PERCNT))/(NUMTOTAL)
      ELSE
NORML=((100.0/(100.0-PERCNT))**2)/(NUMTOTAL)
      END IF
      OUT(1,FLP)=OUT(1,FLP)*NORML
      OUT(2,FLP)=OUT(2,FLP)*NORML
END DO

IF(FNUM.EQ.1600)THEN
      PRINT*,'********** REDUCING FREQ SCAN SIZE! ***'
```

```
    FNUM=FNUM/2
    FSTEP=FSTEP*2
    DO LCV=1,FNUM
OUT(1,LCV)=OUT(1,LCV*2 - 1)
OUT(2,LCV)=OUT(2,LCV*2 - 1)
    END DO
    WRITE(IHDR(305:312),'(F8.1)') FSTEP
ENDIF

C ************************
C * create output filename *
C ************************
FLNM=IFLNM(1:INDEX(IFLNM,'.'))//EXTN
FLNM(INDEX(FLNM,'V')+1:INDEX(FLNM,'V')+4)=WINDIS

C *******************************
C * Optional header info output *
C *******************************
PRINT*, FLNM
C PRINT*, IHDR
C PRINT*, 'Beginning freq = ',FBEG
C PRINT*, 'Frequency step = ',FSTEP
C PRINT*, 'Number of freq pts = ',FNUM

C *********************
C * write output file *
C *********************
CALL FRQWRI(FLNM,OUT,IHDR,FBEG,FSTEP,FNUM,REAERR)
IF (REAERR.EQ.1) THEN
    PRINT*, '**** WRITE ERROR! ****'
ELSE IF (REAERR.EQ.2) THEN
    PRINT*, '**** FILE OPEN ERROR ****'
END IF

END

C******+***$*********$*********$*********$*********$*********$*********$*******
INTEGER FUNCTION SEARCH(XBEG,XLP,YBEG,YLP,ERX,ERY,ERNUM,FNDAT)
C******+***$*********$*********$*********$*********$*********$*********$*******
IMPLICIT NONE
REAL XBEG,YBEG
INTEGER XLP,YLP,ERX(100),ERY(100),ERNUM,FNDAT
```

```
SEARCH=0

IF((NINT(XBEG+XLP-1).EQ.ERX(FNDAT)).AND.
     +  (NINT(YBEG+YLP-1).EQ.ERY(FNDAT)))THEN
    SEARCH=1
    FNDAT=FNDAT+1
ENDIF

   RETURN
END

C*******$*********$*********$*********$*********$*********$*******
REAL FUNCTION DELAY(LP,NUM,PERCNT,PHSDLY)
C*******$*********$*********$*********$*********$*********$*******
C This routine computes the phase delay constant for the
C current position thus spatially filtering the data
C
C Stephen Tuhela-Reuning
C March 21, 1991
C*******$*********$*********$*********$*********$*********$*******

IMPLICIT NONE
   INTEGER LP,NUM
REAL PERCNT,PHSDLY

REAL WIDTH,ROLL,PT2,PI

PI=3.14159265359
WIDTH=NUM+1
ROLL=(PERCNT/100.0)*WIDTH
PT2=WIDTH-ROLL

IF (NUM .EQ. 1) THEN
    DELAY=0.0
    RETURN
END IF

IF (LP .LT. ROLL) THEN
    DELAY=(COS(PI*LP/(2.0*ROLL)-PI/2)-1)*PHSDLY*PI/180.0
ELSE IF (LP .GT. PT2) THEN
    DELAY=(COS(PI*(LP-PT2)/(2*ROLL))-1)*PHSDLY*PI/180.0
```

```
ELSE
    DELAY=0.0
END IF

C PRINT*, DELAY

RETURN
END

C******+***$********$********$********$********$********$*******
REAL FUNCTION MULT(LP,NUM,PERCNT)
C******+***$********$********$********$********$********$*******
C This routine computes the amplitude multiplication constant
C for the current position thus spatially filtering the data
C
C Stephen Tuhela-Reuning
C March 21, 1991
C******+***$********$********$********$********$********$*******

IMPLICIT NONE
   INTEGER LP,NUM
REAL PERCNT

REAL WIDTH,ROLL,PT2,PI

PI=3.14159265359
WIDTH=NUM+1
ROLL=(PERCNT/100.0)*WIDTH
PT2=WIDTH-ROLL

IF (NUM .EQ. 1) THEN
    MULT=1.0
    RETURN
END IF

IF (LP .LT. ROLL) THEN
    MULT=COS(PI*LP/(2.0*ROLL)+PI/2)**2
ELSE IF (LP .GT. PT2) THEN
    MULT=COS(PI*(LP-PT2)/(2*ROLL))**2
ELSE
    MULT=1.0
END IF
```

```
C PRINT*, MULT

RETURN
END

C******+***$*********$*********$*********$*********$*********$*******
SUBROUTINE MKNAME(IFLNM,FLNM,XLP,XBEG,YLP,YBEG,YSTEP)
C******+***$*********$*********$*********$*********$*********$*******
C This routine creates the next filename in the progression
C
C Stephen Tuhela-Reuning
C March 21, 1991
C******+***$*********$*********$*********$*********$*********$*******
IMPLICIT NONE
CHARACTER IFLNM*21,FLNM*21
INTEGER XLP,YLP
REAL XBEG,YBEG,YSTEP

CHARACTER*26 ALPHA
INTEGER POS

ALPHA='ABCDEFGHIJKLMNOPQRSTUVWXYZ'

IF (NINT(XBEG+XLP) .GT. 26) THEN
    POS=NINT(XBEG+XLP-26)
    FLNM(1:1)='A'
    FLNM(2:2)=ALPHA(POS:POS)
    FLNM(3:8)=IFLNM(INDEX(IFLNM,'-')-10:INDEX(IFLNM,'-')-5)
    WRITE(FLNM(9:12),FMT='(I4)')NINT((YBEG+YSTEP*(YLP-1))*10)
    FLNM(13:18)=IFLNM(INDEX(IFLNM,'-'):INDEX(IFLNM,'-')+5)
ELSE
    POS=NINT(XBEG+XLP)
    FLNM(1:1)=ALPHA(POS:POS)
    FLNM(2:7)=IFLNM(INDEX(IFLNM,'-')-10:INDEX(IFLNM,'-')-5)
    WRITE(FLNM(8:11),FMT='(I4)')NINT((YBEG+YSTEP*(YLP-1))*10)
    FLNM(12:17)=IFLNM(INDEX(IFLNM,'-'):INDEX(IFLNM,'-')+5)
END IF

DO POS=1,17,1
    IF (FLNM(POS:POS) .EQ. ' ') FLNM(POS:POS)='0'
END DO
```

```
C  PRINT*, FLNM

RETURN
END

C********$*********$*********$*********$*********$*********$*******
SUBROUTINE FRQWRI( FNM, YM, STT, LOFQ, INCRE, KT, FLG)
C********$*********$*********$*********$*********$*********$*******
C This routine is for writing the data to a freq domain file
C FNM    --- file name (input)
C YM     --- data array (input)
C STT    --- file header (input)
C LOFQ   --- start freq in mhz (input)
C INCRE --- increment freq in mhz (input)
C KT     --- number of points (input)
C FLG    --- error flag (output)
C
C Weihung Lin
C********$*********$*********$*********$*********$*********$*******

IMPLICIT NONE
CHARACTER*21 FNM     !file name
CHARACTER*512 STT    !header
INTEGER KT,K,FLG     !index and flag
REAL INCRE,LOFQ,ST   !scan var
REAL  YM(2,5000)     !data array (real/imaginary,frequency)

BYTE PARAM(512)      !header
CHARACTER*512 FG     !equal name
EQUIVALENCE ( FG , PARAM)

FLG=0                !clear flag
OPEN (UNIT=13,NAME=FNM,TYPE='NEW',FORM='UNFORMATTED',
     +  ERR=1000)  !open file
FG=STT
WRITE (13 , ERR = 999 ) PARAM  !read header
WRITE (13 ,ERR = 999 ) (YM(1,K),YM(2,K),K=1,KT)  !write data

CLOSE (13)  !close file

  RETURN
```

```
C       error handlers
999 CLOSE (13)
        FLG=1    !write error
RETURN
1000 CLOSE (13)
        FLG=2    !open error
RETURN
END


C********$*********$*********$*********$*********$*********$*******
SUBROUTINE FRQREA( FNM, YM, STT, LOFQ, INCRE, KT, FLG)
C********$*********$*********$*********$*********$*********$*******
C This routine is for reading the data from a freq domain file
C FNM    --- file name (input)
C YM     --- data array (output)
C STT    --- file header (output)
C LOFQ   --- start freq in mhz (output)
C INCRE --- increment freq in mhz (output)
C KT     --- number of points (output)
C FLG    --- error flag (output)
C
C Weihung Lin
C********$*********$*********$*********$*********$*********$*******

IMPLICIT NONE
CHARACTER*21 FNM     !file name
CHARACTER*512 STT    !header
INTEGER KT,K,FLG     !index and flag
REAL INCRE,LOFQ,ST   !scan var
REAL  YM(2,5000)     !data array (real/imaginary,frequency)

BYTE PARAM(512)      !header
CHARACTER*512 FG     !equal name
EQUIVALENCE ( FG , PARAM)

FLG=0                !clear flag
OPEN (UNIT=13,NAME=FNM,TYPE='OLD',FORM='UNFORMATTED',
     +  READONLY,ERR=1000)  !open file
READ (13 , ERR = 999 ) PARAM  !read header
STT=FG   !return the header to calling routine
```

```
IF ((FNM(7:7) .EQ. 'F') .OR. (FNM(6:6) .EQ. 'F')) THEN
READ(FG(289:296), *, ERR=1001)LOFQ   !fr scan
READ(FG(297:304), *, ERR=1001)ST
READ(FG(305:312), *, ERR=1001)INCRE
ELSE
READ(FG(313:320), *, ERR=1001)LOFQ  !az scan
READ(FG(321:328), *, ERR=1001)ST
READ(FG(329:336), *, ERR=1001)INCRE
ENDIF

KT=(ST-LOFQ)/INCRE   !get #of points

READ (13 ,ERR = 999 ) (YM(1,K),YM(2,K),K=1,KT)  !read data

CLOSE (13)  !close file

  RETURN

C       error handlers
999 CLOSE (13)
        FLG=1    !read error
RETURN
1000 CLOSE (13)
        FLG=2   !open error
RETURN
1001 CLOSE (13)
FLG=4  !decode error
RETURN
END
```

Bibliography

[1] E. K. Walton and J. D. Young, "The Ohio State University Compact Radar Cross-Section Measurement Range," *IEEE Trans. Antenna Propagat.*, vol. AP-32 No. 11, pp. 1218–1223, Nov. 1984.

[2] A. D. Yaghjian, "An Overview Of Near-Field Antenna Measurements," *IEEE Trans. Antenna Propagat.*, vol. AP-34 No. 1, pp. 30–45, Jan. 1986.

[3] E. B. Joy, "Near-Field Range Qualification Methodology," *IEEE Trans. Antenna Propagat.*, vol. AP-36 No. 6, pp. 836–843, June 1988.

[4] E. B. Joy and J. B. Rowland Jr., "Sample Spacing and Position Accuracy Requirements for spherical surface Near-Field Measurements," *IEEE AP-S Int. Symp. Digest*, vol. II, pp. 689–692, 1985.

[5] D. G. Falconer, "Sampling Rules for Near-Field Scanners," *Proc. AMTA*, pp. 3-3–3-8, 1988.

[6] D. M. Kerns, "Plane-Wave Scattering Matrix Theory of Antennas and Antenna-Antenna Interactions," *NBS Monograph*, vol. 162, p. , June 1981.

[7] D. T. Paris, W. M. Leach Jr., and E. B. Joy, "Basic Theory of Probe-Compensated Near-Field Measurements," *IEEE Trans. Antenna Propagat.*, vol. AP-26 No. 3, pp. 373–379, May 1978.

[8] A. D. Yaghjian, "Upper-Bound Errors in Far-Field Antenna Parameters Determined from Near-Field Measurements. Part 1: Analysis," Tech. Note 667, NBS, Oct. 1975.

[9] B. J. Cown and C. E. Ryan Jr., "Near-Field Scattering Measurements for Determining Complex Target RCS," *IEEE Trans. Antenna Propagat.*, vol. AP-37 No. 5, pp. 576–585, May 1989.

[10] W. D. Burnside, M. C. Gilreath, B. M. Kent, and G. L. Clerici, "Curved Edge Modifications of Compact Range Reflector," *IEEE Trans. Antenna Propagat.*, vol. AP-35 No. 2, pp. 176–182, Feb. 1987.

[11] R. C. Johnson, H. A. Ecker, and J. S. Hollis, "Determination of Far-Field Antenna Patterns from Near-Field Measurements," *Proc. IEEE*, vol. 61 No. 12, pp. 1668–1694, Dec. 1973.

[12] H. G. Booker and P. C. Clemmow, "The Concept of an Angular Spectrum of Plane Waves, and its relation to that of Polar Diagram and Aperture Distribution," *Proc. IEE*, vol. 97 pt. 3, pp. 11–17, Jan. 1950.

[13] E. B. Joy and D. T. Paris, "Spatial Sampling and Filtering in Near-Field Measurements," *IEEE Trans. Antenna Propagat.*, vol. AP-20 No. 3, pp. 253–261, May 1972.

[14] S. Tuhela-Reuning and E. K. Walton, "A Planar Near–Field Scanning Technique for Bistatic Radar Cross Section Measurements," Report 723105-1, ElectroScience Lab., The Ohio State University, Columbus, Dec. 1990.

[15] L. C. Beard, "Electromagnetic Scattering Measurements in a Cluttered Environment," Master's Thesis , ElectroScience Lab., The Ohio State University, Columbus, 1991.

723105-2,"Planar Near-Field Scanning for Compact Range Bistatic Radar Cross-Section Measurement," Tuhela-Reuning & Walton, Nov. 1991.